Very High Energy Gamma-Rays from Flat Spectrum Radio Quasars: Observational Prospects with the Cherenkov Telescope Array

MAIALEN ARRIETA

Very High Energy Gamma-Rays from Flat Spectrum Radio Quasars:

Observational Prospects with the Cherenkov Telescope Array

MAIALEN ARRIETA LOBO

ABSTRACT

Future Very High Energy (VHE, E>100 GeV) gamma-ray detection facilities (e.g. the Cherenkov Telescope Array (CTA)) will allow us to investigate the VHE regime behaviour of extragalactic objects such as blazars and its subclasses, BL Lac Objects and Flat Spectrum Radio Quasars (FSRQs). As such, this future ground-based facility will cast light upon an energy range beyond that of the Large Area Telescope (LAT) aboard the *Fermi* spacecraft, and also upon FSRQs, since current ground-based telescopes have mostly detected BL Lac objects. Given the existing data from the *Fermi*-LAT for a set of FSRQs, the present work is aimed at predicting not only the chances of detecting the sources in VHE gamma rays by considering their spectral shape, but also the existence of spectral cut-offs induced by pair-production with the Extragalactic Background Light (EBL). Data and results for the objects considered are presented, along with some conclusions.

Very High Energy Gamma-Rays from Flat Spectrum Radio Quasars:

Observational Prospects with the Cherenkov Telescope Array

MAIALEN ARRIETA LOBO

SUPERVISORS: A.M.BROWN AND P.M.CHADWICK

GAMMA-RAY ASTRONOMY GROUP

Durham University

A thesis submitted to the University of Durham
in accordance with the regulations
for admittance to the Degree of Master of Science.

August 2014

TABLE OF CONTENTS

List of Figures

List of Tables

Declaration of Authority

The work described in this thesis was undertaken between September 2013 and September 2014 while the author was a research student under the supervision of Dr. Anthony M. Brown and Prof. Paula M. Chadwick in the Department of Physics at the University of Durham.

This work has not been submitted for any other degree at the University of Durham or any other university.

Statement of Copyright

Acknowledgements

To my parents,

because without their unconditional support I would not be where I am now.

To Aitor,

since this months would have been much much harder without him.

To Itziar and Marisa,

in that they have made Durham feel like home.

To Paula and Anthony,

for introducing me to Gamma-Ray Astronomy,
for being a constant source of help,
for sharing their knowledge and experience,
for being the best Master supervisors one could possibly ever have.

Hope we can work together again at some point in the (near) future.

INTRODUCTION

Jetted Active Galactic Nuclei (AGN) are amongst the most powerful particle accelerators in the Universe. These extremely potent extragalactic objects are characterized by a pair of jets of High Energy (HE) relativistic particles and radiation ejected from the central engine of the galaxy, the Supermassive Black Hole (SMBH). When one of the jets is pointing towards the line of sight of the observer, we would see a *blazar*, whereas if the jet is observed at a different angle, the observed extragalactic object would be a *quasar*.

Blazars can be classified as *Flat Spectrum Radio Quasars* (FSRQ) and *BL Lac objects*. Both subclasses show very high luminosity levels and a rapidly variable emission in all the energy ranges of the Electromagnetic (EM) spectrum, from radio to gamma-ray frequencies. Compared to BL Lacs, whose energy distribution appears to be smooth (e.g. Stickel et al., 1991; Shaw et al. 2009), FSRQs show strong and broad emission lines in the optical range (Shaw et al., 2009). In addition, FSRQs seem to be more distant and more luminous than BL Lacs (e.g. Urry & Padovani, 1995; Lawrence et al., 1996; Ghisellini et al. 2010).

A non-thermal continuum spectrum corresponding to the relativistic jets clearly dominates the Spectral Energy Distribution (SED) of the two types of blazars. Depending on the wavelength at which the source is observed, different physical phenomena will be distinguishable when the SED is analyzed. Therefore, multi-wavelength surveys that analyse the whole EM spectrum of the sources are an essential tool for making deductions about the overall behaviour of the blazar.

With regards to gamma-ray wavelengths, the most energetic type of EM radiation in the Universe, one of the main challenges of VHE astrophysics lies in casting light upon the acceleration mechanisms responsible for the relativistic velocities of the particle stream. Moreover, gamma-ray emission region of AGN remains unresolved except for the radio lobes of the galaxy Centaurus A (Abdo et al, 2010a). The mechanisms originating the HE gamma-ray emission are also controversial, although recent interpretations (Barnacka et al., 2014) point towards inverse Compton radiation. Controversy is found as well when it comes to determining the origin of the seed photons for the inverse Compton effect, as we will explain in Section 2.5

After travelling from the source across the Universe, gamma-rays are detected with either ground-based or satellite based detectors. Once the corresponding data are gathered, the direction and energy of the photon can be determined, and therefore it is possible to reconstruct the event, locating the source of the incoming gamma-ray. A deep understanding of the source can be achieved by analysing the characteristics of the detected photons.

According to the Second *Fermi* Large Area Telescope (LAT) Catalogue (Nolan et al., 2012), 886 AGNs have so far been detected by LAT since its launch in 2008, of which 395 are BL Lacs and 310 FSRQs. Although the numbers of BL Lacs and FSRQs detected by *Fermi* are nearly equal, this is not the case for ground- based Cherenkov telescopes: FSRQs are outnumbered by BL Lacs in this type of detector (1 FSRQ versus 19 Bl Lacs detected by HESS, according to Abramowski et al., 2014). This tendency might change with the implementation of the next generation of ground-based Cherenkov telescopes, namely the Cherenkov Telescope Array (CTA) (Section 4.4 and e.g. Funk & Hinton, 2013; Reimer & Böttcher; 2013). With its improved sensitivity and energy coverage compared to the currently available gamma-ray detectors (e.g. *Fermi* or HESS), CTA is expected to increase the number of detected extragalactic gamma-ray sources at TeV energies by an order of magnitude.

While the energy ranges covered by *Fermi* and HESS are 20 MeV - 300 GeV for the former and 100 GeV - 10 TeV for the latter, CTA is expected to cover a wide energy range from 10s of GeV up to 100s TeV. Moreover, CTA will provide much higher quality data, allowing a more precise interpretation of the behaviour and characteristics of the objects producing the detected gamma-ray photons. Topics from AGN population studies and their cosmological evolution via the formation and evolution of extragalactic jets, to the study of the EBL that would shed light on cosmological galaxy evolution and structure formation, will enter a new era when CTA comes into operation and high quality data start to be gathered.

In order to benefit from the full potential of the telescopes from the very early stages of the project, predictions regarding the objects likely to be observed are quite useful. Since CTA is still in its prototyping phase, foreseeing whether a certain object will be detected or not will facilitate the final design of the telescope and its scientific priorities. With this in mind, this work aims at making observational predictions of FSRQs already observed by *Fermi*-LAT for CTA.

As FSRQs seem to be more difficult to detect than BL Lacs at high energies, the enhanced observational capacities and wider energy range of CTA should in principle increase the chances of detecting FSRQs, as previously mentioned. Nevertheless, the detection is highly dependent on the array configuration of the telescope which is finally chosen. For this work, a number of different sensitivity curves corresponding to different configurations are considered, and predictions on the detection of a selected sample of FSRQs are presented.

The first four chapters of this work are related to the fundamental background theory to understand the data analysis. The following chapters explain the data analysis itself and the results obtained. Last, a discussion about the results obtained is presented.

1. INTERACTIONS OF HIGH ENERGY PHOTONS AND PARTICLES

For astronomical sources, the energies of the observed gamma-ray radiation (starting from the rest mass energy of an electron, i.e. 511 keV, up to TeVs) cannot be obtained from nuclear decay, which is the mechanism by which low energy (LE) gamma-rays are obtained in nuclear laboratories. Such energies cannot be generated by thermal emissions of hot celestial objects either: there is nothing hot enough in the Universe - apart from the Big Bang itself - to emit such energetic gamma-rays. Therefore, HE gamma-rays probe the existence of a *non-thermal* Universe: there have to be other mechanisms that allow the concentration of large amounts of energy onto a single quantum of radiation.

Regarding the creation of cosmic HE gamma-rays, two different mechanisms can be considered:

1. ***Bottom-up fashion:*** Highly relativistic particles that collide with ambient gas or interact with photon or magnetic fields. The flux and spectrum of the gamma-rays reflect the flux and spectrum of the HE particles. Hence, gamma-rays can be used to trace electrons/protons in very distant regions of our Galaxy or the Universe.

   Particles reach the relativistic velocities required to create gamma-rays in this bottom-up fashion via the Fermi acceleration mechanisms (see, e.g. Bell 1978). Fermi acceleration, also known as diffusive shock acceleration, is the acceleration that charged particles undergo when being repeatedly reflected, usually by a magnetic mirror. Fermi acceleration is thought to be the primary mechanism by which particles gain non-thermal energies in astrophysical shock waves, and it plays a very important role in many astrophysical models, mainly of shocks including solar flares and supernova remnants.

   There are two types of Fermi acceleration: first-order Fermi acceleration (in shocks) and second-order Fermi acceleration (in the environment of moving magnetized gas clouds). In both cases the environment has to be collisionless (two-body collisions can be neglected with respect to interactions between the charged particles conforming the plasma) in order for the mechanism to be effective. This is because

Fermi acceleration only applies to particles with energies exceeding the thermal energies, and frequent collisions with surrounding particles will cause severe energy loss and as a result no acceleration will occur.

2. ***Top-down fashion:*** By the decay of heavy particles, i.e. hypothetical dark matter particles or cosmic strings, relics left over the Big Bang. Accordingly, gamma-rays would be one of the most suitable ways of studying dark matter.

The created gamma-ray photons travel a considerable distance before undergoing an interaction with matter. This distance depends mainly on the energy of the photon and the density of the matter traversed. The main physical processes involving HE photons and relativistic particles are *photoelectric absorption*, *Compton scattering*, *Inverse Compton scattering*, *Synchrotron radiation* and *pair production*. All of these lead to a partial or total transfer of energy from the photon to the charged particle (usually an electron) or vice-versa.

The following chapter is devoted to explaining these processes, which are of great importance both for detecting HE particles and photons, and for studying the phenomena in which such particles/photons get involved.

Table 1: Different gamma-energy ranges mentioned throughout the present work.

Low Energy (LE) Gamma-Rays	100 keV $<$ E$<$ 100 MeV
High Energy (HE) Gamma-Rays	100 MeV $<$ E $<$ 100 GeV
Very High Energy (VHE) Gamma-Rays	E $>$ 100 GeV

1. Photoelectric Absorption

Photoelectric absorption is the main interaction for gamma-rays in the LE range (100 keV - 100 MeV) where $\hbar\omega \gg m_e c^2$, $\epsilon = \hbar\omega$ being the energy of the incident photon, and $E = m_e c^2$ the rest mass energy of the electron, i.e. 511 keV.

This process is enhanced for materials with large *atomic number, Z*, and is more likely to happen when the energy of the incident photon is just slightly greater than the binding energy of the electron in the atom with which the photon will interact. So, if the energy of the incoming photon ϵ is higher than the energy E_i of an electron located in the atomic level i, the electron can be ejected from that level due to a energy transference from the photon to the electron, as illustrated in Figure 1.

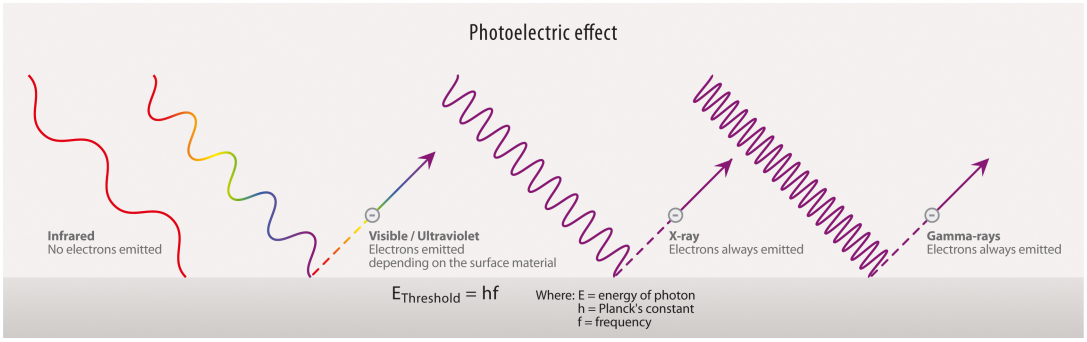

Figure 1: *Illustration of the photoelectric effect [60].*

The ejected electron carries the difference in energies $\hbar\omega - E_i$ in form of kinetic energy. The threshold $\hbar\omega = E_i$ corresponds to an *absorption edge* in the spectrum of the radiation, since photons with energy lower than $\hbar\omega$ do not have enough energy to eject an electron from this atomic level.

The vacancy created by the ejected electron will rapidly be filled with an electron from a outer shell of the atom. The transition of this electron from its original shell is accompanied by the release of X-ray, UltraViolet (UV) or visible radiation.

For gamma-rays with energies above 0.5 MeV, the ejected electron usually belongs to the *K-shell* of the atom, since the innermost shell of the atom is the one with the highest binding energy. Thus, the electrons from this shell are able to absorb the gamma-ray energy and transform it into kinetic energy.

However, the cross-section for photoelectric absorption decreases as ω^{-3}. Hence, this interaction is not important beyond the LE gamma-ray energy range (Figure 2).

2. Compton Scattering

The inelastic scattering[1] of a HE photon by a stationary free charged particle, usually an electron, when $\hbar\omega \gg m_e c^2$, is known as *Compton Scattering*. The incident photon (HE) transfers part of its energy to the charged particle, resulting in a lower energy photon and a higher energy particle.

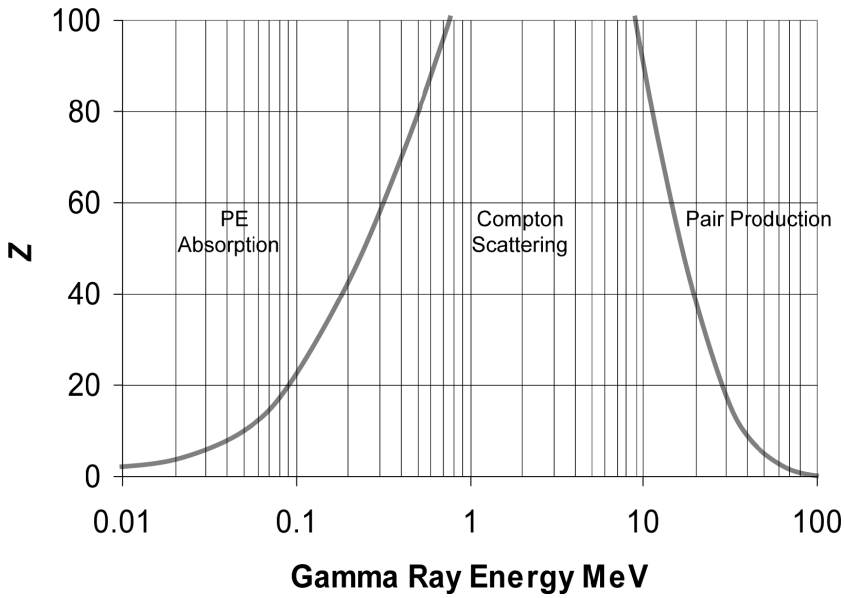

Figure 2: *The relative importance of different forms of energy loss mechanisms for gamma-rays as a function of photon energy and the atomic number of the material [71].*

The energies of the initial and the scattered photon are related by Eq. 1

$$\lambda_f - \lambda_i = \lambda_c(1 - \cos\theta) \tag{1}$$

where λ_f is the wavelength of the scattered photon, λ_i the wavelength of the incident photon, $\lambda_c h/ = m_e c$ is the *Compton wavelength* and θ the scattering angle (see Figure 3). The same equation can be expressed in terms of *energies* as follows

$$E_f = \frac{E_i}{1 + \dfrac{E_i}{m_e c^2}(1 - \cos\theta)} \,. \tag{2}$$

[1] In inelastic scattering processes, the wavelength of the scattered photon is different from the wavelength of the incident photon. Hence, energy is not conserved.

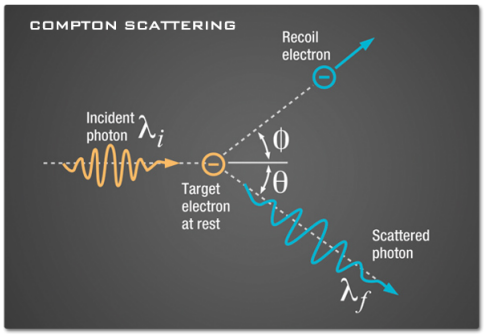

Figure 3: *Electron scattering via Compton effect [61].*

The discovery of this phenomenon by Compton in 1923 demonstrated that light cannot be explained purely as a wave phenomenon, proving Einstein's theory that light has properties of both waves and particles.

3. Inverse Compton Scattering

The scattering of a LE photon by a HE charged particle (i.e. a relativistic electron) is called *inverse Compton scattering*[2]. As a result, LE photons can be up-scattered to HE or VHE by the electrons. The energy gained by the up-scattered photon in the inverse effect is the opposite of the energy lost by the HE photon scattered in the Compton effect.

In the Thomson regime, the average energy of the scattered photons is (Blumenthal & Gould, 1970)

$$\hbar\omega' = \frac{4}{3}\gamma^2\hbar\omega_0 \tag{3}$$

where ω_0 is the frequency of the initial photon. The fact that the frequency of the photons scattered by ultra-relativistic electrons is $\sim \gamma^2$ times the frequency of the initial LE photon is very important in High Energy Astrophysics (HEA). Electrons with Lorentz factors $\gamma \sim$ 100-1000 can be found in different astronomical sources (i.e. jets of AGN), so LE photons can be scattered up to very much higher energies. In the Klein-Nishina regime, though, the average energy of the scattered photon is $\sim \gamma$ times the frequency of the initial LE photon (Blumenthal & Gould, 1970).

[2]Although the name might cause some confusion, inverse Compton is identical to Compton scattering, but viewed in a frame in which the electron is highly relativistic.

Let us consider a relativistic electron of $\gamma \sim 1000$. According to Eq. 3, the scattered radiation energy is roughly 10^6 times the energy of the incoming LE photon. Therefore, an optical photon with $\nu_0 = 10^{14}$Hz will become gamma-rays with frequency $\nu = 10^{20}$Hz (around 1.6 MeV), so inverse Compton is a very effective method to create HE photons.

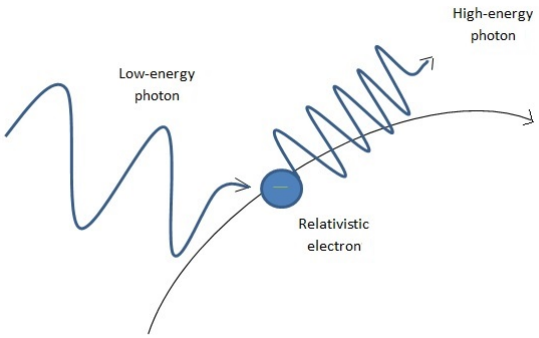

Figure 4: *Illustration of Inverse Compton scattering. The interaction between a relativistic electron an a LE photon originates a HE photon due to the energy transference from the electron to the photon.*

4. Synchrotron radiation

Synchrotron emission is a type of non-thermal radiation generated by charged particles (usually electrons) spiralling around magnetic field lines at close to the speed of light. Since the electrons are always changing direction, they are in effect accelerating and emitting photons with frequencies determined by the speed of the electron at that instant.

Although particularly important to radio astronomers, depending on the energy of the electron and the strength of the magnetic field, synchrotron emission can also occur at visible, ultraviolet and X-ray wavelengths. The radiation emitted is confined to a narrow cone pointing in the direction of the motion of the particle, in a process called *beaming*. It is also polarised in the plane perpendicular to the magnetic field, with the degree and orientation of the polarisation providing information about the magnetic field of the source.

The spectrum of synchrotron emission results from summing the emission spectra of individual electrons (Figure 5). As the electron spirals around the magnetic field, it emits radiation over a range of frequencies peaking at ν_0, the critical frequency. The

longer the electron travels around the magnetic field, the more energy it loses, the narrower the spiral it makes, and the longer the wavelength of the critical frequency.

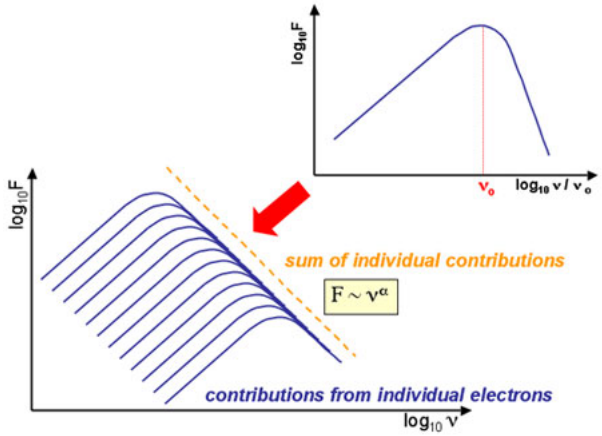

Figure 5: *The sum of the spectra of electrons following a power law distribution over different frequencies, the characteristic spectrum of synchrotron radiation is observed to have a power law shape. Credit: Swinburne University.*

In many cases, synchrotron radiation is emitted from electrons which have a power law distribution. By summing the spectra from the individual electrons we find that synchrotron emission has a characteristic spectrum, where flux steadily declines with frequency according to the relation $F \sim \nu^{\alpha}$, where α is known as the spectral index for the object.

5. Electron-Positron Pair Production

The process of pair production is the creation of an elementary particle and its antiparticle from a neutral boson, usually by a photon, as illustrated in Figure 6. Pair production of either electron and positron, muon and anti-muon or tau and anti-tau will happen provided the photon is energetic enough so as to create the pair, and the energy and momentum can both be conserved. This last condition implies that pair production cannot take place in free space, since momentum and energy cannot be conserved at the same time in free space.

Consider a photon of energy $\epsilon = \hbar\omega$ decaying into an electron-positron pair $e^- + e^+$ with kinetic energies of $E_k = (\gamma - 1)m_e c^2$, where γ is the Lorentz factor and m_e the mass of the electron in rest:

$$\hbar\omega \longrightarrow (\gamma - 1)m_e c^2 + (\gamma - 1)m_e c^2 \tag{4}$$

If both energy and momentum were to be conserved, the $e^- + e^+$ would have to move parallel to the initial photon,

$$\begin{aligned} E &= \hbar\omega \\ & \longrightarrow \quad p = 2\gamma m_e v = \frac{\hbar\omega}{c}\frac{v}{c} \\ p_0 &= \frac{\hbar\omega}{c} \end{aligned} \tag{5}$$

Given that v cannot be equal to c in vacuum, energy and momentum cannot be conserved at the same time in free space. A third element is necessary (e.g. a nucleus or photon) to absorb either some of the energy or momentum.

On the other hand, the photon has to be energetic enough to create the pair, establishing a minimum energy threshold of

$$\hbar\omega = 2m_e c^2 \tag{6}$$

according to which the photon has to carry, at least, twice the rest mass energy of the particles (511 keV for electrons) to decay by means of pair production.

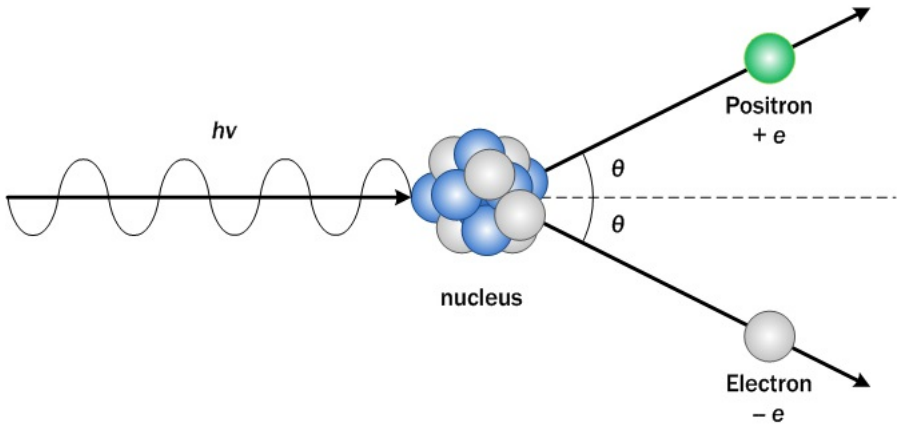

Figure 6: *A electron and a positron are created via pair production when a very HE photon encounters an atom or a molecule [62].*

4.1 Electron-photon cascades and Electromagnetic showers

When a gamma-ray enters the Earth's atmosphere, an electron-positron pair is created by means of pair production. If the energy of the gamma-ray, and hence of the electron-positron pair, is large enough, each of the charged particles will create a HE photon via *Bremsstrahlung*[3] which will eventually decay into an electron-positron pair.

This process results in an electromagnetic cascade (illustrated in Figure 7) which will continue down through the atmosphere along the axis of the trajectory of the original gamma-ray. The total energy of the secondary particles will be a good representation of the energy of the initial gamma-ray.

The probability of a pair production interaction happening is given by

$$\xi \; = \; \mathrm{R} \; = \; \xi_0 \mathrm{Ln2}, \tag{7}$$

where R is the *radiation length*. The radiation length of a material is the amount of matter traversed by a particle until a certain level of energy is reached.

Given that HE electrons (> 10 MeV) mainly lose energy in matter via Bremsstrahlung, and HE photons via pair production, the radiation length can refer to:

- The mean distance over which a HE electron loses all but 1/e of its energy by Bremsstrahlung.
- 7/9 of the mean free path for pair production by a HE photon.
- The appropriate scale length for describing HE EM cascades.

The approximate expression for the radiation length is

$$R = \frac{1432.8}{Z(Z+1)(11.319 - \mathrm{Ln}Z)}\,\mathrm{g\,cm^{-2}}. \tag{8}$$

Assuming that the cascade is initiated by a photon of energy E_0, an electron-positron pair be produced after a distance R. The particles created share the energy of the photon, $E_{e^-} = E_{e^+} = \frac{E_0}{2}$. After travelling another R radiation length, the electron-positron pair loses half of its energy by radiating a photon of energy $\frac{E_0}{4}$. The whole process is illustrated in Figure 7. Thus, EM cascades not only transform a VHE gamma-ray into

[3] Electromagnetic radiation created when a charged particle is depleted by another charged particle.

a very large number of fast moving charged particles, but also spread the particles over a vast area.

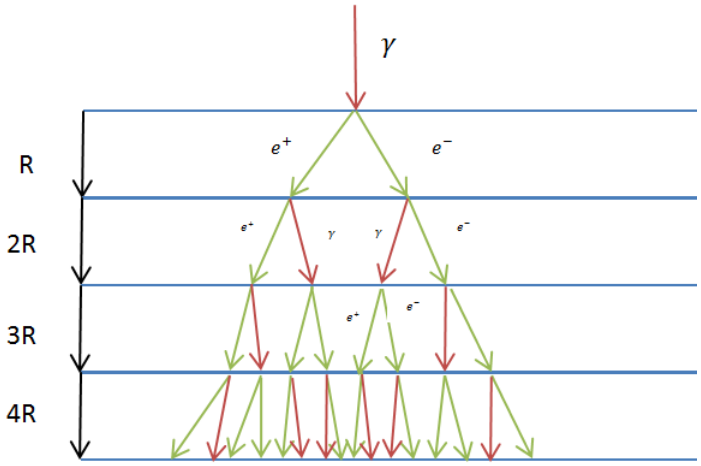

Figure 7: *Electromagnetic shower caused by a gamma-ray entering the Earth's atmosphere. The initial photon creates an electron-positron via pair production after travelling a radiation length R. Each of these charged particles will create a photon, and the process will continue until the threshold energy level is reached.*

This way, after a distance nR, a total number 2^n of gamma-rays, electrons and positrons is created, whose average energy is $\frac{E_0}{2^n}$. An average photon-initiated shower consists of $\frac{2}{3}$ charged particles and $\frac{1}{3}$ photons.

The cascade will continue until the minimum energy threshold E_c, i.e. the energy in which the Bremsstrahlung and ionization rates are equal, is reached. Below this critical energy, ionization rather than Bremsstrahlung becomes the predominant energy-loss process. A rough estimate to this threshold energy is $E_c = 800\,\mathrm{MeV}/(Z + 1.2)$.

For gamma-rays of energy 100 TeV and above, sufficient secondary particles can reach ground level for the shower to be detected by arrays of particle detectors spread over areas of 0.1 km^2. At lower energies the cascade will die out as the average energy of the secondary particles drops to the point that ionization losses become the major loss process.

In fact, for a primary gamma-ray of energy 1 TeV, few secondary particles will reach even mountain altitude. However, as the relativistic particles traverse the atmosphere, they excite the atmosphere to radiate Cherenkov light (see Section 5 in Chapter 4 for further information about Cherenkov radiation) with high efficiency. Although the fraction of energy that goes into this mode is small (less than 10^{-6} of the primary energy), it provides a very easy way to detect the cascade and hence the gamma-ray.

2. ACTIVE GALACTIC NUCLEI AS SOURCES OF GAMMA RADIATION

Gamma-ray sources can be Galactic or extragalactic. Since in this work we concentrate on FSRQs, which are extragalactic sources of HE radiation, only the types of gamma-ray sources encountered outside from the Milky Way will be presented. In this chapter Active Galaxies (AGs) and AGN are presented as sources of extragalactic VHE radiation.

1. Active Galactic Nuclei

AGs are galaxies characterized by certain properties such as high luminosity in a region of the spectrum other than optical (e.g. radio, UV, IR), non-thermal spectra that do not look like the sum of many stellar spectra, bright star-like nuclei, rapid variability, and sometimes radio jets.

In the zoo of AGs, one can find *radio galaxies*, *quasars*, *Seyfert galaxies* and *blazars*. Even if each of these AG types has some spectral peculiarity by itself, in all these types of galaxies there is evidence that a very large amount of energy is being released in a region that is tiny compared with the size of the galaxy.

Usually, these tiny regions can be traced to the nucleus of the host galaxies, so the origin of the excess radiation is attributed to the AGN. AGN are compact regions of enhanced activity powered by the release of gravitational energy from an accreting central SMBH. The SMBH cannot be seen directly, but the UV continuum radiation is generally presumed to be thermal emission from the hot gas that forms an accretion disk surrounding the black hole.

Around 50 AGN have been detected in the VHE gamma-ray regime by current ground-based instruments such as HESS, VERITAS or MAGIC (e.g. Holder, 2012). They are not only one of the largest energy storehouses known in the Universe, but also the most luminous and persistent sources of EM radiation, so they can be used as a probe of conditions between the observer and the AGN.

Some AGN possess narrow features called jets projecting up several hundreds of kpc from their nuclei. These jets are considered to be streams of energetic particles flowing from the central engine. But if an AGN consisted solely of the central engine and the jets, observers would see X-rays and UV radiation from the hot accretion disc and very little else, which is not what observations show.

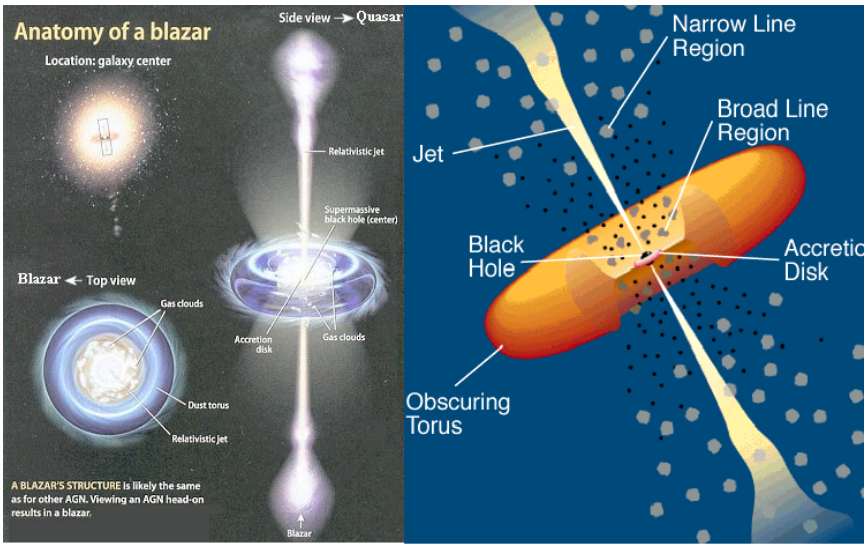

Figure 8: *Two different pictures showing the unified AGN model. See [64] for the left and Urry & Padovani 1995 for the right.*

To account for the strong IR emission coming from many AGN, the standard model for AGN includes a torus of gas and dust surrounding the central engine (see Figure 8). In such a model, dust particles are heated by the radiation from the engine until they are warm enough to radiate energy at the same rate at which they receive it. The dust cloud will act to convert UV and X-rays from the engine into IR radiation. Therefore, we consider a model in which the engine is surrounded by gas clouds. If these clouds are illuminated by UV or X-rays from the engine, they will absorb the energy and emit the characteristic lines of the gases making up the clouds.

The relativistic jets are usually identified by the detection of bright non-thermal radio emission as observed in radio-loud AGN. Only around 10% of AGN are known to be radio-loud, though. The relativistic particles from the jet are believed to create the gamma-ray emission observed from AGN when they interact with the gas clouds surrounding the central engine (for papers on the location of the gamma-ray emission see, e.g., Marscher et al., 2010; Brown, 2013, Abdo et al., 2010a).

The majority of the AGN detected at VHE gamma-ray energies belong to the *blazar* class, meaning that the relativistic jet is pointing closely towards the line-of-sight of the observer. The fact that the observed gamma-ray flux varies very quickly means that radiation in these wavelengths must come from a very small region.

Next, different types of AGN and their main characteristics are presented. Special emphasis is put into the blazar class and its subclass, FSRQs, the objects of our analysis.

2. Radio Galaxies

The birth of modern HEA was associated with Karl Guthe Jansky's discovery of the radio emission of our Galaxy in 1933 (Jansky, 1933). The radio emission of the Milky Way was identified as synchrotron radiation (because of the power-law form of its radio spectrum and its high degree of polarization). Subsequent observations revealed large populations of Galactic and extragalactic radio sources. For instance, the observation of synchrotron radiation from Cassiopeia A[4] demonstrated that supernova remnants are sources of relativistic electrons (Baade and Minkowski, 1954).

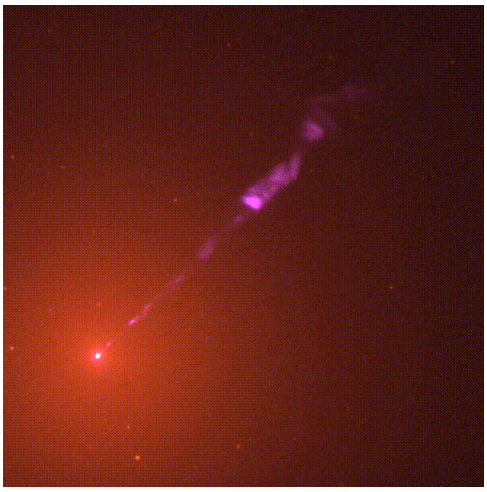

Figure 9: *Color composite from stacked HST WFPC2 images in the near-UV and near-IR (at about 2900 and 8000 Angstroms) of the radio galaxy M87. The color mix is not quite what a purely visual filter selection would produce. Anyhow, the color difference between the old stars dominating the galaxy and the bluer light of the jet (tending to violet in this rendition) is clear. The small objects scattered around the field of view are are a few of the thousands of globular star clusters in M87 itself. Image credit: John Biretta.*

[4]Cassiopeia A is a SuperNova Remnant (SNR) located in the constellation Cassiopeia within the Milky way, the brightest extrasolar radio source in the sky at frequencies above 1 GHz.

When observing the radio source Cygnus A[5], astronomers discovered that it is a million times more powerful in the radio regime than the Milky Way, but, surprisingly, the radio emission did not originate from the galaxy itself. In 1953, it was shown that this radiation came from two huge lobes almost symmetrically located with respect to a luminous radio galaxy (Jennison & Das Gupta, 1953).

Also in 1953, Iosif S. Shklovsky proposed that both the optical and the radio emission of the supernova remnant, the Crab Nebula[6], was synchrotron radiation (Shklovsky, 1953). Therefore, the continuum emission of the nebula should be linearly polarized, which is in fact the case, as detected by, for instance, Vashakidze in 1954 (Vashakidze, 1954) or Oort and Walraven in 1956 (Oort & Walraven, 1956).

In addition, the jet in the radio galaxy M87[7] (Figure 9) was found to be linearly polarized too, and its radiation was identified as synchrotron emission of ultra-relativistic electrons (Baade, 1956).

In 1956, G.R. Burbidge estimated the minimum energy requirements in relativistic particles and magnetic fields for synchrotron radiation sources such as Cygnus A, finding that at least 2×10^{52} J of energy had to be in the form of relativistic particles and magnetic energy (Burbidge, 1956). He inferred that there must be some efficient mechanism by which rest-mass energy can be converted into ultra-high energy electrons and magnetic fields, and then ejected from the host galaxy into intergalactic space.

The galaxies associated with these bright radio sources were called *Radio Galaxies*, and they show a luminosity from 1000 to 100 million times that of the Milky way. Despite the fact that all galaxies emit radio emission, something different must be happening in the radio galaxies, since they are much more powerful radio emitters than galaxies such as ours and are powered by jets of relativistic material originating in their AGN.

The unexpected discoveries related to radio galaxies led to improvements in radio telescopes to unravel the astrophysics of radio sources. Their distances were found by first determining accurate radio positions for the sources and then identifying the associated radio galaxies (for which redshifts could be measured).

[5]Cygnus A (3C 405) is one of the most famous radio galaxies which is among the strongest radio sources in the sky.
[6]The Crab Nebula is a SNR and pulsar wind nebula situated in the constellation of Taurus, within the Milky Way.
[7]Messier 87, also known as M87, Virgo A or NGC 4486, is a supergiant elliptical galaxy, and it is the second brightest galaxy within the Virgo Cluster.

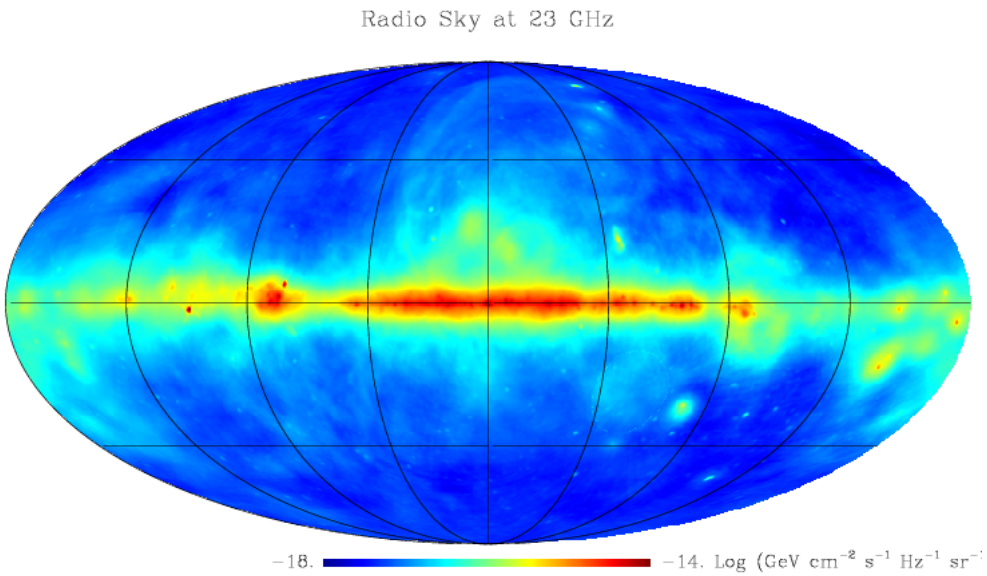

Figure 10: *Sky map of the Milky Way at a radio frequency of 23 GHz. The Galactic plane is clearly visible, with the galactic centre in the middle and the Galactic disc extending horizontally from it (Borriello et al. 2009).*

3. Quasars

By the 1960s, the positions of radio sources could be measured with sufficient accuracy for identifications to be made with faint galaxies. There were three strange cases, though: 3C48, 3C196 and 3C286, which had been identified as stars of an unknown type with strange, optical spectra. As they resemble stars in their point-like appearance, they were named *Quasi Stellar Radio Sources*,or *quasars*.

Even if they take after stars in their point-like appearance, the spectra of quasars are quite unlike those of stars: the emission lines turn out to be those of hydrogen and other elements, but significantly redshifted (Figure 11).

The high redshifts of many quasars cause some of the features observed in the visible part of the spectrum to correspond to emission features in the UV in closer objects. Taking these significant redshifts into account, all quasars must be highly luminous to be seen by us at all. At the same time, their spectra are similar to those of Seyfert 1 galaxies (Section 2.4), with prominent broad lines[8] but rather weaker narrow lines[9].

[8]Broad Emission Lines (BLs): Spectral lines coming from cold material close to the SMBH (see Figure 7). Lines are broad because the emitting material is revolving at high speed around the black hole, causing a range of Doppler shifts of the emitted photons.

[9]Narrow Emission Lines (NLs): Emission lines from further away from the SMBH. The clouds do not have such high velocities, hence the Doppler shifts are not as large and the lines are not as broad.

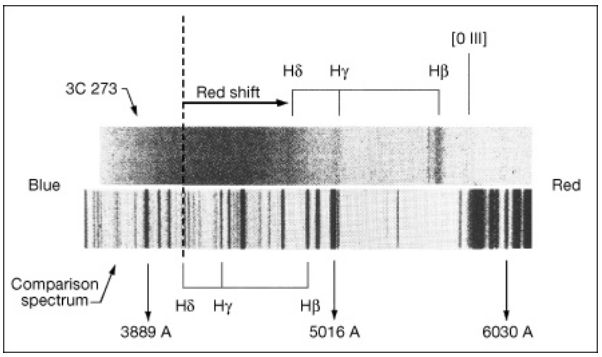

Figure 11: *Optical spectrum of the distant quasar 3C273 (redshift z=0.158). The redshift of the hydrogen spectral lines Hδ, Hγ and Hβ is clearly visible. The large redshift indicates how distant the source is, and the width of the lines points towards rapid internal motion within the quasar itself. Image credit: Palomar/Caltech.*

Being so distant[10], it has been difficult to study the host galaxies that contain quasars. Nowadays, quasars are considered to be remote, very luminous AGN buried in galaxies of normal luminosity. They are believed to be the most luminous examples of AGN known.

4. Seyfert Galaxies

Seyfert galaxies, which amount to 10% of all galaxies, have a quasar-like nucleus, but the host galaxy is clearly distinguishable. These galaxies are named after Carl Keenan Seyfert, who identified this galaxy class in 1943 (Seyfert, 1943). Seyfert selected a list of galaxies, the majority of which were spiral and shared the following common features:

- Containing an exceedingly luminous stellar or semi-stellar nucleus which contains a relatively large percentage of the total light.
- The spectra of the intense continuum radiation from their nuclei are smooth, unlike the spectrum of starlight.

Originally, the definition of these galaxies was primarily morphological: galaxies with high surface-brightness nuclei. When observed through a large telescope, a Seyfert galaxy looks like a distant spiral galaxy with a star in its centre, but subsequent spectroscopy revealed unusual emission-line characteristics. Nowadays Seyfert galaxies are identified spectroscopically by the presence of strong, high-ionization emission lines. In addition, morphological studies indicate that most, if not all, Seyferts are located in

[10]The most distant quasar discovered presents a redshift of $z = 7.085$ (Morlock et al., 2011.)

spiral galaxies.

Seyfert galaxies can be divided in two subclasses. *Type 1 Seyferts* show two sets of emission lines superimposed to one another, one corresponding to BLs and the other to NLs, whereas in *type 2 Seyferts* only the NLs are visible. A detailed study of the spectra of radio galaxies shows that there are similarities between Seyferts and radio galaxies:

I Broad-Line Radio Galaxies (BLRG), with similar spectra to Seyfert 1 galaxies.

II Narrow-Line Radio Galaxies (NLRG), with similar spectra to Seyfert 2 galaxies.

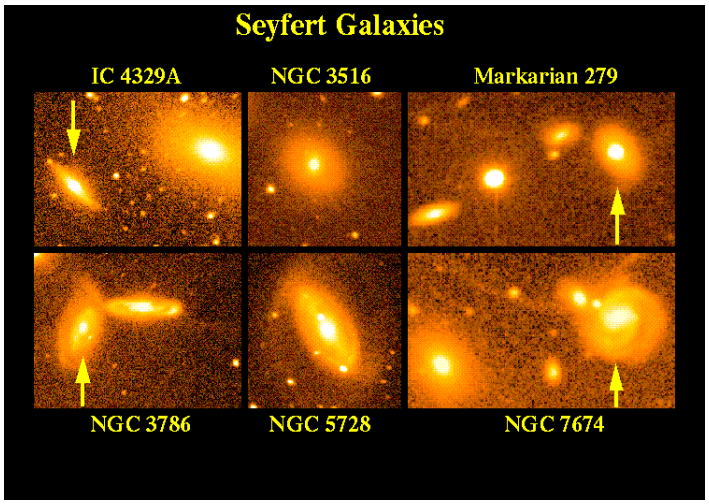

Figure 12: *Ground-based wide-field images showing the different types and environments in which Seyfert galaxies are found. IC 4329A, NGC 3516, and Markarian 279 are type 1 Seyferts, NGC 3786 is an intermediate "type 1.5" nucleus", and NGC 5728 and NGC 7674 are type 2 objects. This set includes fairly isolated galaxies (NGC 3516 and 5728) as well as several undergoing gravitational interactions with close neighbours, which has been widely suspected of contributing to the Seyfert phenomenon. V-band images taken using a Texas Instruments CCD at the 1.1-m Hall telescope of Lowell Observatory, described in detail in (Keel, 1996).*

Although the differences in the optical spectra of Seyfert 2s and NLRGs are small, they are much larger for Seyfert 1s and BLRGs. Another difference between Seyferts and radio galaxies is that practically all Seyferts are spiral galaxies, whereas the radio galaxies are giant ellipticals.

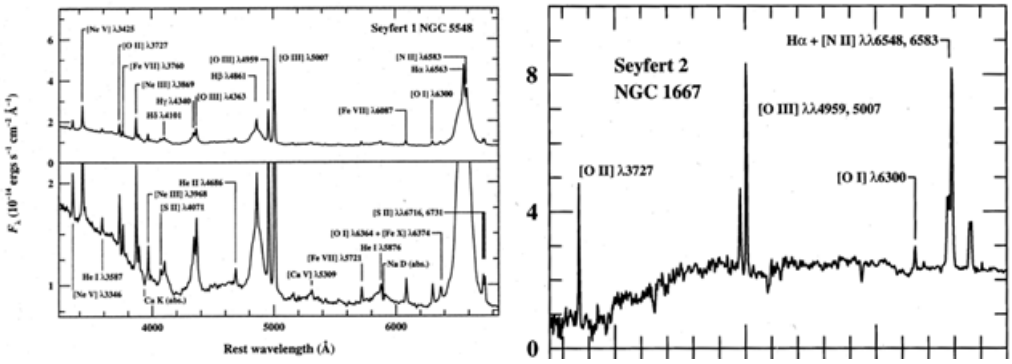

Figure 13: *LEFT - Optical spectra of NGC1275, a type 1 Seyfert. Prominent BELs and NELs, along with strong absorption features of the host galaxy spectrum are marked. The full width at half maximum (FWHM) of the broad components is about 5900 km s^{-1}, and the width of the narrow components is about 400 km s^{-1}. Data courtesy of A. V. Filippenko. RIGHT - Optical spectra of NCG1667, a type 2 Seyfert. The difference in the widths of the lines in both spectra is the criteria for classifying these galaxies into one type or the other.*

5. Blazars

Blazars are jetted AGN whose relativistic jet is pointing very closely towards our line of sight (see Figure 8). They comprise the most numerous extragalactic VHE gamma-ray source set, i.e. sources with $E > 100$ GeV, and they are usually classified in two types: BL Lac objects and Flat Spectrum Radio Quasars (FSRQs), the latter being distinguished from the former due to the presence of broad emission lines in their spectra (Figure 14).

Blazars are characterized by very rapid variability, high and variable polarization, superluminal motion, and very high luminosities. They appear to be the most 'active' and 'violent' kind of AGN.

The observed rapid variability and enhanced flux is known to be due to the jet pointing close towards the Earth, so the bulk relativistic motion of the particle stream causes radiation to be beamed in a forward direction, making the variability appear more rapid and the luminosity higher than in the rest frame (e.g. Urry & Padovani, 1995).

Back in the 1960s, studies of variability of AGN radio sources suggested that source sizes are around a light week. Therefore, the angular sizes of the sources should be ≈1 milli-arcsecond. This is difficult to resolve with conventional interferometers, which led

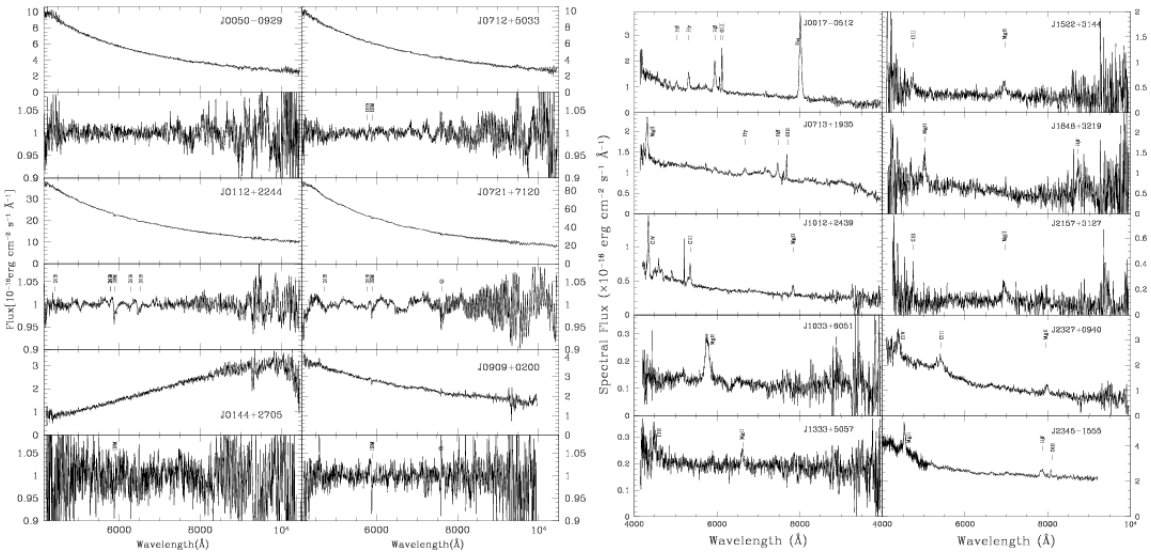

Figure 14: *Spectra of BL Lac (left) and FSRQ (right) objects in the Fermi-LBAS sample. The lack of strong emission lines can be seen in the upper left panels (Shaw et al., 2009).*

to the development of the Very Long Baseline Interferometry (VLBI) technique (see Appendix D).

In 1968, the first milli-arcsecond resolution data on radio-loud AGN obtained by this technique proved they had sizes of 1 milli-arcsecond, as predicted. Around 1970s, it was discerned that for the source 3C279, two VLBI maps taken four months apart showed the source had expanded $\approx 0.14 \pm 0.04$ milli-arcseconds. The distance of 3C279 (redshift of $z = 0.536$) implied it had expanded at a velocity of about ten times the speed of light.

In fact, virtually every blazar exhibits superluminal motion in high-resolution radio maps (Vermeulen & Cohen, 1994), which is easily explained by the above-mentioned relativistic bulk motion along the line-of sight. That is: the superluminal motion is an 'optical illusion' caused by the jets of relativistic particles being closely oriented towards the line-of-sight.

In addition to this, among the sources found in low frequency radio surveys, a number of them appeared to have flat radio spectra. All the 'flat-spectrum objects' were of very small angular size too, and often variable in the time scale of months or years. Given the compact nature of the sources, the emitting electrons had to be relativistic, which was consistent with the theory of relativistic particles causing the apparent superluminal motion.

A natural interpretation of observations was that the flat spectra resulted from the superposition of a number of compact source components in which synchrotron self-radiation took place at high radio frequencies. As such, the compact and highly variable

radio source VRO 42.22.01 was found to be associated with the 'variable star' BL Lac (Schmitt, 1968), and the optical spectrum of BL Lac was found to resemble a power law and was featureless. Therefore, this source became the prototype of the objects known as *BL Lac objects*.

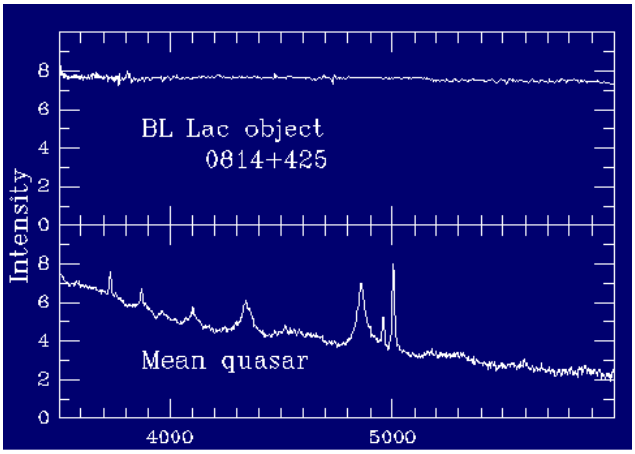

Figure 15: *Spectra of a BL Lac object (above) and a mean quasar (below). When compared to the quasar's, the spectra of the BL Lac object is outstandingly flat. For the "mean quasar" spectrum see Francis et al. 1991, and Lawrence et al. 1996 for 0814+425.*

Since the spectrum of such objects is so flat (see Figure 15), without any feature, it is a challenge to measure their redshifts. Nonetheless, it can be done, e.g. making observations when the nucleus is in a state of low activity. BL Lac objects are generally low redshift, very rare objects, $z < 0.2$.

There is a closely-related family of objects, the *Flat Spectrum Radio Quasars*, (FSRQs). While both blazar classes share the properties of a non-thermal continuum, FSRQs show strong and broad optical emission lines in their spectrum (Figure 14), and usually have larger redshifts than BL Lac objects. Also, the broad emission lines are intrinsically brighter in FSRQs than in BL Lacs (Padovani, 1992).

Despite these differences, the SEDs of the two subclasses of blazars are very similar: two bumps are clearly distinguishable in them (Figure 16). The first peak extends from radio to optical or UV to X-ray wavebands, while the second extends from X-rays to gamma-rays. As for the mechanisms providing the peaks, synchrotron radiation of the relativistic electrons of the jet is believed to create the LE one, whereas the origin of the HE peak is more controversial.

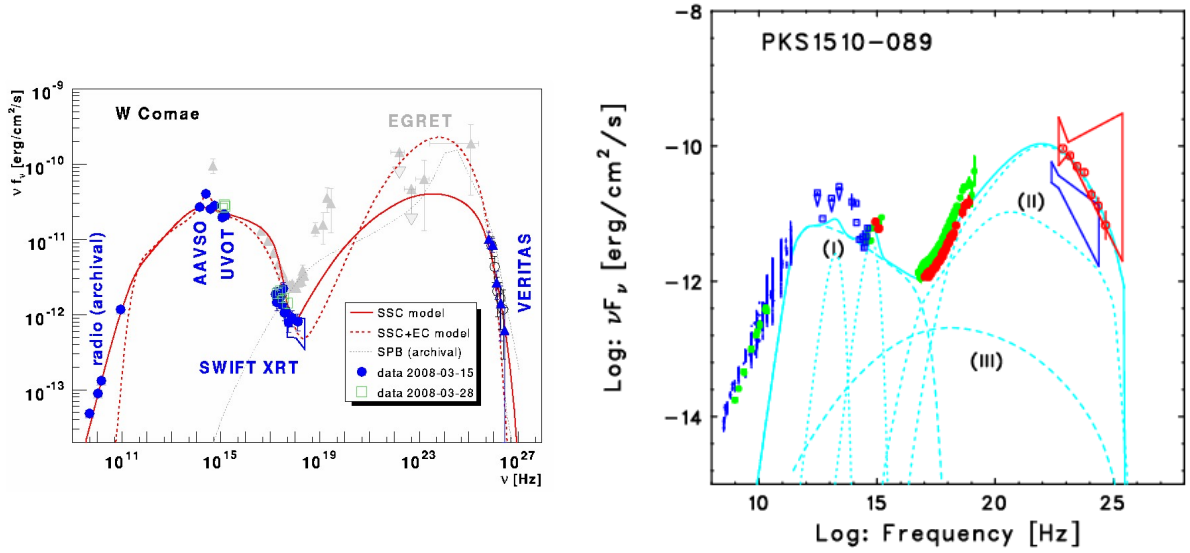

Figure 16: *Broad-band SEDs of the BL Lac W Comae (left, Acciari et al. 2008) and the FSRQ PKS1510-089 (right, Abdo et al. 2010b).*

One way to explain HE emission from blazars could be the inverse Compton scattering of the same electrons responsible for the LE synchrotron peak. From the fact that we observe gamma-rays from both BL Lacs and FSRQs can be inferred that inverse Compton scattering of the general radiation field from the accretion disc of the blazar is unlikely to be the source of the gamma-rays, since this region is very different in the two subclasses (the inner region of FSRQs is far messier, which is why strong emission lines are observed). More probably, relativistic electrons up-scatter their own synchrotron radiation in a process known as the *Synchrotron Self Compton* process, SSC (see, for example, Maraschi et al., 1992).

Nevertheless, external photon sources located outside the jet (i.e. accretion disc, broad line region (BLR), dusty torus) are another good candidate seed photon source for the inverse Compton effect (Dermer & Schlickeiser, 1993; Sikora et al., 2009).

Arguments in favour of this last possibility state that since for FSRQs the LE peak corresponding to synchrotron radiation is located at low frequencies (mostly in the infrared regime) of the SED, electrons from the relativistic jet itself might not be energetic enough to produce VHE photons by means of IC scattering. Therefore, the SSC effect, in which the photons responsible for the LE peak of the SED are also the seed photons for the HE peak, might not be a realistic option for the production of VHE photons. This would mean that the IC effect would be upscattering external photons. But even if one assumes external sources of seed photons, the origin of the HE and VHE emission within blazars is still an open question in which two main opinions are held, namely gamma-rays originating from within the BLR at a sub-parsec scale, EC(BLR), and gamma-rays originating further out from the central SMBH within the hot dust torus (HDT) that surrounds the SMBH at a parsec scale, EC(HDT) (Barnacka et al.,

2013; Brown, 2013).

Much more accurate data are necessary to exactly determinate the emission zone of blazars, though. One method which has been suggested to be the most promising observational discrimination for EC and SSC emission models is the use of Multi Wavelength (MWL) analysis for detection of coeval high-amplitude variability during blazar flares (Sikora et al., 2009).

3. THE EXTRAGALACTIC BACKGROUND LIGHT

The diffuse cosmic radiation from UV to IR wavelengths, also known as the *Extragalactic Background Light* (EBL), is the second most intense source of diffuse radiation in the Universe after the Cosmic Microwave Background (CMB).

The EBL is the integrated flux from all extragalactic sources, including those that are not individually detected. It is the remnant emission of galaxy formation and evolution and it is mainly produced by direct star light (UV and visible range) and light reprocessed by the interstellar dust (IR to sub-millimeter range).

As shown in Figure 17, these two major components are clearly visible in the bimodal SED of the EBL: the first bump corresponds to the *Cosmic Optical Background* (COB) from the radiation emitted by stellar nucleosynthesis, whereas the second bump or *Cosmic Infrared Background* (CIB) is related to the afore mentioned direct starlight being absorbed and re-radiated by dust in the IR domain.

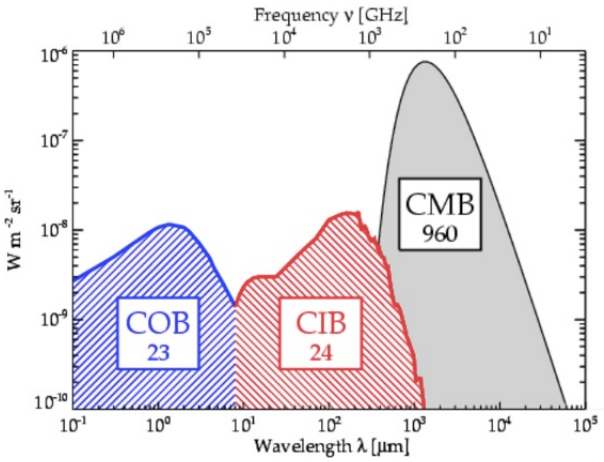

Figure 17: *Illustration of the intensity of the EBL. The CMB is also shown to compare the different wavelengths corresponding to each background radiation. The two components of the EBL, the COB and the CIB are clearly distinguishable. The brightness of each component is is written in boxes (in units of $nW/m^2/sr$). From Dole et al., 2006.*

This type of diffuse background radiation is an important source of opacity for the propagation of (V)HE gamma-ray photons. The LE background photons that compose the EBL (IR and optical photons) can absorb the HE cosmic photons when they travel across the Universe by means of pair production, resulting in an important reduction in the number of photons observed by either space- or ground-based instruments, $(dN_\gamma/dE)_{obs}$ (e.g. Nikishov, 1962; Jelley, 1966; Gould & Schreder, 1967).

Thus, the intrinsic flux $(dN_\gamma/dE)_{int}$ from a source decreases exponentially as a function of the *optical depth* τ (Eq. 9), which is both photon energy E and redshift z dependent.

$$\left(\frac{dN_\gamma}{dE}\right)_{obs} = \left(\frac{dN_\gamma}{dE}\right)_{int} \times e^{-\tau(E,z)} \tag{9}$$

Hence, estimating EBL intensity is an important factor to accurately determine the intrinsic spectrum of a source, particularly for sources emitting in the VHE range since they are the most absorbed by LE EBL photons, and for sources located at high redshifts, since the intrinsic photons have to travel a greater distance through the background radiation field.

To discover the threshold for photon-photon absorption collisions that end up in electron-proton pair production processes, we define the momentum four-vectors of the photons before the collision $\boldsymbol{P}_1$ and $\boldsymbol{P}_2$ as follows:

$$\boldsymbol{P}_1 = [\varepsilon_1/c,\, (\varepsilon_1/c)\boldsymbol{i}_1] \qquad \text{and} \qquad \boldsymbol{P}_2 = [\varepsilon_2/c,\, (\varepsilon_2/c)\boldsymbol{i}_2], \tag{10}$$

where $\varepsilon_1 = h\nu_1$ and $\varepsilon_2 = h\nu_2$ are the energies of the photons before the collision. According to the laws of conservation, the four-momentum before and after the collision has to be conserved,

$$\boldsymbol{P}_1 + \boldsymbol{P}_2 = \boldsymbol{P}_3 + \boldsymbol{P}_4, \tag{11}$$

$\boldsymbol{P}_3$ and $\boldsymbol{P}_4$ being the four-momenta of the created particles. To find the pair-production threshold, we assume that the particles are created at rest. Hence, their respective four-vectors are

$$\boldsymbol{P}_3 = [m_e/c, 0] \qquad \text{and} \qquad \boldsymbol{P}_4 = [m_e/c, 0]. \tag{12}$$

By squaring both sides of Eq. 11, one gets

$$\boldsymbol{P}_1 \cdot \boldsymbol{P}_1 + \boldsymbol{P}_2 \cdot \boldsymbol{P}_2 + 2 \cdot \boldsymbol{P}_1 \cdot \boldsymbol{P}_2 = \boldsymbol{P}_3 \cdot \boldsymbol{P}_3 + \boldsymbol{P}_4 \cdot \boldsymbol{P}_4 + 2 \cdot \boldsymbol{P}_3 \cdot \boldsymbol{P}_4. \tag{13}$$

Bearing in mind that the norm of the momentum four-vector of a photon is equal to zero, $\boldsymbol{P}_1 \cdot \boldsymbol{P}_1 = \boldsymbol{P}_2 \cdot \boldsymbol{P}_2 = 0$, Eq. 13 is simplified to

$$2 \cdot \boldsymbol{P}_1 \cdot \boldsymbol{P}_2 = \boldsymbol{P}_3 \cdot \boldsymbol{P}_3 + \boldsymbol{P}_4 \cdot \boldsymbol{P}_4 + 2 \cdot \boldsymbol{P}_3 \cdot \boldsymbol{P}_4. \tag{14}$$

In addition, from Eq. 12 we see that $\boldsymbol{P}_3 = \boldsymbol{P}_4 = [m_e/c, 0]$. Therefore, Eq. 14 becomes

$$\begin{aligned} 2 \cdot \boldsymbol{P}_1 \cdot \boldsymbol{P}_2 &= 2 \cdot \boldsymbol{P}_3 \cdot \boldsymbol{P}_3 + 2 \cdot \boldsymbol{P}_3 \cdot \boldsymbol{P}_3 \\ &= 4 \cdot \boldsymbol{P}_3 \cdot \boldsymbol{P}_3 \end{aligned} \tag{15}$$

Next, inserting the values of the four-momenta of the photon, we get

$$2 \cdot \left(\frac{\varepsilon_1 \varepsilon_2}{c^2} - \frac{\varepsilon_1 \varepsilon_2}{c^2} \cos\theta \right) = 4 {m_e}^2 c^2, \tag{16}$$

where θ is the angle between the two initial photons. If we isolate the variable ε_2 from the last equation,

$$\varepsilon_2 = \frac{2 {m_e}^2 c^2}{\varepsilon_1 (1 - \cos\theta)}, \tag{17}$$

we see that the incident direction threshold angle for electron-positron pair production is $\theta = \pi$, that is, the threshold for the process happens for head-on collisions. Thus, the energy threshold for pair-production via photon-photon absorption is

$$\varepsilon_2 \geq \frac{2 {m_e}^2 c^2}{\varepsilon_1} = \frac{0.26 \times 10^1 2}{\varepsilon_1} \,\text{MeV}. \tag{18}$$

Note that this process provides not only a mechanism to create electron-positron pairs, but also a major source of opacity for HE and VHE gamma-rays. For instance, a ε=100 GeV gamma-ray would give rise, and hence, be absorbed, to electron-positron pairs after

colliding with starlight photons (UV and visible range) of ε=2 eV that compose the EBL.

A direct estimate of the EBL intensity can be obtained by subtracting the emission corresponding to foreground sources from the total emission. Such estimations have already been done for the sub-millimetre range (e.g. Puget et al., 1996; Hauser et al., 1998; Hauser & Dwek, 2001). However, it has proved to be a daunting task in the IR range, due to *foreground contamination* from, for example, the zodiacal light[11]. This contamination can result in an overestimation of the EBL intensity.

Therefore, upper and lower limit calculation has usually been the approach taken by scientists. Upper limits have been obtained by observing the isotropic emission component (e.g. Hauser & Dwek, 2001). On the other hand, strict lower limits have been achieved from integrated galaxy number counts (e.g. Fazio et al., 2004). Lower limits obtained from source counts are usually one order of magnitude below limits from direct measurements.

Extragalactic VHE gamma-ray sources can be used to derive strong constraints on the EBL density, due to the opacity mentioned above. EBL absorption is expected to leave a unique imprint in the detected spectra of the sources. This signature is predicted to be both redshift and energy dependent (Abramowski et al., 2012), as can be inferred from Eq. 9. For the first peak of the SED, the COB, the absorption is expected to produce a weak modulation in the spectra for the range from $\approx$ 100 GeV to 5-10 TeV, while a sharp cut-off is envisaged as a result of the CIB absorption at energies $E \geq$5 to 10 TeV.

By analysing the attenuated gamma-ray flux detected on Earth, and assuming there is no intrinsic break in the energy range of interest (Stecker et al., 1992) and that the spectrum has a limited hardness, constraining upper limits on the EBL opacity to gamma-rays have been obtained (e.g. Aharonian et al. 2006; Mazin & Raue, 2008). EBL models so far agree with these derived limits, resulting in a consistent value for the gamma-ray opacity (e.g. Dominguez et al., 2011).

In their paper of 2012, Abramowski et al. analysed the spectra of the brightest extragalactic blazars detected by HESS (*High Energy Stereoscopic System*, see Section 4.5) with a maximum likelihood method in search of signatures of the EBL. Instead of the upper limits obtained in previous analysis, they obtained a direct measurement of the optical depth in a joint fit of the optical depth itself and the intrinsic spectra of the sources.

For the predictions made in this work, it was essential to consider the effect of the EBL. The spectra obtained from *Fermi* data were extrapolated to the energy range of CTA, and afterwards corrected for the impact of EBL so that they could be compared to the sensitivity curves of the future ground-based detectors. The EBL model proposed by Franceschini et al. (Franceschini et al., 2008) was implemented for the analysis.

[11] Faint, roughly triangular, diffuse white glow seen in the night sky, which appears to extend up from the vicinity of the Sun along the ecliptic (the apparent path of the Sun on the celestial sphere). It is caused by sunlight scattered by space dust in the zodiacal cloud.

In their model, Franceschini et al. modelled the extragalactic optical and infrared backgrounds using available information on cosmic sources in the universe from far-UV to sub-millimeter wavelengths over a wide range of cosmic epochs. They applied relevant cosmological survey data (e.g. number counts, redshift distributions, luminosity functions) from ground-based observatories in the optical, near-IR, and sub-millimeter, as well as multi-wavelength information coming from the HST, ISO and Spitzer space telescopes, and also direct measurements or upper limits on the extragalactic backgrounds by dedicated missions such as COBE, were implemented to set constraints to the EBL.

Data were fitted and interpolated with a multi-wavelength backward evolutionary model. In this way, they were able to estimate the background photon density and its redshift evolution. From the redshift-dependent background spectrum, they calculated the photon-photon opacities for sources of HE emission at any redshifts. The same results can also be used to compute the optical depths for any kind of processes in the intergalactic space involving interactions with background photons, which is very useful for our EBL correction.

4. GAMMA-RAY DETECTORS

As seen in Chapter 1, when gamma-rays travel through matter, they can undergo a variety of processes (Compton scattering, photoabsorption, pair-production, etc.) which create VHE charged particles from the gamma-ray. Different gamma-ray detection techniques can be implemented using these interactions.

In this chapter, a summary of the main types of gamma-ray detectors is presented, along with examples of each type of telescope. A more detailed attention is paid to the last two types (atmospheric Cherenkov telescopes and pair-production telescopes), since they correspond to the two observational facilities considered in this work, CTA and *Fermi*-LAT.

1. Satellite-based detection techniques

1.1 Scintillation Detectors

Scintillation detectors consist of a material which emits LE photons (usually in the optical range of the EM spectrum) when hit by a HE charged particle, that is, they convert gamma-ray photons into optical ones. The scintillation crystal absorbs the gamma-ray and re-emits it into the visible part of the EM spectrum.

When a gamma-ray passes through a scintillation material, it can interact with the scintillator through one of the standard three mechanisms - photoelectric effect, Compton scattering, or pair production (note that pair production is only possible if the energy of the gamma-ray is greater than 1.022 MeV, i.e. the sum of the rest mass energies of the created electron/positron pair). All of these processes produce energetic electrons that produce a large number of ionized atoms as they pass through the crystal. Most of the secondary electrons produced inthis way recombine, generating photons in the ultraviolet part of the spectrum.

That means that, when used as a gamma-ray detector, a scintillator detector does not detect the gamma-ray directly. Instead, it detects the LE photons created from the

interaction between the HE charged particles and the scintillation crystals. These LE photons are collected by Photo-Multiplier Tubes (PMTs) (Figure 18). These PMTs absorb the light emitted by the scintillator, and convert it into electrons via photoelectric absorption (Section 1.1). The energy of the incoming gamma-ray can be determined by the sum of the energies collected by the surrounding PMTs.

Most common scintillators used for gamma-ray detection are made of inorganic materials, usually an alkali halide salt (e.g. sodium iodide, NaI, or caesium iodide, CsI). An impurity such as thallium is often added to increase the detection capabilities of these semiconductor materials. This leads to detectors described as NaI(Tl) - sodium iodide crystal with thallium activator- or CsI(Na) - caesium iodide crystal with sodium activator.

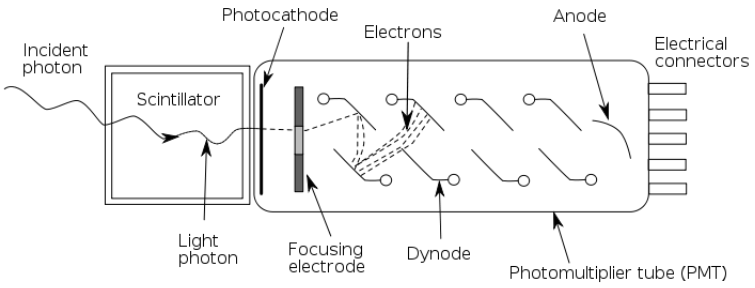

Figure 18: *Schematic of a basic scintillation detector. The photocathode where the LE photons created from the interaction between the gamma-ray and the crystals are converted into electrons via photoelectric effect can be seen. These photoelectrons then travel through the PMT tube towards the anode and the electrical connectors which record the output information [65].*

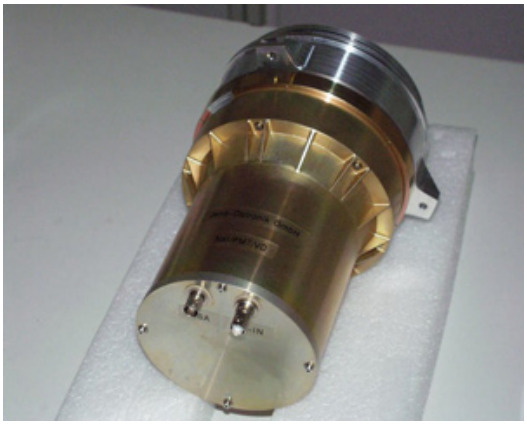

Figure 19: *Picture of one of the GBM detectors aboard the Fermi spacecraft. Credit: NASA.*

Examples of Scintillation Detectors: CGRO and HEAO-1

Missions as the Compton Gamma-Ray Observatory (CGRO) or the first High Energy Astrophysical Observatory (HEAO-1) have used gamma-ray detectors based on inorganic scintillators. For instance, the Gamma-Ray Burst Monitor (GBM) on board of the *Fermi* spacecraft (Figure 19) consists of 12 NaI scintillators and 3 bismuth germanate detectors for its monitoring procedures, and it is sensitive to gamma-ray photons from a few keV to 25 MeV.

1.2 Solid State Detectors

Solid state gamma-ray detectors are very similar to scintillation detectors, but the semiconductor materials implemented in the former are more sophisticated (e.g. germanium, Ge, or cadmium zinc telluride, CdZnTe). These new materials offer better energy resolution, less noise and better spatial resolution, providing a more accurate acquisition of data. However, their maintenance is more complicated than for the standard scintillators (Ge detectors require cooling to operating temperatures). Besides, they are usually more expensive.

Similarly to scintillators, the operating principle of solid state detectors is the photoelectric ionization of the material by the incoming gamma-ray. The difference is that, while in a scintillator the gamma ray creates electron/ion pairs, in a solid state detector electron/hole pairs are created.

Example of solid state detector: The INTEGRAL mission

The primary spectrometer in the INTErnational Gamma-Ray Astrophysics Laboratory (INTEGRAL), the SPectrometer for Integral (SPI), is made of a coded mask of hexagonal tungsten tiles, above a detector plane of 19 germanium crystals, which are cooled with a mechanical system (Figure 21). The sensitivity obtained is in the range between 2 keV and 1 MeV.

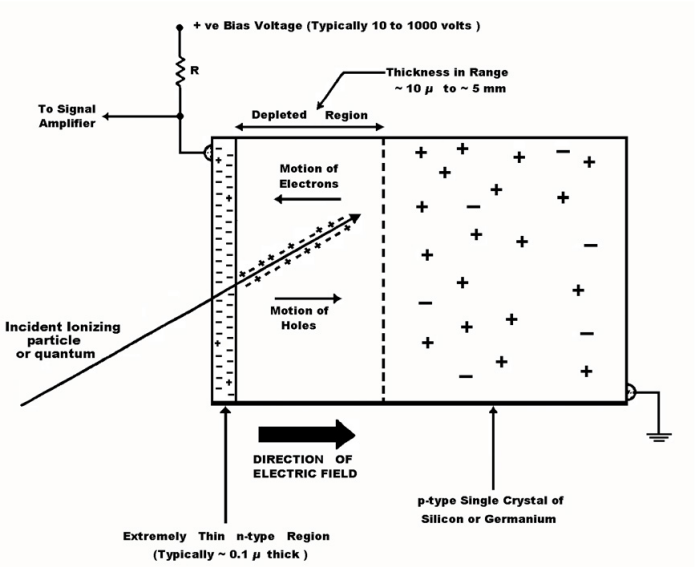

Figure 20: *Scheme of a solid state detector. The incoming gamma-ray triggers a transport of charge carriers (either electrons or holes) in the diode (a single p-n junction) which leads to a change in the potential difference across the depletion zone. If the absorption of the gamma-ray occurs in the junction's depletion region, carriers are swept from the junction by the built-in electric field of the depletion region, creating an electric current. By determining the total current through the photodiode, the initial energy of the photon can be determined [66].*

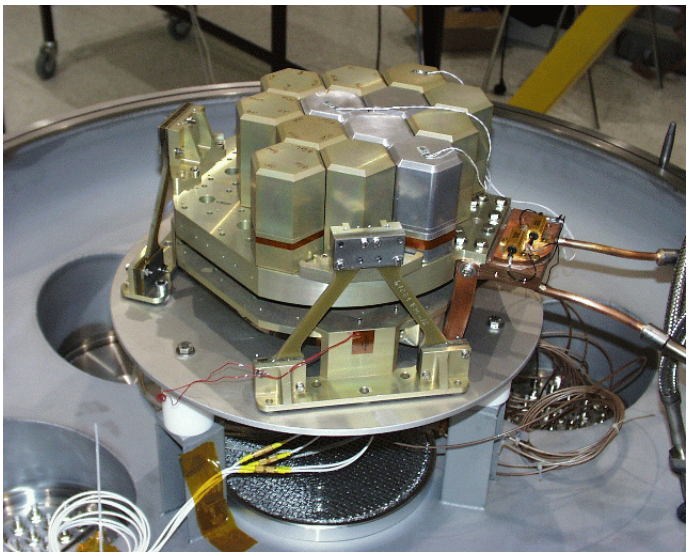

Figure 21: *Picture of the setup of SPI telescope in the INTEGRAL project. The hexagonal form of the tungsten tiles and the germanium detectors can be clearly seen [67].*

1.3 Compton Scattering Detectors

The energy range from about 1 to 30 MeV is where Compton scattering is the dominant physical interaction. As seen in Section 2.2, this phenomenon occurs when a LE electron is scattered by a HE photon, leading to energy transference from the photon to the charged particle. This interaction is the basis of the Compton Scattering detection method. The Compton scattering energy band is also the region where some active galaxies and pulsars have been detected strongly, and where nuclear emission lines can be detected. Furthermore, gamma-ray bursts and flares from the Sun are often detected in this range.

Compton scattering telescopes usually consist of two levels. First, the incident cosmic gamma-ray photon Compton-scatters a resting electron from the scintillator in the top level. The scattered photon then proceeds to a lower level of scintillation material in which it is totally absorbed. The points at which the interaction happened in both levels, along with the energy transference occurred in each layer, can be determined with PMTs (see Figure 22).

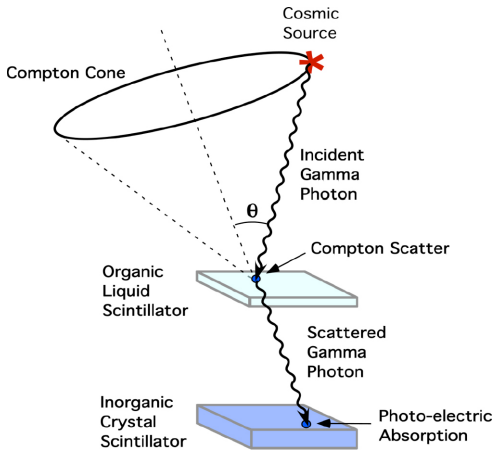

Figure 22: *Scheme of the basic principle of Compton Scattering Telescopes. Note that the line between the first layer/interaction and the second layer/interaction does not point directly to the initial direction of the incoming gamma-ray. However, the angle of incidence of the photon relative to this line can be determined by applying the Compton scattering law [68].*

The Compton scattering law provides a relationship between the angle and energy of the of the scattered electron (first level) and the scattered photon (measured in the second level) as follows,

$$\lambda_f - \lambda_i = \frac{h}{m_e c}(1 - \cos\theta). \tag{19}$$

From Figure 22, it is evident that the line between the two levels of interaction does not correspond with the direction of the incoming photon. However, applying Eq. 10, it is possible to determine the angle of incidence of the initial cosmic photon relative to this line. The azimuthal direction of the incoming photon cannot be calculated this way though, meaning that the photon could come from any point in a ring on the sky (the point-spread function of the telescope, i.e. the probability of an event coming from a certain area on the sky). As a result, data from Compton telescopes are quite difficult to analyse.

Regarding their structural characteristics, these detectors have good energy resolution (about 5-10%), which is bounded by uncertainties in the measurement of the energy deposited in each layer of the telescope. Compton telescopes also have wide fields-of-view and relatively small effective areas, due to the fact that very few incident photons actually Compton-scatter in the top level. This reduces a physical area of several thousand cm^2 to an effective area of a few tens of cm^2.

Future Compton scatter telescopes will implement some mechanism which allows data regarding the final direction of the scattered electron to be gathered in the first layer, obtaining a complete solution for the trajectory of the cosmic gamma-ray photon.

Example of Compton scattering detector: The COMPTEL telescope

Compton scatter telescopes have been largely experimental in design. The most advanced and successful instrument is the so-called COMPTEL (COMPton TELescope) aboard NASA's Compton Gamma-Ray Observatory, a schematic of which can be seen in Figure 23.

Sadly, the implementation of Comptel revealed higher than expected instrumental background and also poor angular resolution (Schönfelder & Gottfried, 2010), as can be appreciated in Figure 24.

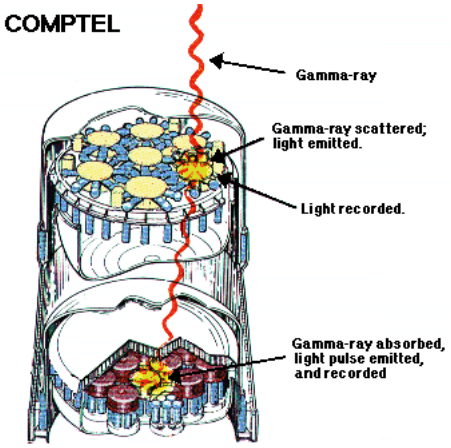

Figure 23: *Sketch of the Compton scatter telescope on board NASA's Compton Gamma-Ray Observatory. Image credit: NASA.*

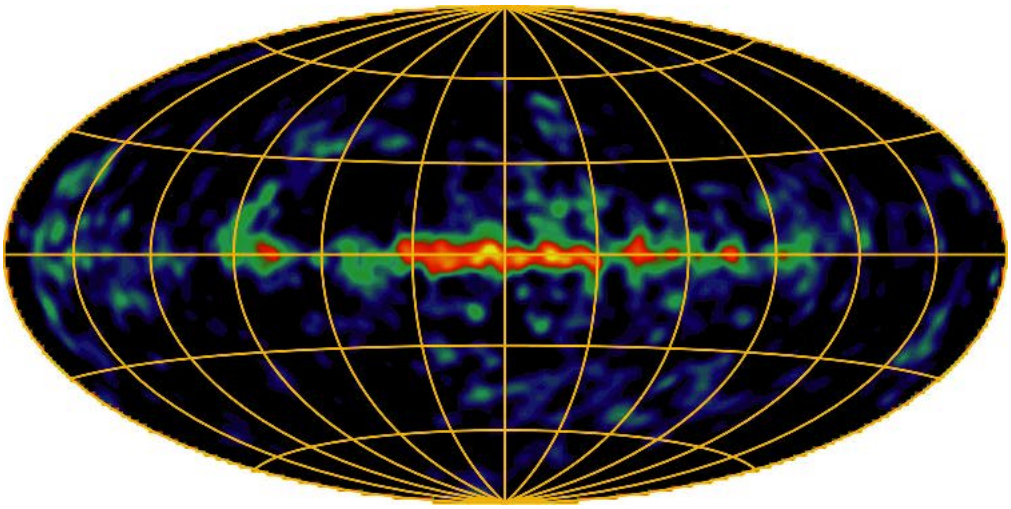

Figure 24: *All-sky map from Comptel. The poor angular resolution is clearly noticeable. Image credit: Comptel collaboration.*

1.4 Pair-production Detectors

At energies above 30 MeV, the dominant photon interaction is pair production (Section 1.5) for most materials. Pair-production telescopes use this process to detect the incoming cosmic gamma-ray photons through the detection of the electron-positron pair created in the detector.

Pair telescopes are designed as layered telescopes, with converter layers usually made of a heavy metal (where the photons are turned into electron-positron pairs) interleaved with tracking material (where the electrons and positrons are detected).

There are two main types of tracking devices. One is a *spark chamber*, consisting of a gas-filled region crossed with wires. Once the pair is created in a converter layer, both particles cross the chamber, ionizing the gas along their path. The ionization triggers the detector to electrify the wires, creating the detected signal. The paths followed by the particles can be reconstructed from the trail of sparks inside the chamber.

The other type of tracker is made of silicon strip detectors. These detectors consist of two planes of silicon, one of which has the strips oriented in the x direction, whereas in the other the strips are oriented in the y direction. The direction and origin of the initial gamma-ray can be determined by reconstructing the tracks of the charged particles through a vertical array of trackers. Moreover, the total energy of the incoming photon can be obtained either by the analysis of the scattering of the pair or by a calorimeter after the particles exit the spark chamber.

Initially, spark chambers where widely used to detect cosmic-rays. Unsurprisingly, an overwhelming number of cosmic-rays is also detected when searching for genuine gamma-ray photons. To prevent cosmic-rays triggering the spark chamber, pair telescopes feature an anti-coincidence detector covering the entire instrument, as can be seen in Figure 25 . The anti-coincidence shield detects charged particles before they enter the chamber, preventing them from triggering the detector, so that the telescope only detects actual gamma-rays.

The energy resolution when the detector is a spark chamber is worsened both at low gamma-ray energies and at very high gamma-ray energies. For the lowest limit, particles lose energy through multiple scattering while they travel across the detector, whereas at very high energies the electron-positron pair might be incompletely absorbed by the calorimeter. Both issues reduce the energy resolution of the detector down to a meagre 20%. If silicon strip detectors are used, the energy resolution can be improved to 10%.

As with atmospheric Cherenkov telescopes, pair telescopes have to be as large as possible in order to detect the scarce VHE photons. To improve the energy resolution of these telescopes, larger collection areas have to be implemented, which would allow space-based gamma-ray detectors to observe sources up to 100 GeV, a threshold compatible with observations made by ground-based atmospheric Cherenkov telescopes.

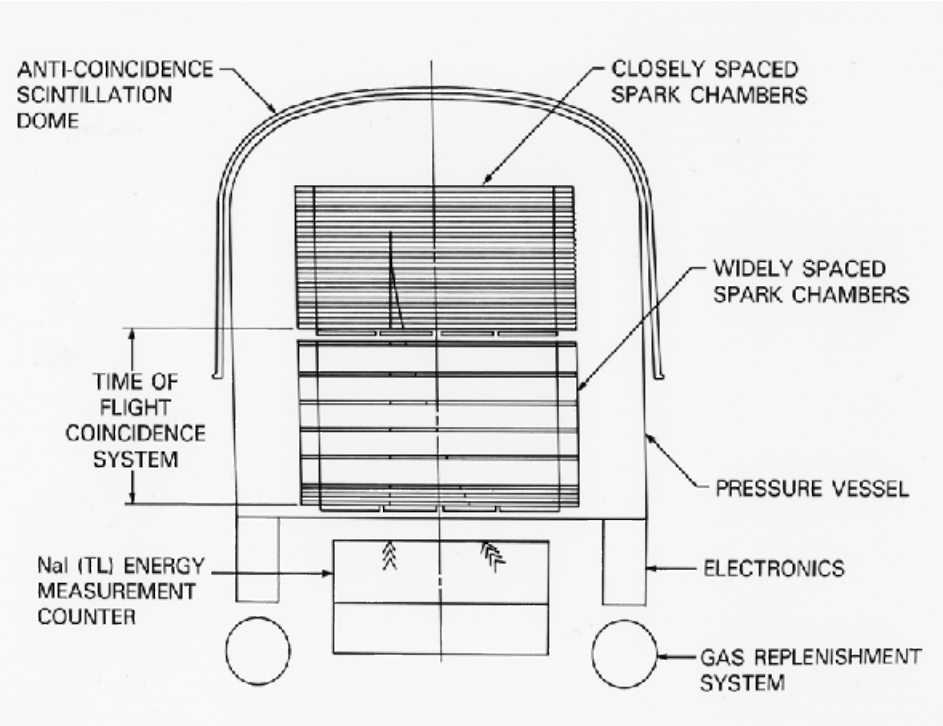

Figure 25: *Scheme of the pair detector used in EGRET (Energetic Gamma-Ray Experiment Telescope). The anticoincide detector, the spark chamber and the calorimeter used for detecting clean events can be clearly seen in the diagram. Image credit goes to CGRO Science Support Centre.*

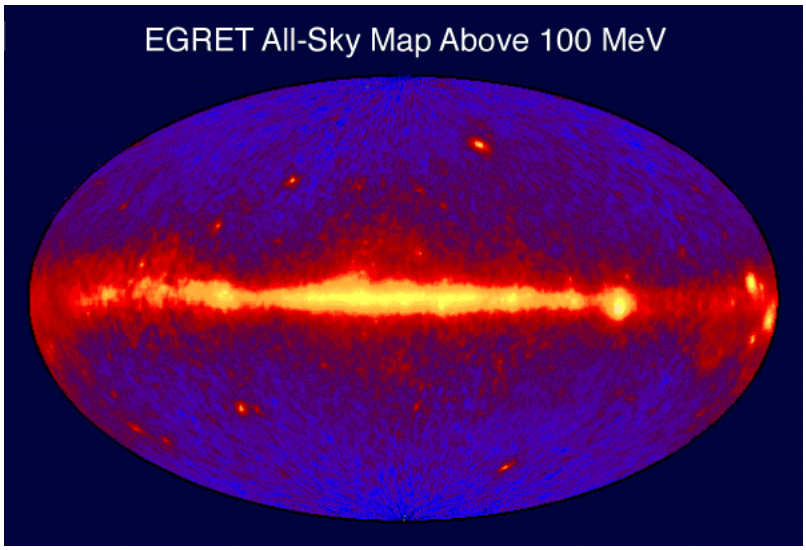

Figure 26: *All-sky image from EGRET. Credit: EGRET team.*

Example of pair-production detector: The Fermi Gamma-Ray Space Telescope

On 2008 June 11th, the *Fermi* Gamma-Ray Space Telescope (Figure 27), an international space mission that studies the Universe in the energy band from 10 keV to 300 GeV, was launched. Aboard the spacecraft is the most advanced space-based gamma-ray telescope, which consists of two instruments: the main *Large Area Telescope* (LAT), an imaging, wide field-of-view gamma-ray telescope, and a secondary instrument devoted to the study of gamma-ray bursts, the *Gamma-ray Burst Monitor* (GBM). The data from the mission are publicly available from the *Fermi* Science Support Centre (FSSC, [70]).

The primary instrument, the LAT, which covers an energy range from 20 MeV to 300 GeV and is described in detail in Atwood et al., 2009 , is a silicon strip pair-conversion telescope. The large field of view of the LAT, $\simeq 2.4$ sr , its improved angular resolution, $\simeq 0.8^{\circ}$ at 1 GeV, and its large effective area, $\simeq 8000$ cm^2 on axis at 10 GeV, provide an order of magnitude improvement in performance compared to its predecessors.

The large field of view and effective area, in combination with the *all sky survey* mode by which the satellite points away from the Earth and rocks North and South of its orbital plane, enables a scan of the entire sky in about three hours or 2 orbits of the satellite (Ritz, 2007).

The LAT instrument can be subdivided into four parts or subsystems previously mentioned, namely the *tracker/converter*, the *calorimeter*, the *anti-coincidence detector* and the *data acquisition system*, as shown in Figure 28.

Figure 27: *LAT on the payload attach fitting. NASA/ Jim Shiflett.*

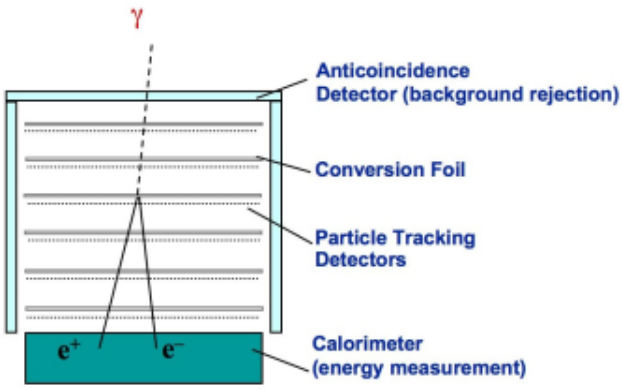

Figure 28: *A sketch showing the subsystems composing the LAT instrument aboard the Fermi Gamma-Ray Space Telescope. Image credit: Fermi collaboration.*

TRACKER/CONVERTER (TKR)

In the TKR of the LAT, converter planes are interleaved with position sensitive detectors that record the passage of charged particles, measuring the tracks of the particles resulting from pair conversion. Incident gamma-ray photons preferentially convert in one of the tungsten foils, and the resulting electron/positron particles are tracked by the Silicon Strip Detectors (SSDs) through successive planes. The tracks of the particles are used for reconstructing the direction of the triggering gamma-ray. Moreover, the pair conversion signature is also used to help rejecting the background of cosmic rays. The advanced technology implemented in the TKR enables straightforward event reconstruction and determination of the incident photon. The TKR is made up of an array of four-by-four tower modules, each tower consisting of 18 layers of Silicon Strip Detector (SSD) planes with interleaved tungsten foils.

CALORIMETER (CAL)

Composed of 8.6 radiation lengths of CsI(TI) scintillation crystals stacked in 8 layers, the CAL has two main goals: to measure the energy deposition caused by the EM particle shower resulting from the electron/positron pair produced by the incoming gamma-ray, and to image the shower development profile, providing an important background discrimination (since the energy deposition of cosmic rays is different from that of gamma-rays) and an estimation of the shower energy leakage fluctuations.

ANTICOINCIDENCE DETECTOR (ACD)

The ACD in the LAT consists of plastic scintillation tiles covering the whole LAT instrument. These tiles are triggered when scintillation light caused by charged cosmic particles (i.e. cosmic rays) is detected, so that the ACD can provide charged particle background detection. The ACD is segmented in order to avoid the *backsplash effect* caused by the large mass (≈1800 kg) of the CAL necessary to measure photon energies at the HE limit of the LAT (around 300 GeV). The backsplash effect is caused by isotropically distributed secondary particles (mostly 100 - 1000 keV photons) from the EM shower that can Compton scatter in the ACD and hence create false signals from the recoil electrons. This effect was observed in EGRET, and the afore mentioned segmented design was implemented, so that only the ACD segment nearby the incident photon may be considered, reducing the area of the ACD that could contribute to backsplash (Moriseev et al. 2004).

***DATA ACQUISITION SYSTEM* (DAQ)**

Made of specialized electronics and microprocessors, the DAQ collects information from the previous subsystems and conducts the first filtering of *clean* events (events triggered by genuine gamma-rays), in order to decide whether the detected signal is *good* enough (the signal follows the pattern of a genuine gamma-ray) to be sent to the ground.

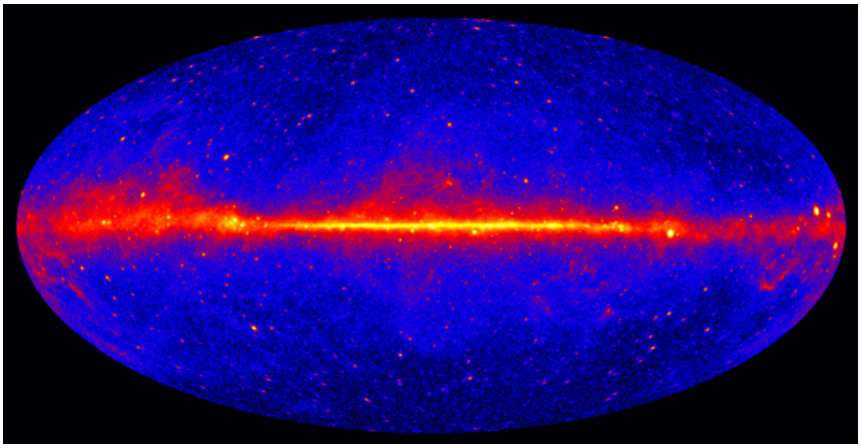

Figure 29: *All-sky image constructed from 5 years of observation with Fermi Gamma-Ray Telescope. Brighter colors show brighter gamma-ray sources. The galactic planes is clearly dominating the gamma-ray sky. The majority of AGN detected are located off the plane. Image credit: NASA/DOE/Fermi LAT Collaboration.*

The implementation of these high-technology systems has enabled *Fermi* to fulfil its expectations from the very beginning. For instance, during its first year of operation *Fermi* discovered around 1500 gamma-ray sources comprising AGN, pulsar wind nebulae, supernova remnants and other objects (see Figure 29). According to the Second *Fermi* LAT Catalogue (Nolan et al., 2012), 395 BL Lacs objects and 310 FSRQs from a total of 886 AGN have so far been detected.

With its minimum active period of five years (2008-2013) over, the mission is now half way through its intended time line of 10 active years. The fact that *Fermi*-LAT will be operating when the CTA project enters its active phase will probably be of great usefulness, since both instruments overlap in the region between 10-100 GeV (Funk & Hinton, 2013), and meaningful information about the performance of CTA can be foreseen given the data we get from *Fermi* (see Chapters 5-7 of this work).

Table 2: Summary of the mentioned satellite-based gamma-ray missions

NAME	LIFETIME	DETECTOR TYPE	ENERGY RANGE	DETECTOR AREA
HEAO-1/A4	Aug 1977 - Jan 1979	Scintillators	0.3-10 MeV	120 cm^2
EGRET/CGRO	Apr 1991 - Jun 2000	Spark chambers, NaI(Tl) crystals & plastic scintillators	20 MeV-30 GeV	1500 cm^2
COMPTEL/CGRO	Apr 1991 - Jun 2000	Compton Scattering	0.75-30 MeV	20-50 cm^2
SPI/INTEGRAL	Oct 2002 - Active	Solid State	18 keV-8 MeV	500 cm^2
FERMI/LAT	Jun 2008 - Active	Pair Production	10 keV-300 GeV	8000 cm^2

Examples of different satellite-based gamma-ray telescopes

2. Ground-based detection techniques

2.1 Atmospheric Cherenkov telescopes

The absorption suffered by gamma-rays when they enter the atmosphere is a problem for typical gamma-ray detectors, which have to be flown in, for instance, a balloon to a height where the influence of the atmosphere is minimized. In contrast, Atmospheric Cherenkov telescopes use the atmosphere as a part of the detector.

When a gamma-ray enters the Earth's atmosphere, it produces an electron/positron pair in the Coulomb field of an atmospheric (e.g. Nitrogen) atom. This particles then interact via Bremsstrahlung, creating further HE photons. This process will continue until a certain energy threshold is reached[12], and a so-called *particle air shower* or *cascade* is obtained, as in Figure 30.

Even if nothing can travel faster than light *in a vacuum*, the speed of light is reduced when it travels through a medium such as glass, water or air. As the particles created in the gamma shower are extremely energetic, they travel at speeds greater than that of light in the *medium of the atmosphere*. The relativistic charged particles polarize the atoms from the atmosphere as they cross their vicinity, resulting in the so-called *Cherenkov radiation*, a faint, bluish light named after Pavel Cherenkov.

[12] As seen in Section 4 of Chapter 1, a rough estimate to the energy threshold for Bremsstrahlung processes is given by $E_c = 800\,\mathrm{MeV}/(Z + 1.2)$.

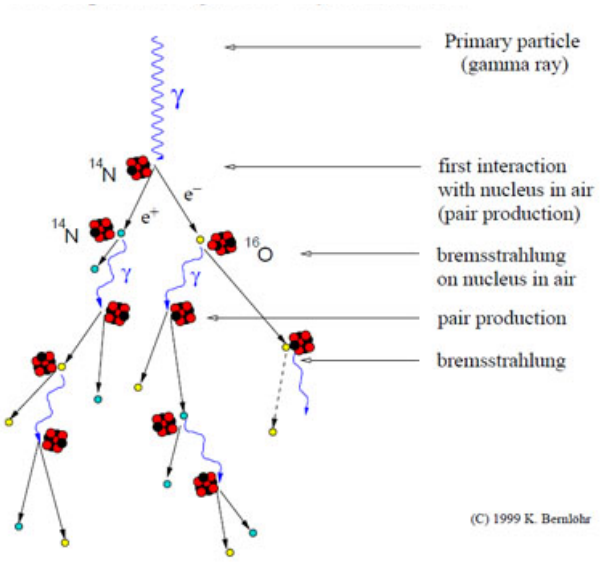

Figure 30: *Scheme of a gamma-ray shower originated by the photon interacting with the molecules from the Earth's atmosphere. Image credit: K. Bernlöhr.*

The total number of Cherenkov light photons created in a gamma shower is about proportional to the initial gamma-ray photon energy ($\simeq$ 50000 ph/GeV). Although Cherenkov photons are emitted all along the air shower at different heights and times, they arrive almost simultaneously (within few nanoseconds), because the particles and the light propagate with almost the same velocity.

Atmospheric Cherenkov detectors basically detect the 'pool' of Cherenkov light which accompanies the particle shower. This affects both to the effective area of the telescope and to the quality of the mirrors. On the one hand, the collection area is roughly the area of the light pool at the detector altitude, which can reach up to 50000 m^2 for gamma-ray detection. Note that for pair-production telescopes this area is far smaller than the cross-section of the telescope (e.g. 8000 cm^2 on axis at 10 GeV is the effective area of *Fermi*, 1600 cm^2 for EGRET). On the other hand, the mirrors used for these detectors do not need to be such high-quality as the ones in optical telescopes: Cherenkov telescopes image the light of the pool instead imaging an astronomical source.

The light of the Cherenkov light pool reflected by the mirror of the telescope is then detected in the focal plane by PMTs, so that the detection of the gamma-ray event can be recorded. As the Cherenkov light of the pool is very faint, and the detectors are very sensitive, clean detections can only be made on dark, moonless nights, which reduces the observation period of this type of telescope.

Once the light has been detected in a PMT, fast electronics are used to record the signal. In this way, a crude image of the Cherenkov light pool is recorded. Recording the light pool is paramount since apart from cosmic gamma-rays, these detectors also detect the important cosmic-ray background. Despite being charged particles instead of

photons, these interact with the atmosphere in a similar way to photons. Consequently, cosmic-ray showers produce Cherenkov light pools too, which mask the desired signal from the gamma-rays; indeed, over 99% of detected events are triggered by cosmic-rays.

Although both types of showers create Cherenkov light pools, simulations such as that illustrated in Figure 31 show that pools from gamma-ray primaries have a smaller angular distribution and an ellipsoidal shape that aligns itself with the direction of the incoming photon, whereas cosmic-ray induced showers present broader and not so well-aligned Cherenkov light pools. Cosmic-ray contamination can be mostly removed by selecting the showers that show the features of those induced by gamma-rays.

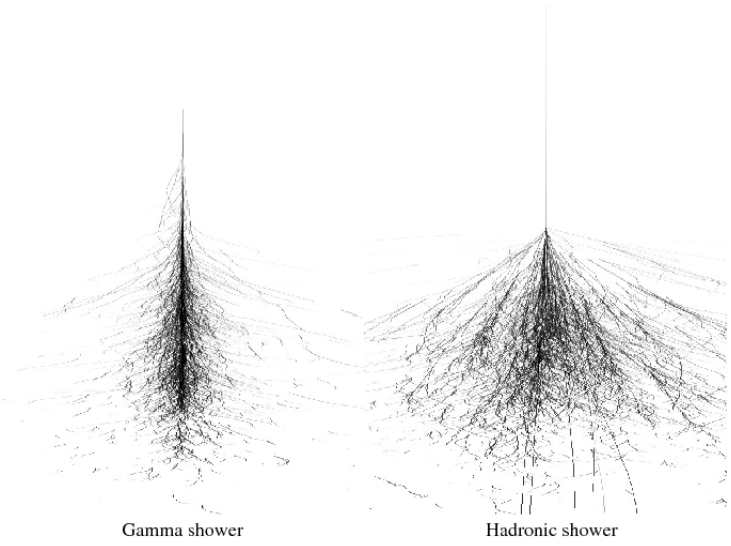

Figure 31: *Imaging of a gamma-ray induced particle cascade (left) and cosmic-ray induced shower (right). Gamma-rays create narrower showers that are more aligned with the direction of the incoming photon [69].*

One of the best features of this type of gamma-ray telescope is that their collection area is not the area of the mirror, but the *size of the pool* on the ground. The event can be detected so long as the detector is *inside* the Cherenkov light (Figure 32). Hence, atmospheric Cherenkov telescope have much larger collection areas than satellite-based telescopes such as *Fermi*-LAT (Section 4.4). Having large collection areas makes this type of telescope very effective in terms of detecting VHE photons (order of TeV), since the number of photons emitted by sources decreases rapidly with increasing energy.

Unfortunately, incident photon energy is hard to determine with atmospheric Cherenkov telescopes. The energy of the incoming photon can be estimated with an accuracy up to 30-40%. On the other hand, time resolution is quite good, as the arrival time of a shower can be determined with an accuracy of sub-microseconds.

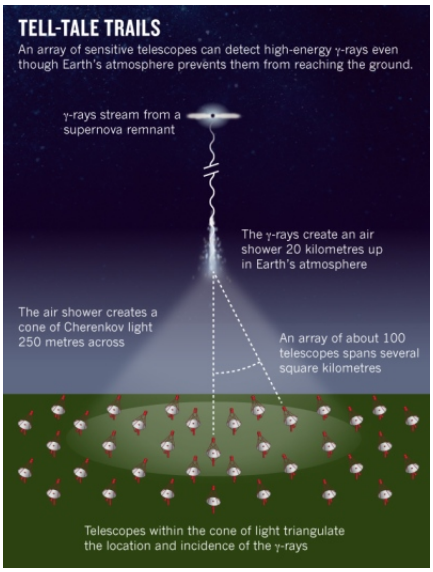

Figure 32: *Schematic detection of a gamma-ray coming from a source, a supernovae remnant concretely. The Cherenkov light pool is detected by the telescopes located both totally and partially inside the light cone. Image credit: Eugenie Samuel Reich.*

In the past, 'on/off' observations were used with such detectors in order to detect a source. In this mode of observation, the detector first looked at a region of the sky containing the source of interest for a period of time, followed by a period of observing a background region. A significant difference between the number of events detected in the on/off observations meant the detection of a source. However, this technique has lately been developed to a more accurate one with the advent of imaging detectors. Latest atmospheric Cherenkov detectors have a big enough field-of-view that enables observing the source simultaneously with sufficient background regions.

As for all gamma-ray telescopes, larger is better. This applies especially to the less energetic gamma-rays that reach the atmosphere. LE gamma-rays they produce less bright Cherenkov light, so even if the number of events in the LE range is larger than in the HE range, individual telescopes with large mirror areas are fundamental in order to detect the fainter light cones. Current leading facilities such as HESS-2 in Namibia, which features 5 *Imaging Atmospheric Cherenkov Telescopes* (IACT) (Figure 33), have provided invaluable observations of the Universe in the VHE band. The future of ground-based atmospheric Cherenkov telescopes lies in the construction of CTA in the following years. With a much larger collection area, it will improve the measurement of image parameters, as well as decreasing the energy threshold of the detectors and improving their sensitivity and angular and energy resolution.

Figure 33: *The five IACTs composing the HESS observatory next to the Gambsberg mountain in Namibia, a place well known for its splendid observational conditions. Image credit: HESS collaboration.*

Example of IACT: The Cherenkov Telescope Array

The CTA project is a worldwide collaboration aimed at building the next generation of ground-based gamma-ray open observatory. CTA will explore the most energetic aspects of the non-thermal VHE Universe, deepening our understanding of the physical phenomena occurring at energies above 10 GeV.

CTA is expected to supersede the current generation of ground-based IACTs (HESS, MAGIC and VERITAS) by improving on the sensitivity by a factor of 5 to 10, and by extending the observable energy range from below 100 GeV to above 100 TeV. In close collaboration with observatories in other wavelengths, CTA will cast light upon topics regarding cosmic non-thermal processes in HE astrophysics, from the acceleration mechanisms in black holes to the search for dark matter and quantum gravity.

As previously mentioned, a larger number of telescopes means a larger collection area for the Cherenkov light created by the gamma-ray shower, and hence, a larger number of gamma-ray detections. CTA will be the first observatory with a telescope array larger than the size of the Cherenkov light pool. For the first time, images will be recorded at the optimum distance from the vertical propagation axis of the gamma-ray shower, from 70 to 150 metres, a distance at which the intensity of Cherenkov light is large and fluctuations are small. Observing the shower axis from a large enough angle will allow a better reconstruction of the direction of the cascade. The angular resolution will therefore be improved, and the cosmic-ray background will be rejected more comprehensively.

However, the exact observational characteristics will depend on the array of telescopes which is finally chosen. Members of the Consortium started the site negotiations for the northern and southern hemisphere sites of CTA last April; these include Mexico, Spain and the USA for the northern and Aar in Namibia and ESO (European Southern Observatory) in Chile for the southern locations. The southern hemisphere array will consist of three types of telescopes with different mirror sizes for covering low, medium and high energy ranges, while in the northern site the two types of telescopes with larger mirrors will be constructed.

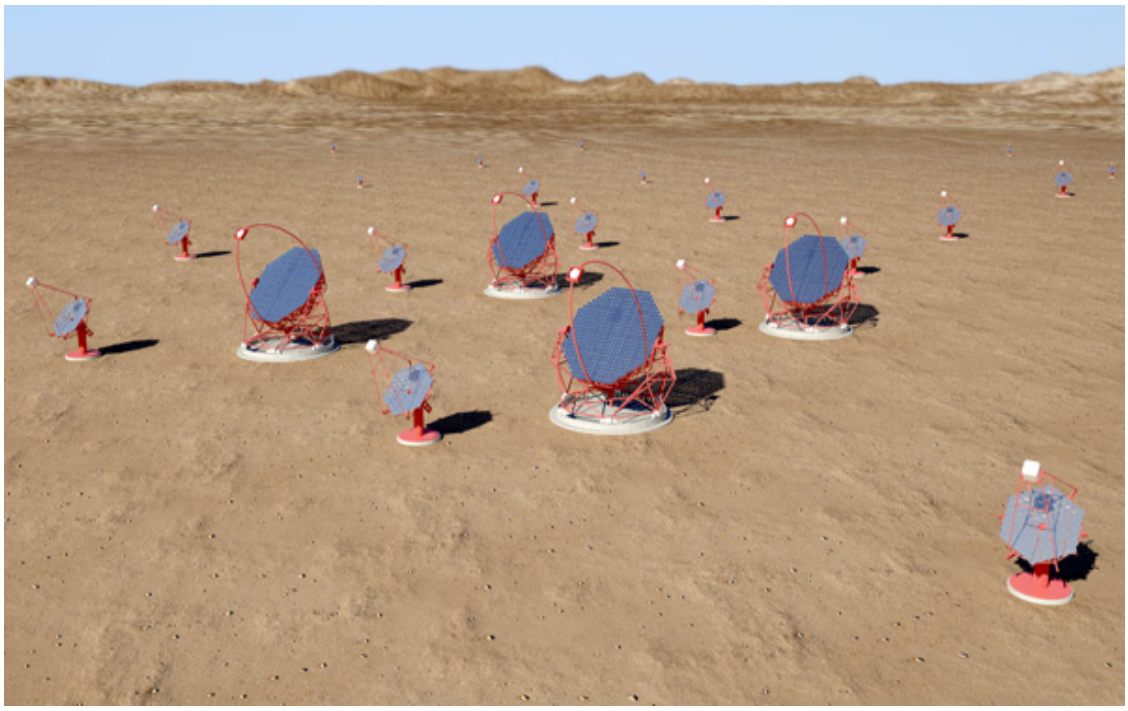

Figure 34: *Artist's impression of the Southern Observatory of CTA. Credit: G. Perez, IAC, SMM.*

Large-Size Telescopes

The Large-Size Telescopes (LSTs) will constitute the LE instruments of CTA, in the range from tens of GeV to approximately a hundred GeV. An array of 3 to 4 telescopes of diameter about 24m, as shown in Figure 31, spaced approximately 100m apart and with a field-of-view of the order of 4-5 degrees is the chosen design for the lowest energy domain of CTA.

Since at this energy range the number of events detected is high, the collection area of the array of LSTs does not have to be extremely large ($\approx$ 10,000 m^2), but the individual telescopes need large mirror areas as the Cherenkov radiation at low energies is faint. These telescopes are very expensive to build, therefore a relatively small number will be constructed.

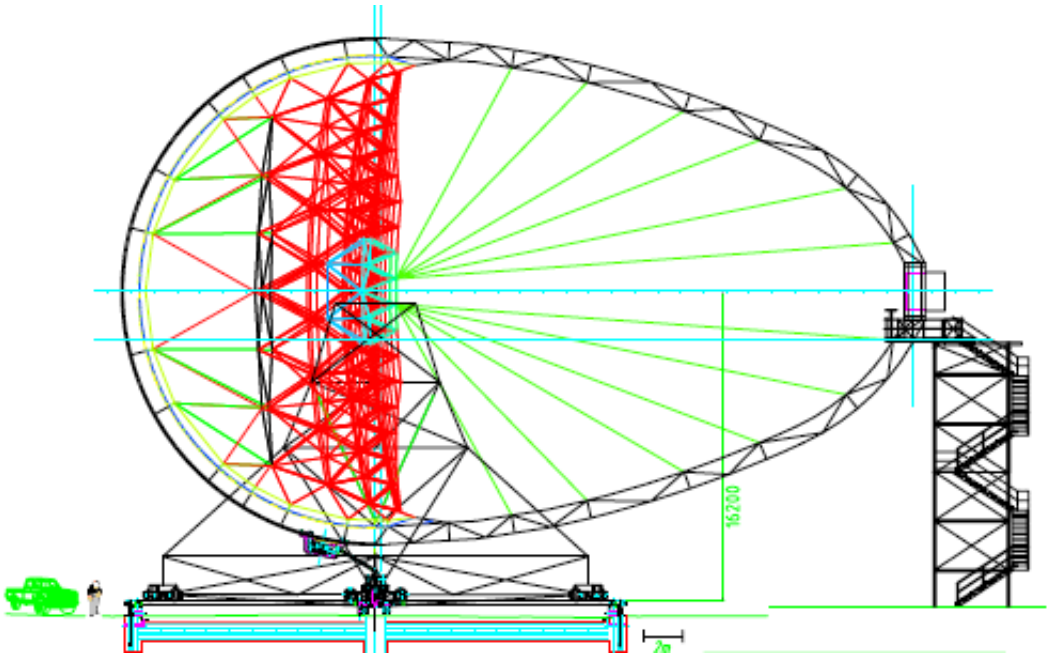

Figure 35: *Design concept for the Large Telescopes of CTA. Image credit: CTA Consortium.*

Medium-Size Telescopes

For the medium energy range (from 100 GeV to 1 TeV, the central energy range of CTA) telescopes of 10-12 metres of diameter with a field-of-view of 6-8 degrees were the chosen option, the Medium-Size Telescopes (MSTs). With this part of the array, a sensitivity of a milli-Crab will be achieved for the energy range mentioned before.

Based on the evidence provided by the current generation of IACT, which cope well in this central energy range, the best layout for the MSTs of CTA appears to be an array of around 20 telescopes with a spacing of around 100 metres.

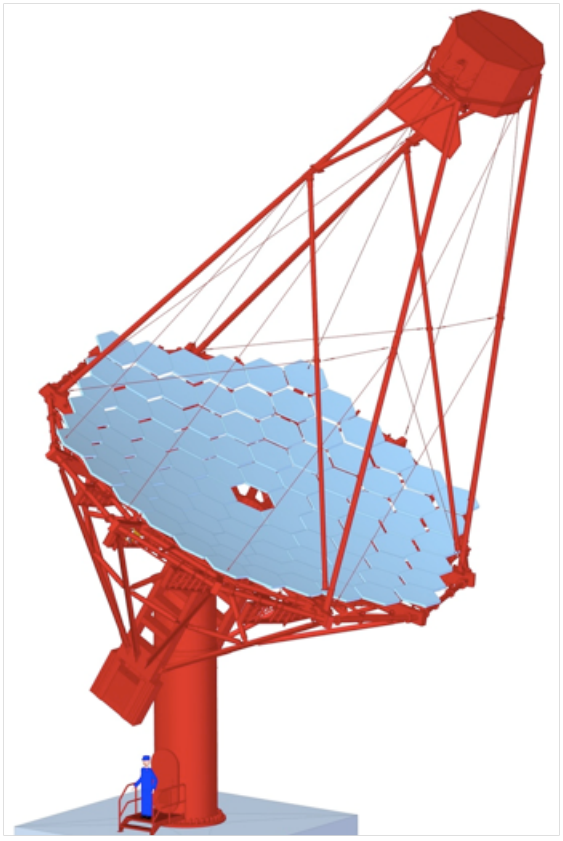

Figure 36: *Prototype for the CTA MST. Credit: CTA Consortium.*

Small-Size Telescopes

The part of CTA that will observe the sky above the threshold of 10 TeV will be made of a large number of ∼4 metre diameter telescopes with a field-of-view of approximately 10 degrees, the Small-Size Telescopes (SSTs).

As mentioned in previous sections, the main issue at the highest energy range is the small number of gamma-ray photons that reach the detector. However, the advantage of incoming VHE photons is that, being energetic, the primary gamma-ray creates more pair-production events before the minimal threshold for the interaction is reached (because the initial photon is much more energetic, more energetic electron-positron pairs will be created). Thus, more Cherenkov light photons will be created. At the same time, the light pool will be wider, so the area that SSTs have to cover will increase considerably. Showers originated by the most energetic gamma-rays can be detected beyond the 150 metre radius of a typical Cherenkov light pool.

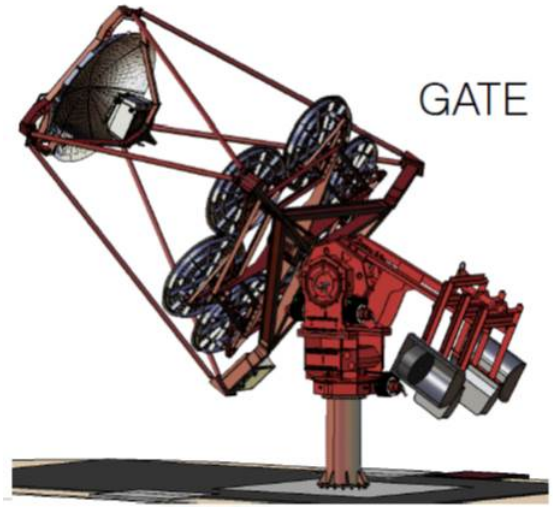

Figure 37: *An example prototype design for the SST (GCT). Credit: CTA Consortium.*

For that purpose, either a large number of small telescopes spaced according to the size of the light pool (100-200 metres) or a smaller number of slightly larger telescopes, which can detect showers to distances up to 500 metres and can consequently be located in separated subclusters of a few telescopes, can be implemented. The advantage of the subcluster option is that it would additionally provide high-quality shower detection in lower energies when the telescopes are triggered near the subcluster.

The first option, i.e. many small telescopes spaced according to the size of the light pool, corresponds to telescopes of the Davies-Cotton (DC) design, which implements a single spherical reflector segmented into individual mirrors. Ground-based gamma-ray

telescopes built so far are D-C designs. On the other hand, the option of slightly larger telescopes corresponds to Schwarzschild-Couder (S-C) double-mirror telescope designs.

S-C designs provide better point spread functions, which results in more expensive telescopes than those built following D-C designs. A major drawback of D-C designs, though, is the rapidly increasing effect of optical aberrations with the off-axis angle, which leads to narrower fields of view. Wide field of views are obtained with S-C telescopes, and permit the image capture of air showers at large distance from the telescopes. This allows larger spacing between SST telescopes, and hence one obtains increased effective areas for the same number of telescopes. For a prototype of S-C design based SST telescope for CTA, see Laporte et al. (2012).

Monte Carlo simulations for CTA

The evaluation of the expected performance of the different telescope designs and of sub-arrays of equal telescopes as well as the combined performance of the whole CTA instruments planned for the southern and northern hemispheres, is performed by the Monte-Carlo simulation method (Bernlöhr et al., 2013).

The simulations for an instrument like CTA require vast computing resources, specially for simulating enough background events, due to the excellent gamma-hadron discrimination and angular resolution of the instrument. Apart from initial simulation sets for demonstrating that the expected performance of CTA is not unreasonable, and small-scale simulations for optimization of the individual telescope types, the main effort is put into two large-scale simulation sets.

The first one, known as *Production Run 1 (PROD1)*, was based on initial and conservative assumptions of telescope parameters. It was carried out for hypothetical sites at altitudes of 2000 m and 3700 m, with source zenith angles of 20° and 50°. Some of these simulations were set up to correspond to an elevated night sky background, corresponding to partial moon light. In all of these PROD1 simulations a total of 275 telescopes was simulated, including five different types of telescopes. The performance parameters as evaluated for many different subsets, each matching a given cost envelope, were subjected to many different astrophysical test cases. These tests narrowed down the configurations or layouts with overall best performance to a class of intermediate layouts. See Bernlöhr et al. (2012), Bernlöhr et al. (2013) and Maier 2011 for further information about the overall PROD1 layout, the assumed telescope types and further details.

The PROD1 round of simulations demonstrated that the initial expectations on the CTA performance were quite realistic, except perhaps at the lowest energies where gamma-leptonic selection capabilities are limited by shower fluctuations, since electron

based air showers are difficult to distinguish from gamma-ray showers as they have similar Cherenkov footprints. Therefore, possible systematic errors in the subtraction of remaining backgrounds have to be taken into account.

The second simulation set, PROD2, takes PROD1 simulation results into consideration in the layout of the positions of the 229 telescopes of 7 different types (2 types of MST, 4 types of SST). The PROD2 simulations are currently being carried out for three different candidate sites at altitudes between 1600 and 3600 m, and assumed telescope parameters incorporate current designs (optics, camera, photo sensors, trigger, readout, etc.)

CTA sensitivity curves

As mentioned in the previous section, a wide variety of simulations has been performed to try to predict the best performance of CTA. The sensitivity of a certain CTA telescope array configuration can also be simulated via these Monte Carlo simulations (Bernlöhr et al. 2012). First, a very large number of both gamma-ray and CR induced air showers is simulated using the COSIKA code. Shower simulations span over a large range of energies and few zenith angles, and impact points are considered to scatter over a large area on the ground.

Once the showers have been simulated, the response that a given CTA array would have towards these showers is simulated, via the **sim_telarray** code. This code takes the incoming Cherenkov photons that accompany the showers and simulates the ray-tracing through the telescopes, as well as the signal processing.

Next, a reconstruction method is applied to the simulated shower images. The reconstruction leads to a certain number of reconstructed gamma-ray showers per energy bin. The background level is constituted by the CR showers that survive the gamma-hadron selection threshold.

The excess of gamma-rays over the background level can be calculated for each energy bin. A minimum 3 sigma per bin, with at least 10 excess events and an excess that is larger than 3% of the background is required. This way, one can calculate the minimum detectable energy per bin, and hence, the sensitivity curve.

For the long-term analysis of the sources performed in this work, we have considered four different analysis methods which lead to four different sensitivity curves, named after the institutes and laboratories who proposed them. We consider the baseline or KB (Konrad Bernlöhr from the Max-Planck-Institut fur Kernphysik) analysis, accepted as the basic analysis procedure for CTA simulations, and three parallel analysis techniques applied to the CTA MC simulations in order to improve the sensitivity of the

arrays, i.e. the PARIS analysis, the DESY (Deutsches Elektronen-Synchrotron) analysis and the IFAE (Institut de Física d'Altes Energies) analysis. All four analyses have been considered for an array layout E from PROD1 simulations with an exposure of 50 hours. On the other hand, for flare event analysis, we considered a PROD2 sensitivity curve for the analysis proposed by DESY for an array layout A (the most recent one in the CTA database), as well as the previously mentioned PROD1 DESY curve for the array E, so as to compare the currently developing simulations with past (and published) simulations. See Figures 38 and 39 for considered PROD1 and PROD2 telescope layouts.

The baseline analysis method, hereafter KB, uses Hillas parameters (Hillas, 1985) for stereoscopic reconstruction of IACT data. Given that Hillas parameters are highly sensible to Night Sky Background (NSB) noise, image cleaning is applied first, usually following a two-level procedure (Daum et al., 1997). The tail-cut[13] levels of the image cleaning procedure have to be adapted to NSB levels, if one wants to include significant Cherenkov light signals well above the NSB noise level. Typical high (low) tail-cut levels are 10.0 (5.0) photo-electrons times the square root of the per-pixel NSB rate in units of photo-electrons per 10 ns.

The main differences between the KB analysis and the parallel analysis techniques are the threshold applied for image cleaning and the method used for shower image reconstruction. These differences lead to slightly varying sensitivity curves, as can be appreciated in Figure 40. In this work, these four different sensitivity curves are used as a threshold to determine whether a source will be observed if a certain analysis is implemented.

For instance, both IFAE and PARIS analyses use similar image cleaning to KB analysis. However, while the tail-cuts are the same for KB and PARIS, IFAE has somewhat looser criteria for inclusion of a pixel in an image (3.0 and 6.0 photo-electrons). On the other hand, IFAE uses Hillas parametrization for shower reconstruction, while PARIS analysis implements a 3D model reconstruction (Lemoine Goumard et al., 2006) used along with a Toolkit for Multi-Variate Analysis (TMVA) background rejection, which leads to an improved sensitivity at low energies, as demonstrated for HESS (Becherini et al., 2011) and adapted to CTA (Becherini et al., 2012). Note that DESY and IFAE analyses follow similar procedures, see Maier 2011 for further details on DESY analysis.

All the sensitivities are plotted in Figure 40, and as can be seen, are not very different from one another in average, but when compared to the spectra of our FSRQs, there is a significant difference between some of them. See Section 6 in Chapter 5 for the results of long-term analysis, and Section 3 in Chapter 6 for flare events.

[13] Tail-cut: standard image pre-processing procedure discarding the pixels with signals below some level.

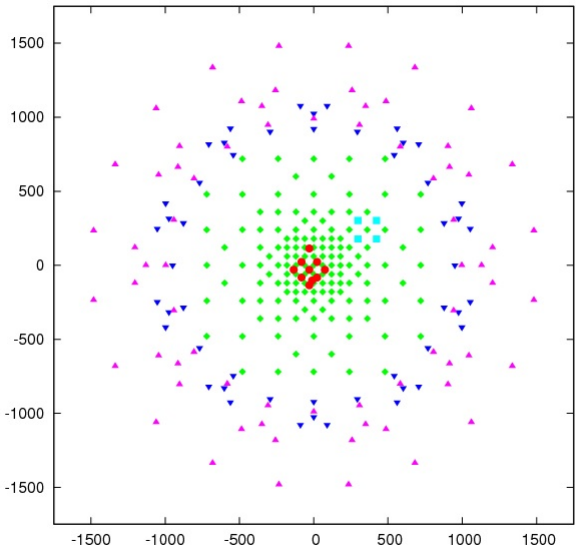

Figure 38: *Telescope layout for array layout E of PROD1 CTA configuration. Red points are 23m telescopes, black points 12m telescopes, pink points 10m telescopes, green points 6.7m telescopes and blue points 12m telescopes with 10 degrees field-of-view. Credit: Konrad Berlöhr.*

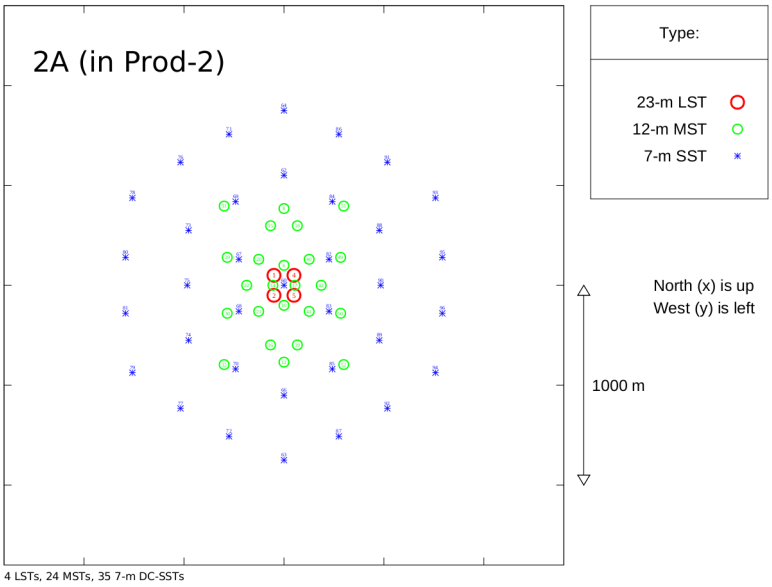

Figure 39: *Telescope layout for array layout A of PROD2 CTA configuration. Credit: Konrad Berlöhr.*

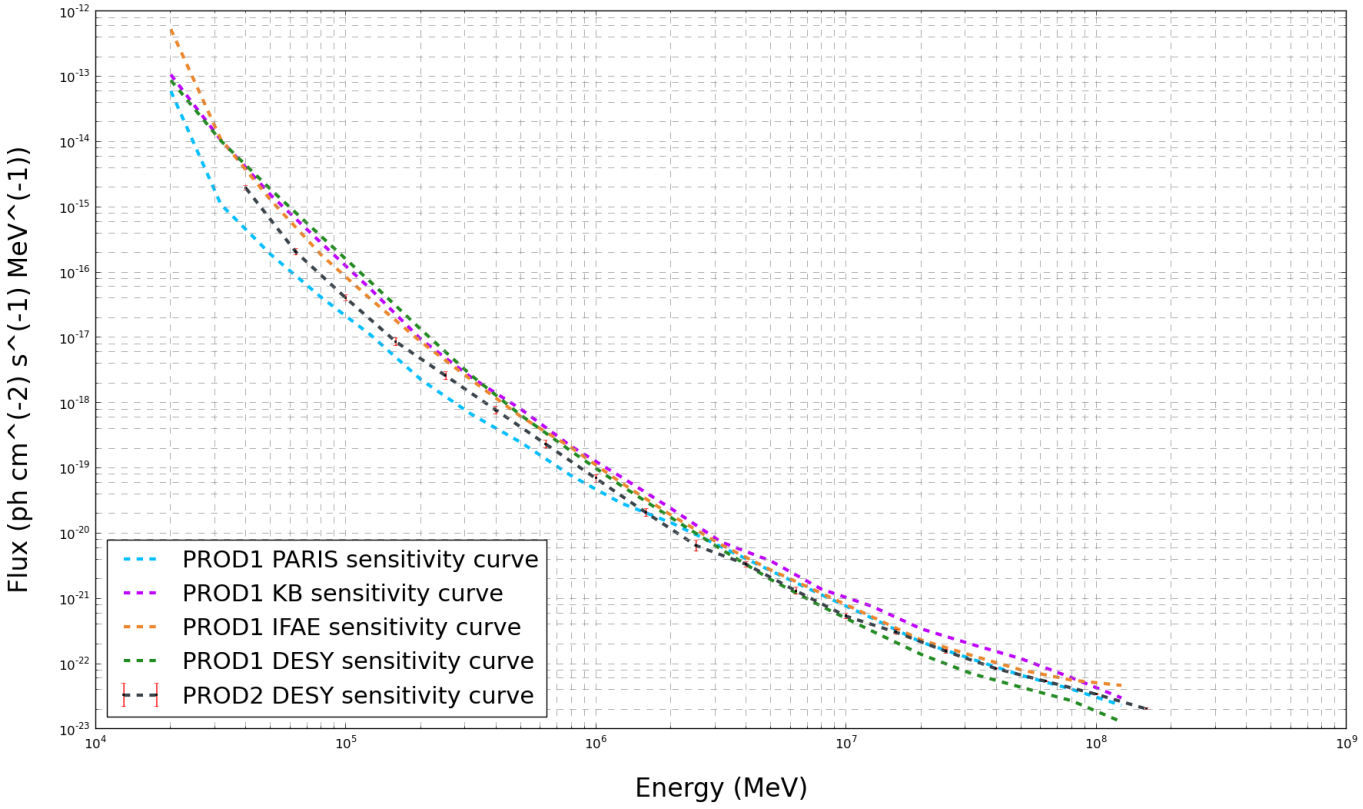

Figure 40: *Plot of sensitivity curves considered for long-term analysis (PROD1) and for flare event analysis (PROD2).*

5. ANALYSIS OF THE LONG-TERM EMISSION FROM THE SELECTED FSRQs

In this chapter, the analysis of the long-term emission for the selected FSRQs is presented. First, the sample of sources and the criteria for selecting them are provided, followed by the procedure for the acquisition of *Fermi*-LAT data. Next, background and source model files, and model creation are introduced. Finally, the procedure for the 5-year period analysis performed is explained.

1. Source sample

A sample of nine FSRQs was chosen for this work. The main selection criterion was the brightness of the sources, i.e. the brightest nine FSRQs according to the 2-year *Fermi* catalogue (Nolan et al., 2012) were chosen. A Galactic latitude threshold greater than $b > \pm 10^{\circ}$ was also selected, because we wanted to consider sources located away from the Galactic plane, since it is very bright at gamma-ray energies, as can be seen in Figure 29. The sample of the FSRQs chosen is shown in Table 2.

2. Data acquisition and filtering criteria

For the data acquisition and analysis, the FSSC team [69] publicly distributes specific science analysis tools, the *Fermi Tools*, which can be used to perform various types of data analysis. In this work, the latest version of them has been implemented, **v9r33p0**, released Jun 03, 2014.

Table 3: List of selected FSRQs and their characteristics

SOURCE	FLUX (1-100 GeV)	REDSHIFT	SPECTRAL INDEX	MONITORED?	TEVCAT?
3C454.3	$(96.5\pm1)\times10^{-9}$	0.859	2.226 ± 0.008	✓	×
PKS1510-089	$(406\pm7.2)\times10^{-10}$	0.36	2.288 ± 0.014	×	✓
PKS1502+106	$(401\pm7.3)\times10^{-10}$	1.83928	2.147 ± 0.017	✓	×
4C+21.35	$(354\pm6.4)\times10^{-10}$	0.433507	2.122 ± 0.015	×	✓
3C279	$(256\pm5.7)\times10^{-10}$	0.536	2.221 ± 0.019	✓	✓
PKS0454-234	$(227\pm5.4)\times10^{-10}$	1.003	2.033 ± 0.021	✓	×
PKS0727-11	$(220\pm5.8)\times10^{-10}$	1.591	2.108 ± 0.024	✓	×
B21520+31	$(176\pm4.5)\times10^{-10}$	1.484	2.248 ± 0.021	✓	×
3C273	$(151\pm4.5)\times10^{-10}$	0.158	2.452 ± 0.022	✓	×

List of the 9 FSRQs analyzed (column 1), their flux (column 2), redshift (column 3) and spectral index (column 4), whether a source has been monitored by the FSSC (column 5) and if a source has been detected in the TeV range (last column). Data was taken from the ASI Science Data Center.

The photon data files can also be obtained from the FSSC website, along with the *spacecraft file* that accounts for the performance of the telescope during a certain period of time. For the present analysis, the observation period considered is from 2008-08-04 to 2014-01-15 (from 239557414 to 411464064 in *Mission Elapsed Time*, MET[14], and from 54682 to 56672 in *Modified Julian Date*, MJD[15]) for the whole *Fermi* energy range (i.e. 100 MeV to 300 GeV). The *search radius* or *radius of interest* (ROI) was 15° degrees wide from the source. The point spread function of the LAT is larger at high energies, therefore a larger ROI has to be implemented.

To avoid contamination from Earth limb gamma-rays originating from cosmic rays coming into the atmosphere, a *zenith angle cut* $< 100°$ was applied. An event class of 2 ($evclass = 2$ option) was chosen in the *Fermi* tool **gtselect**, the option recommended for point source analysis. This ensures that the events selected have a high probability of being photons. Other event class options available for event data filtering are event class of 3 ($evclass = 3$) for *clean* events, and event class of 4 ($evclass = 4$) for *ultraclean* events.

Further filtering criteria are applied via the **gtmktime** tool, which uses the spacecraft(SC) files to select the good time intervals (GTI). One can select GTIs by using a logical filter for any of the quantities in the SC file. For our analysis, we have applied the the recommended quality filter cuts DATA_QUAL= 1, LAT_CONFIG= 1, and ABS(ROCK_ANGLE)<52, which are the cuts recommended for *Fermi* analysis in the FSSC.

[14]MET: True elapsed seconds since January 1, 1994, corresponding to the start of the RXTE mission
[15]Equals JD-2400000.5, where JD is the number of days since Greenwich mean noon on January 1, 4713 BC

- DATA_QUAL: quality flag set by the LAT instrument team (1 = ok, 2 = waiting review, 3 = good with bad parts, 0 = bad).

- LAT_CONFIG: instrument configuration (0 = not recommended for analysis, 1 = science configuration).

- ROCK_ANGLE: can be used to eliminate pointed observations from the dataset, and also to confirm the stability of the rocking of the detector.

Table 4: Data acquisition and analysis criteria

Fermi tools version	v9r33p0
Observation period in MET	239557414 to 411464064
Energy range	100 MeV - 300 GeV
ROI	15°
Zenith angle	<100°
Event class	=2
Data quality	=1
LAT configuration	=1
Rock angle	<52

List of analysis criteria followed in the analysis of the sources for the 5-year dataset.

3. Galactic, extragalactic and point source models

The FSSC not only provides the data files and the analysis tools - a spatial and spectral model of the Galactic diffuse gamma-ray emission and a spectral template for isotropic extragalactic gamma-ray emission are also provided. The isotropic template includes contamination of the gamma-rays from residual charged cosmic rays.

For the latest tool release, the diffuse background model is *gll_iem_v05_rev1.fit*, while the recommended isotropic template is *iso_source05.txt*. The isotropic spectrum is valid only for the P7REP_SOURCE_V15 response functions, which have been implemented in this work. Moreover, information concerning the gamma-ray sources discovered by *Fermi* is taken from the file *gal_2yearp7v6_v0.fits* that corresponds to the 2-year *Fermi* catalog.

Creating a model file is necessary, since the **gtlike** routine for a likelihood analysis compares the significance of the data with and without a model. The model file contains sources published in the 2 year *Fermi* LAT catalogue regarding the spectral shapes and positions of the sources in the *Fermi* data files. Throughout this work, model files are created using the user contributed tool **make2FGLxml.py** available from the FSSC website.

It must be said that the **make2FGLxml.py** script automatically adds 5 degrees to your ROI to account for sources that lie just outside your data region, but with photons that could be in your data. In addition, it frees all the spectral normalisation parameters for sources within your ROI, and fixes them for the others.

The created xml file uses the spectral model from the 2-year *Fermi* catalog for each source, but a closer analysis might point out that another spectral model could be more suitable for describing the source. Therefore, in this work the model files created with **make2FGLxml.py** for each of our FSRQs are changed, in order to describe the corresponding FSRQ with the 4 different spectral models that follow:

- Broken Power Law,

$$\frac{dN}{dE} = N_0 \begin{cases} (E/E_b)^{\gamma_1} & \text{if } E < E_b \\ (E/E_b)^{\gamma_2} & \text{otherwise} \end{cases} \tag{20}$$

- Power Law,

$$\frac{dN}{dE} = N_0 \, (\frac{E}{E_0})^{\gamma} \tag{21}$$

- Logarithmic Parabola,

$$\frac{dN}{dE} = N_0 \, (\frac{E}{E_b})^{-(\alpha+\beta \mathrm{Log}(E/E_b))} \tag{22}$$

- Exponential Cut-Off,

$$\frac{dN}{dE} = N_0 \begin{cases} (E/E_0)^{\gamma} & \text{if } E < E_b \\ (E/E_0)^{\gamma} \exp[-((E-E_b)/p_1 + p_2 \mathrm{Log}(E/E_b) + p_3 \mathrm{Log}^2(E/E_b))] & \text{otherwise} \end{cases} \tag{23}$$

The parameters that define the different spectral models can be changed, frozen or set free by changing some little details in the model file. This is interesting when performing

likelihood analysis of large sets of data with many sources and parameters to fit, as will be explained in the next Section.

When data from a source is fitted with a certain spectral model, the significance of the likelihood fit is given by the *Test Statistic* (TS) value of the source, defined as

$$TS = -2\ \frac{\mathcal{L}_{max,0}}{\mathcal{L}_{max,1}} \tag{24}$$

where $\mathcal{L}_{max,0}$ is the maximum likelihood value for a model without the source, and $\mathcal{L}_{max,1}$ the maximum likelihood values for a model with the additional source at a specified location. The square root of the TS value is approximately the detection significance for a source.

Accordingly, sources with low TS values are not very significant to the analysis, and therefore can be removed from model files. On the other hand, sources with high TS values, and hence significance, might have not been properly modelled in our file, because they are not present in the 2-year *Fermi* catalog[16]. If an extra source is observed in the residual map, it has to be inserted into the model file (see Section 5.4 for more information about model maps and residual maps).

4. Analysis of the 5-years of *Fermi* data from the chosen FSRQs

After gathering the data files corresponding to the observational period of interest, filtering them according to the afore mentioned criteria (Table 3), and making the corresponding model files, a *likelihood* analysis was performed for each FSRQ.

As mentioned in Section 5.3, 4 different spectral models were considered for each FSRQ. So the first thing was to decide which was the best fit model for the 5-year data set.

For this purpose, a *binned likelihood* analysis, more appropriate than an *unbinned* due to the large data sets we needed to analyse, was performed for each of the different model files. Unbinned analysis is preferable short time periods with few events (such as flare events), while binned analysis is better for long timescales or high-density data which can cause errors in the unbinned analysis. The likelihood output value of the binned **gtlike** routine is paramount to determine the best fit spectral model, via the

[16] The 2-year *Fermi* catalogue only consists of the sources detected in the first two years of the mission. Unsurprisingly, many gamma-rays have been detected since this catalogue was published. Lacking a newer source catalog, they have to be manually inserted and modelled by the astronomer

Akaike Information Criterion, AIC (Akaike, 1974).

$$AIC = 2\mathrm{k} - 2\mathrm{Ln}(\mathrm{Likelihood}) \tag{25}$$

where k is the number of free parameters of the model and *Likelihood* is the maximized value of the likelihood function of the model.

According to the AIC, for a number of different models, the best fit model is the one with the minimum AIC value, and hence the model that minimizes the information loss due to the choice of a certain type of model (see Table 4 for the different AIC values obtained).

Table 5: List of AIC values for each spectral model

SOURCE	LogParabola	PowerLaw	BrokenPowerLaw	ExpCutoff
3C454.3	**-771018.8642**	-769399.548	-770859.091	-770817.0558
PKS1510-089	-559441.9412	-559172.1972	**-559446.326**	-559312.2876
PKS1502+106	**-71535.76694**	-71254.34816	-71494.80666	-71507.19842
4C+21.35	**-34039.38574**	-33920.38546	-34022.75782	-33904.48504
3C279	**-216748.175**	-216621.167	-216724.5698	-216719.7094
PKS0454-234	**20494.62238**	20771.55144	20516.56784	20562.91
PKS0727-11	**-2076237.568**	-2076176.686	-2076230.144	-2076221.76
B21520+31	**-12322.178886**	-12195.73324	-12293.461742	-12307.031404
3C273	**-119802.64434**	-119635.69424	-119794.36658	-119754.88018

AIC values for each spectral model considered for the 9 FSRQs of interest, obtained by applying Eq. 16. The minimum AIC value for each source appears in bold print.

The quantity

$$\exp((AIC_{min} - AIC_i)/2) \tag{26}$$

is known as the *relative likelihood* of model i, and denotes how probable model i is compared to the model with the minimum AIC value ($\mathrm{AIC_{min}}$) to minimize the information loss. See Table 5 for the best fit model for each of the FSRQs.

After determining the best fit model, the point sources with low TS values (TS$<$ 1) were taken out from the fitted output model from the **gtlike** routine corresponding to that best fit model, as mentioned in Section 5.3.

On the other hand, as mentioned in Section 5.3, some significant sources (sources with high TS values) might have been omitted in our original model file, due to the fact that for the creation of such a model file the 2 year *Fermi* LAT Catalogue is used, and since this catalogue was published, more gamma-ray sources have been discovered by *Fermi* LAT that are not yet accounted for in a new catalogue. Counts maps (also known as sky maps), model maps, and residuals maps are produced in search for a potential excess.

Table 6: List of selected FSRQs, corresponding best fit model and characteristics

SOURCE	FLUX	SPEC IND 1	SPEC IND 2	BEST FIT MODEL
3C454.3	$(1.995 \pm 0.001)\times10^{-6}$	2.2137 ± 0.0007	0.1065 ± 0.0004	LogParabola
PKS1510-089	$(9.090 \pm 0.015)\times10^{-7}$	-2.2160 ± 0.0010	-2.5472 ± 0.0017	BrokenPowerLaw
PKS1502+106	$(3.0081 \pm 0.0007)\times10^{-7}$	2.2020 ± 0.0001	0.1155 ± 0.0009	LogParabola
4C+21.35	$(4.512 \pm 0.026)\times10^{-7}$	2.2172 ± 0.0054	0.0568 ± 0.0025	LogParabola
3C279	$(4.420 \pm 0.002)\times10^{-7}$	2.2411 ± 0.0005	0.0671 ± 0.0002	LogParabola
PKS0454-234	$(2.954 \pm 0.014)\times10^{-7}$	2.0171 ± 0.0040	0.0984 ± 0.0018	LogParabola
PKS0727-11	$(2.543 \pm 0.001)\times10^{-7}$	2.1667 ± 0.0005	0.0651 ± 0.0002	LogParabola
B21520+31	$(3.457 \pm 0.032)\times10^{-7}$	2.2403 ± 0.0101	0.0733 ± 0.0049	LogParabola
3C273	$(3.600 \pm 0.011)\times10^{-7}$	2.4330 ± 0.0034	0.1494 ± 0.0020	LogParabola

9 FSRQs analysed for 5-year long-term analysis (column 1), their 100 MeV-300GeV flux obtained from the binned likelihood analysis of the 5 years of data in units of photons/cm^2/s (column 2), the first (column 3) and second (column 4) spectral indexes from the likelihood analysis, and the best fit spectral model obtained for the 5-year period analysis (last column). According to Eq. 13, for sources best modelled as LogParabolas the first spectral index is α whereas the second is β. On the other hand, for sources best fit with a BrokenPowerLaw, the first spectral index corresponds to γ_1 and the second to γ_2 in Eq. 11.

Sky maps are obtained using the **gtbin** tool, and illustrate what our data (filtered according to the chosen criteria) look like. Model counts maps, on the other hand, illustrate what the data should look like according to the model file that has been used for fitting the data. Model counts are obtained via the **gtmodel** *Fermi* tool to the model file used for the likelihood analysis. The subtraction of the counts maps and the model counts maps, i.e. a residuals map, shows whether our data have been properly modelled, since any excess in flux in the residuals maps means gamma-ray sources not taken into account in the model map. Residuals can be obtained with the **farith** routine from **heasoft** tools. In our case, we have obtained residuals maps that give information in terms of percentages, by first subtracting the counts maps and the model counts map, and then dividing the result with the model counts map: (countsmap − modelcountsmap)/(modelcountsmap). Figures 41-49 show the counts maps, model counts maps and residuals maps for all the 9 FSRQs.

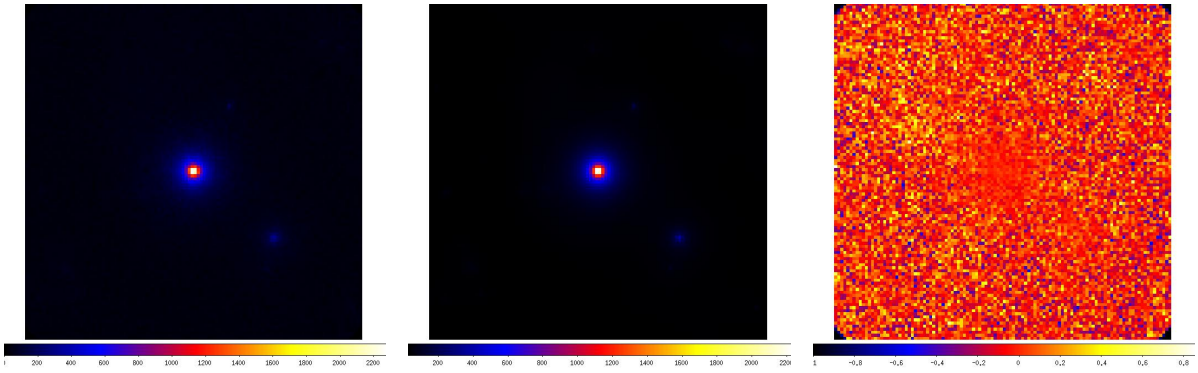

Figure 41: *Source 3C454.3. LEFT - 100 MeV-300 GeV map for the whole 5 year period. Counts per pixel are shown on the color bar. The image scale is 0.2° per pixel, and the image covers 22° ×22°. CENTER - Model map obtained with the* ***gtmodel*** *Fermi tool for the whole 5 year period, using the best fit model which for 3C454.3 is a LogParabola. Counts per pixel are shown on the color bar. The image scale is 0.2° per pixel, and the image covers 22° ×22°. RIGHT - Residuals map of the 100 MeV-300 GeV events in units of percentage. The residuals map is produced by (sky map - model map)/(model map). The colour scales for both the sky map and the model map are in units of gamma-ray counts, whereas the residuals maps are in units of percentage. No evidence is visible for new gamma-ray sources.*

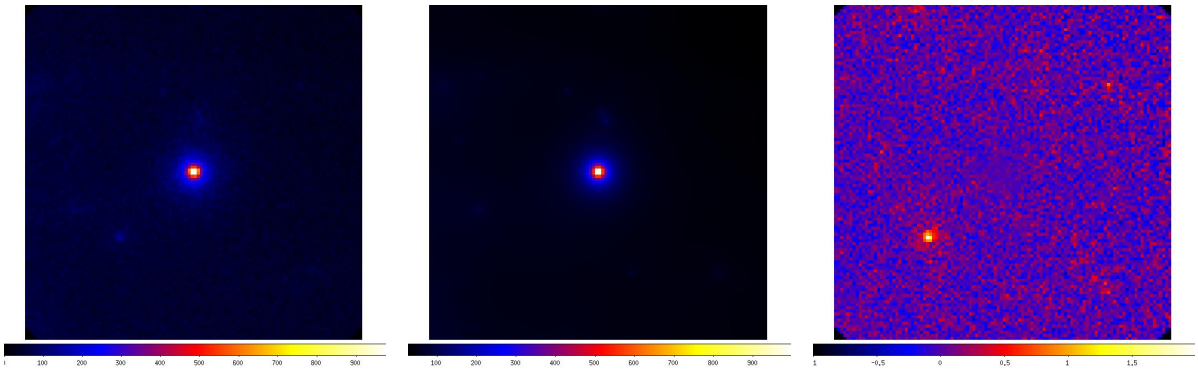

Figure 42: *Source PKS1510-089. LEFT - 100 MeV-300 GeV map for the whole 5 year period. Counts per pixel are shown on the color bar. The image scale is 0.2° per pixel, and the image covers 22° ×22°. CENTER - Model map obtained with the* ***gtmodel*** *Fermi tool for the whole 5 year period, using the best fit model which for PKS1510-089 is a BrokenPowerLaw. Counts per pixel are shown on the color bar. The image scale is 0.2° per pixel, and the image covers 22° ×22°. RIGHT - Residuals map of the 100 MeV-300 GeV events in units of percentage. The residuals map is produced by (sky map - model map)/(model map). The colour scales for both the sky map and the model map are in units of gamma-ray counts, whereas the residuals maps are in units of percentage. A point source not taken into account by the best fit model is evident in the residuals map.*

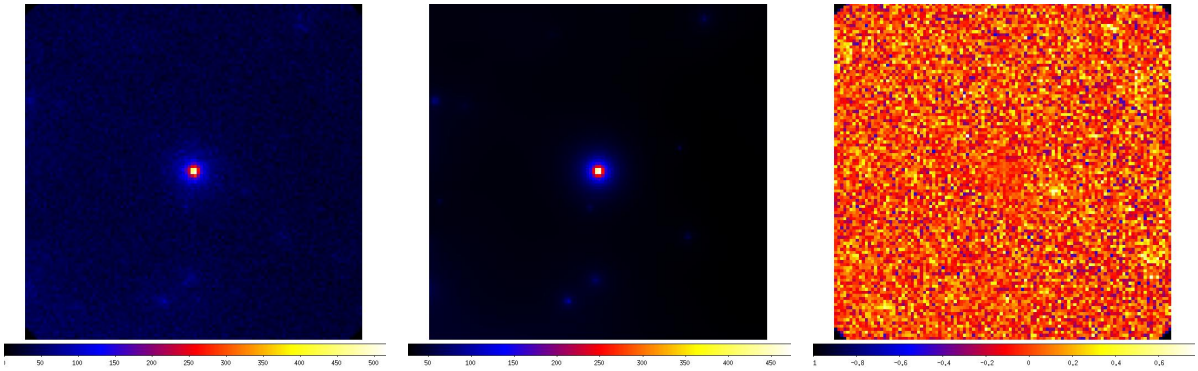

Figure 43: *Source PKS1502+106. LEFT - 100 MeV-300 GeV map for the whole 5 year period. Counts per pixel are shown on the color bar. The image scale is 0.2° per pixel, and the image covers 22° ×22°. CENTER - Model map obtained with the* ***gtmodel*** *Fermi tool for the whole 5 year period, using the best fit model which for PKS1502+106 is a LogParabola. Counts per pixel are shown on the color bar. The image scale is 0.2° per pixel, and the image covers 22° ×22°. RIGHT - Residuals map of the 100 MeV-300 GeV events in units of percentage. The residuals map is produced by (sky map - model map)/(model map). The colour scales for both the sky map and the model map are in units of gamma-ray counts, whereas the residuals maps are in units of percentage. No evidence is visible for new gamma-ray sources.*

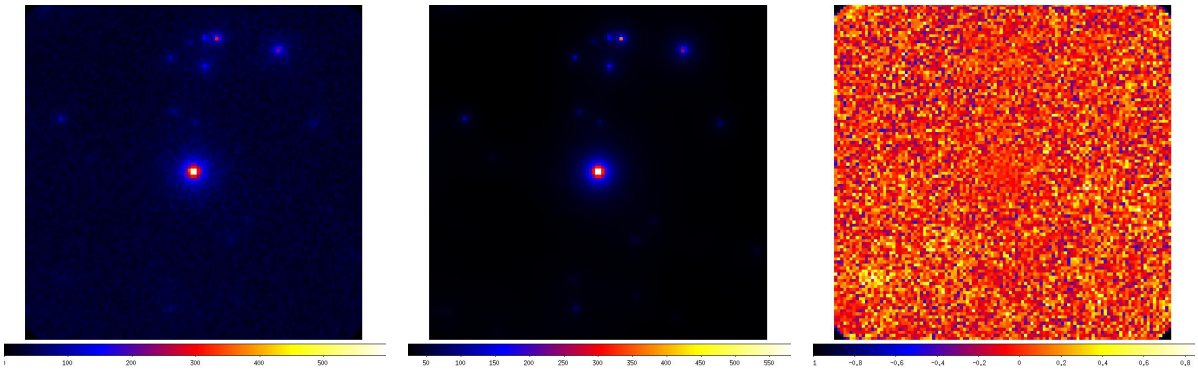

Figure 44: *Source 4C+21.35. LEFT - 100 MeV-300 GeV map for the whole 5 year period. Counts per pixel are shown on the color bar. The image scale is 0.2° per pixel, and the image covers 22° ×22°. CENTER - Model map obtained with the* ***gtmodel*** *Fermi tool for the whole 5 year period, using the best fit model which for 4C+21.35 is a LogParabola. Counts per pixel are shown on the color bar. The image scale is 0.2° per pixel, and the image covers 22° ×22°. RIGHT - Residuals map of the 100 MeV-300 GeV events in units of percentage. The residuals map is produced by (sky map - model map)/(model map). The colour scales for both the sky map and the model map are in units of gamma-ray counts, whereas the residuals maps are in units of percentage. No evidence is visible for new gamma-ray sources.*

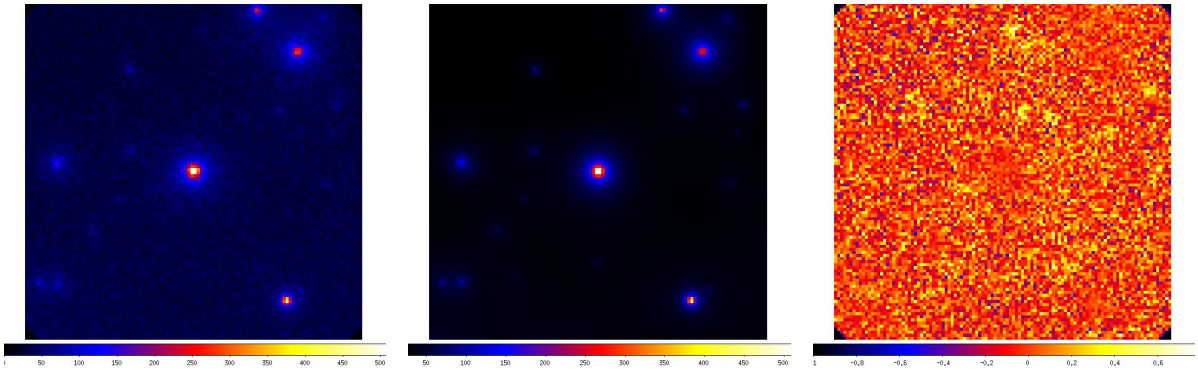

Figure 45: *Source 3C279. LEFT - 100 MeV-300 GeV map for the whole 5 year period. Counts per pixel are shown on the color bar. The image scale is 0.2° per pixel, and the image covers 22° ×22°. CENTER - Model map obtained with the* ***gtmodel*** *Fermi tool for the whole 5 year period, using the best fit model which for 3C2793 is a LogParabola. Counts per pixel are shown on the color bar. The image scale is 0.2° per pixel, and the image covers 22° ×22°. RIGHT - Residuals map of the 100 MeV-300 GeV events in units of percentage. The residuals map is produced by (sky map - model map)/(model map). The colour scales for both the sky map and the model map are in units of gamma-ray counts, whereas the residuals maps are in units of percentage. No evidence is visible for new gamma-ray sources.*

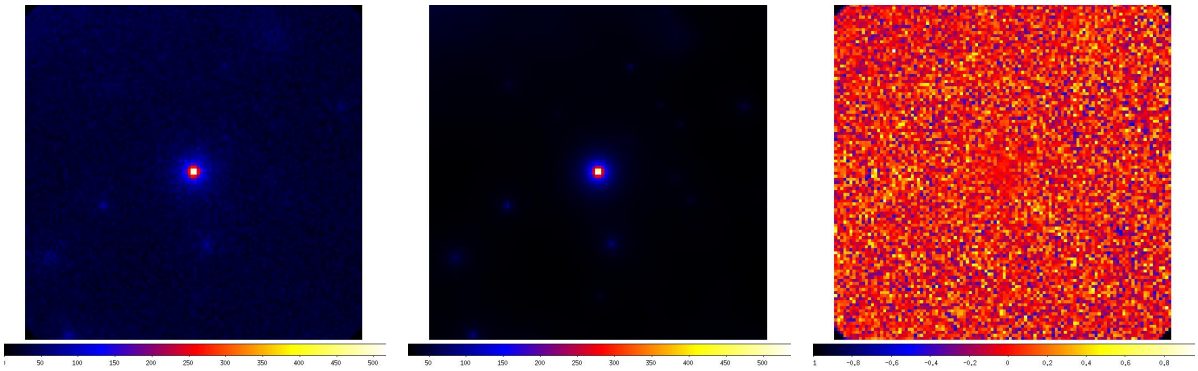

Figure 46: *Source PKS0454-234. LEFT - 100 MeV-300 GeV map for the whole 5 year period. Counts per pixel are shown on the color bar. The image scale is 0.2° per pixel, and the image covers 22° ×22°. CENTER - Model map obtained with the* ***gtmodel*** *Fermi tool for the whole 5 year period, using the best fit model which for PKS0454-234 is a LogParabola. Counts per pixel are shown on the color bar. The image scale is 0.2° per pixel, and the image covers 22° ×22°. RIGHT - Residuals map of the 100 MeV-300 GeV events in units of percentage. The residuals map is produced by (sky map - model map)/(model map). The colour scales for both the sky map and the model map are in units of gamma-ray counts, whereas the residuals maps are in units of percentage. No evidence is visible for new gamma-ray sources.*

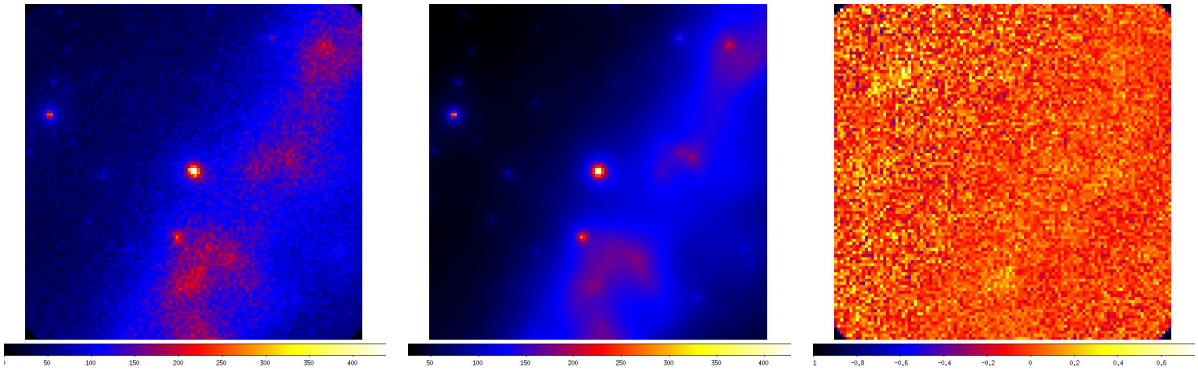

Figure 47: *Source PKS0727-11. LEFT - 100 MeV-300 GeV map for the whole 5 year period. Counts per pixel are shown on the color bar. The image scale is 0.2° per pixel, and the image covers 22° ×22°. CENTER - Model map obtained with the* ***gtmodel*** *Fermi tool for the whole 5 year period, using the best fit model which for PKS0727-11 is a LogParabola. Counts per pixel are shown on the color bar. The image scale is 0.2° per pixel, and the image covers 22° ×22°. RIGHT - Residuals map of the 100 MeV-300 GeV events in units of percentage. The residuals map is produced by (sky map - model map)/(model map). The colour scales for both the sky map and the model map are in units of gamma-ray counts, whereas the residuals maps are in units of percentage. No evidence is visible for new gamma-ray sources.*

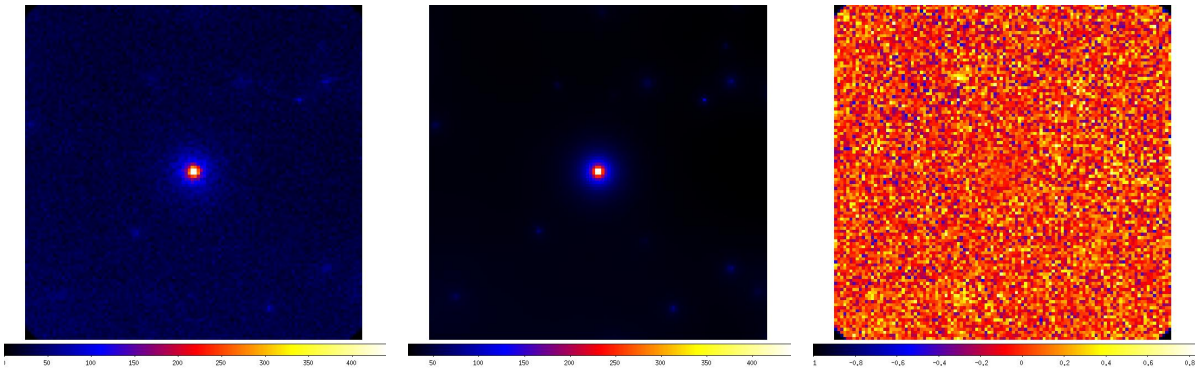

Figure 48: *Source B21520+31. LEFT - 100 MeV-300 GeV map for the whole 5 year period. Counts per pixel are shown on the color bar. The image scale is 0.2° per pixel, and the image covers 22° ×22°. CENTER - Model map obtained with the* ***gtmodel*** *Fermi tool for the whole 5 year period, using the best fit model which for B21520+31 is a LogParabola. Counts per pixel are shown on the color bar. The image scale is 0.2° per pixel, and the image covers 22° ×22°. RIGHT - Residuals map of the 100 MeV-300 GeV events in units of percentage. The residuals map is produced by (sky map - model map)/(model map). The colour scales for both the sky map and the model map are in units of gamma-ray counts, whereas the residuals maps are in units of percentage. No evidence is visible for new gamma-ray sources.*

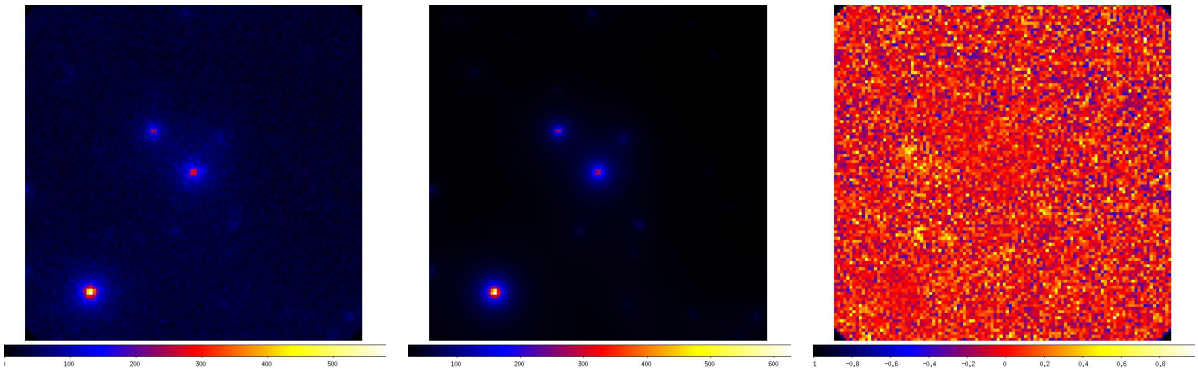

Figure 49: *Source 3C273. LEFT - 100 MeV-300 GeV map for the whole 5 year period. Counts per pixel are shown on the color bar. The image scale is 0.2° per pixel, and the image covers 22° ×22°. CENTER - Model map obtained with the* ***gtmodel*** *Fermi tool for the whole 5 year period, using the best fit model which for 3C273 is a LogParabola. Counts per pixel are shown on the color bar. The image scale is 0.2° per pixel, and the image covers 22° ×22°. RIGHT - Residuals map of the 100 MeV-300 GeV events in units of percentage. The residuals map is produced by (sky map - model map)/(model map). The colour scales for both the sky map and the model map are in units of gamma-ray counts, whereas the residuals maps are in units of percentage. No evidence is visible for new gamma-ray sources.*

If the data have been properly modelled, the residuals would show no point-like sources, which is the case for 8 out of 9 sources. For the remaining source, PKS1510-089, an extra point-like source was present in the residuals map, as can be seen in Figure 42. Hence, the object was introduced in the model file in form of a simple PowerLaw (for the sake of simplicity). Afterwards, the binned likelihood analysis was performed again in order to check if the object had been correctly modelled by a PowerLaw, in which case the bright point would have disappeared from the residuals, which is what actually happened (see Figure 48).

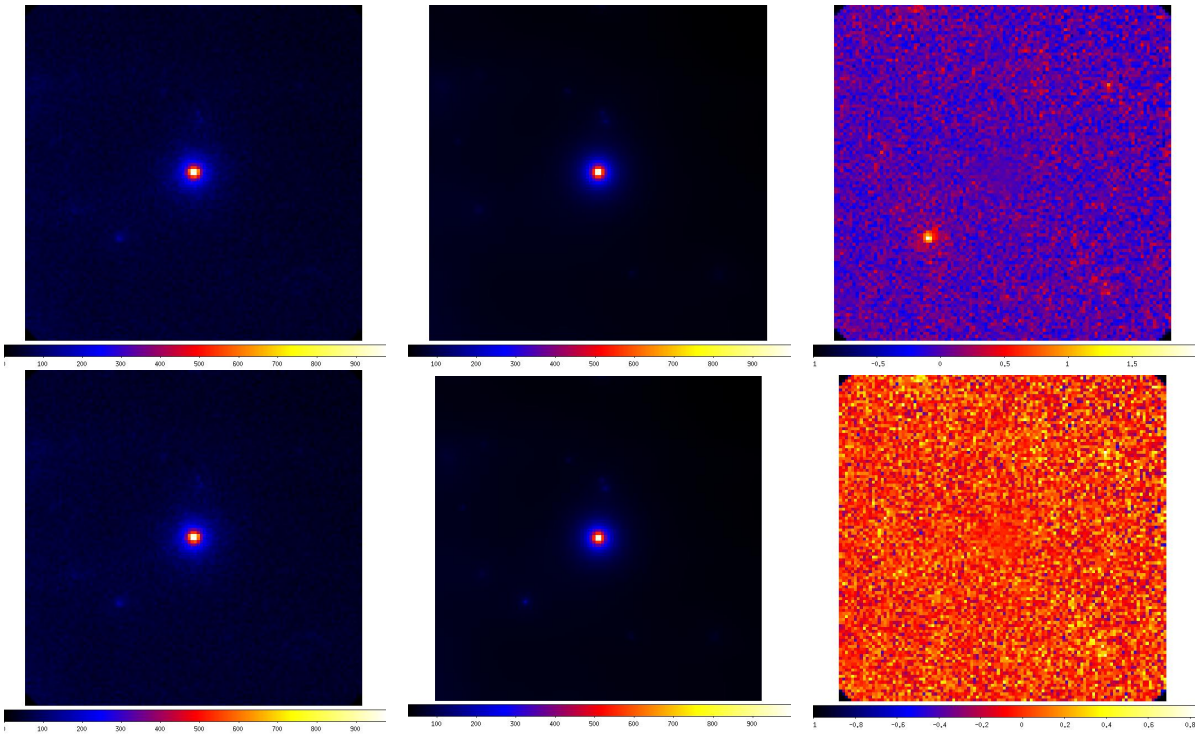

Figure 50: *Source 3C273. LEFT COLUMN - 100 MeV-300 GeV map for the whole 5 year period. Counts per pixel are shown on the color bar. The image scale is 0.2° per pixel, and the image covers 22° ×22°. CENTER COLUMN - Model map obtained with the* ***gtmodel*** *Fermi tool for the whole 5 year period, using the best fit model which for 3C273 is a LogParabola. Counts per pixel are shown on the color bar. The image scale is 0.2° per pixel, and the image covers 22° ×22°. RIGHT COLUMN - Residuals map of the 100 MeV-300 GeV events in units of percentage. The residuals map is produced by (sky map - model map)/(model map). UPPER ROW - Source PKS1510-089 modelled as a BrokenPowerLaw. LOWER ROW - Source PKS1510-089 modelled as BrokenPowerLaw with point-like source added as a PowerLaw. The colour scales for both the sky map and the model map are in units of gamma-ray counts, whereas the residuals maps are in units of percentage. No evidence is visible for new gamma-ray sources.*

The likelihood analysis also gives us an insight into the significance of the new extra sources via their TS value. It cannot be directly stated that the additional point of gamma-ray flux excess is in fact a source, but still its significance has to be taken into consideration. Therefore, a threshold of TS=16 was established: new sources with TS values above the threshold were significant enough to be considered and modelled, as happened for the extra point in the residuals of PKS1510-089 (TS= 1147.95). The extra point-like gamma-ray source turned out to be a flare event of the FSRQ TXS 1530-131, detected by *Fermi*-LAT on 2012 August 22 (Gasparrini & Cutini, 2011).

Once both the low and high TS values had been accounted for in a new model file, a binned analysis was performed again for this modified model, in order to reduce the secondary sources in the model file to a 10° radius from our main FSRQ, by freezing

all the parameters for the sources beyond this radius, and by freezing everything except for the normalization or prefactor parameter for sources within that radius. The model file consisting of sources within 10° and with the low and high TS values properly dealt with is the definitive model file to use to get the spectrum of the source.

Next, splitting the whole *Fermi* energy range into 11 smaller logarithmic energy bins[17] and using this definitive model file, a binned likelihood analysis was done for each bin for the whole 5 years. A minimum threshold of TS=25 was set for all the energy bins. For those with lower values, upper limits were calculated via a **gtlike** unbinned likelihood analysis only for the corresponding energy bin.

The flux values obtained for the energy bins were used for getting the best fit values (normalization/prefactor, break energy, *alpha* and β for LogParabolas and normalization/prefactor, break energy, γ_1 and γ_2 for BrokenPowerLaw) corresponding to the best fit spectral model according to the AIC calculation (Table 5). The best fit function was therefore obtained for the data points, and this function was then extrapolated to the CTA energy ranges by splitting this energy range into logarithmic energy bins, as done for the *Fermi* energy range. Once I had the extrapolated function for the CTA range, I corrected the extrapolated function for EBL flux absorption following Eq. 9 in Chapter 3. The EBL model and optical depth values considered can be found in Franceschini et al. 2008. The main features of the EBL model have been presented in Chapter 3.

6. Results for 5-year long-term analysis

In the first part of this section, the spectra for all the ten sources in the *Fermi*-LAT and CTA energy range, are gathered together. The fluxes have been corrected for EBL absorption for the energies in which its effect becomes important, as mentioned in the previous Section.

In order to qualitatively determine if a source is likely to be detected by CTA, both the spectra of the flux corrected for EBL absorption and the PROD1 sensitivity curves mentioned in Chapter 4 Section 5 were plotted in the same graphic.

The detection criterion is fairly rudimentary: if the spectrum lies *above* the sensitivity curve, the source will be detected. On the contrary, if the source's spectrum is below the CTA curve, the source will not be detected.

Two plots are provided for each source: the plot above shows the overall tendency and flux attenuation as the energy is increased. This could be a sign of not only EBL absorption, but also of some internal absorption mechanism of gamma-ray photons. The

[17] 100-200 MeV, 200-400 MeV, 400-800 MeV, 800-1600 MeV, 1600-3200 MeV, 3200-6400 MeV, 6400-12800 MeV, 12800-25600 MeV, 25600-51200 MeV, 51200-102400 MeV, 102400-300000 MeV

fact that LogParabola functions drop to cut-offs is also to take into account for the attenuation as the energy increases, and could also point towards internal absorption mechanisms (Brown, 2013). The plot below is a zoom into the *important* area, i.e. the area in which the positive or negative detection is determined, which corresponds to the LE regime of CTA.

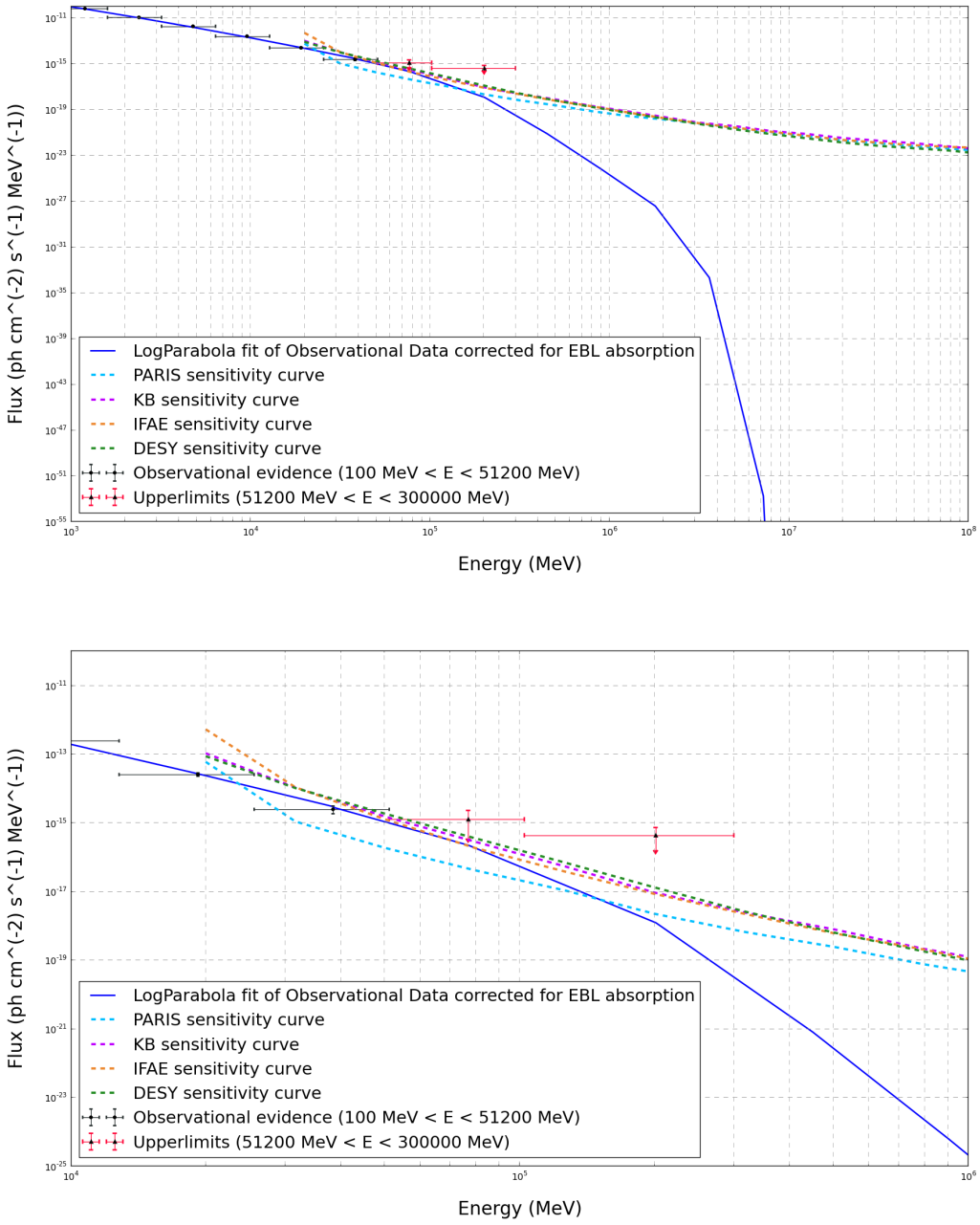

Figure 51: *Spectrum of 3C454.3 for 5-yearFermi analysis together with 50-hour PROD1 sensitivity curves. 3C454.3 is the brightest FSRQ from our sample, so it makes a good candidate to be detected by CTA. Anyhow, as the lower plot in Figure 48 shows, this source would only be detected by the PROD1 PARIS analysis out of the 4 analyses considered, which reveals that being the brightest in our sample does not straight away mean that it will be detected by the next generation ground-based gamma-ray telescope. The upper plot clearly illustrates the absorption suffered by the VHE photons from the source due to the EBL absorption: the spectrum dramatically decreases as energy rises.*

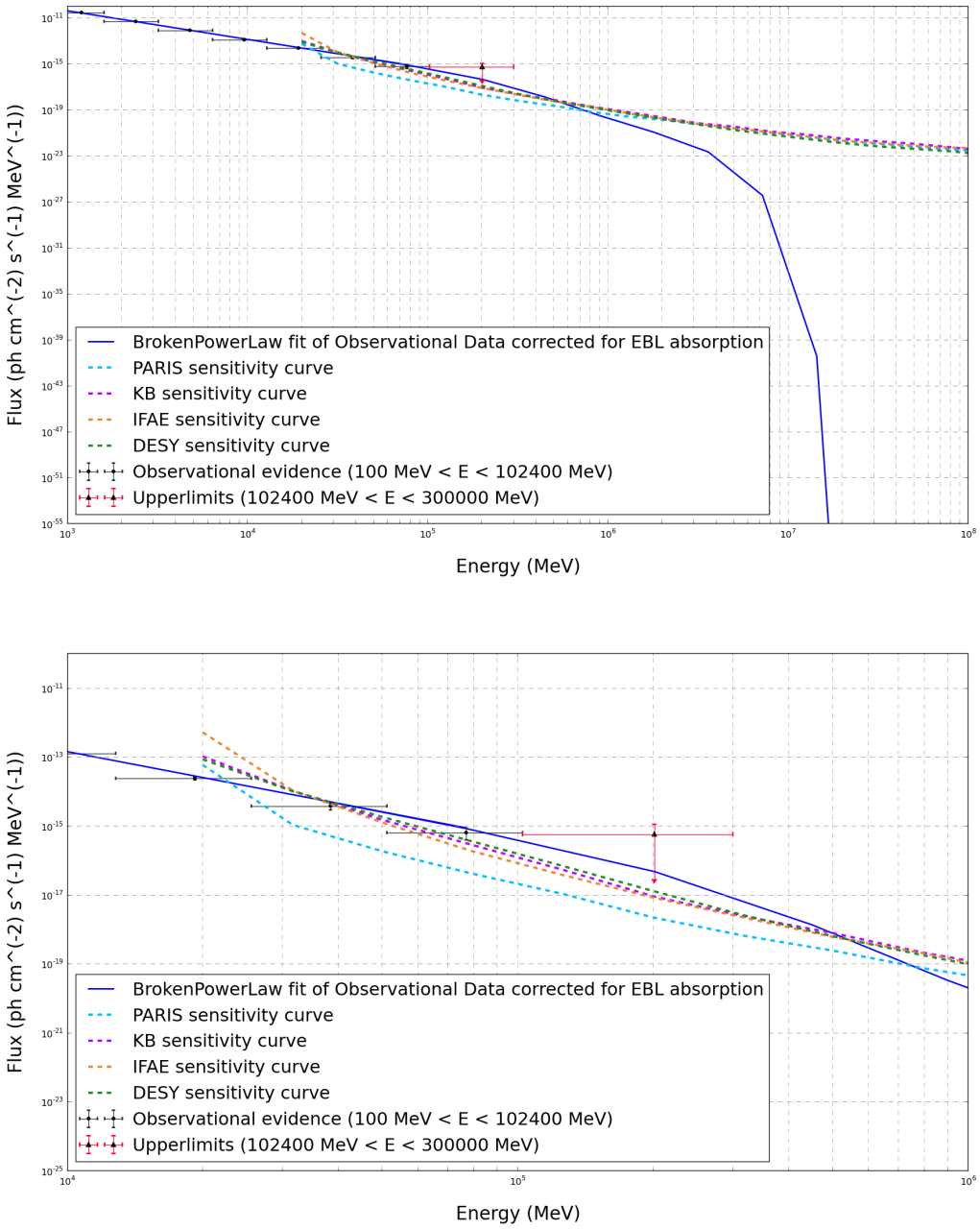

Figure 52: *Spectrum of PKS1510-089 for the 5-year Fermi analysis together with 50-hour PROD1 sensitivity curves. The case of the second brightest source considered is quite different from 3C454.3, since all the PROD1 analyses would detect the source, as can be seen in the lower plot. This is the only object which is best fitted by a BrokenPowerLaw as opposed to a LogParabola, and it has a smaller redshift than 3C454.3. Both of these factors make PKS1510-089 more likely to be detected with CTA.*

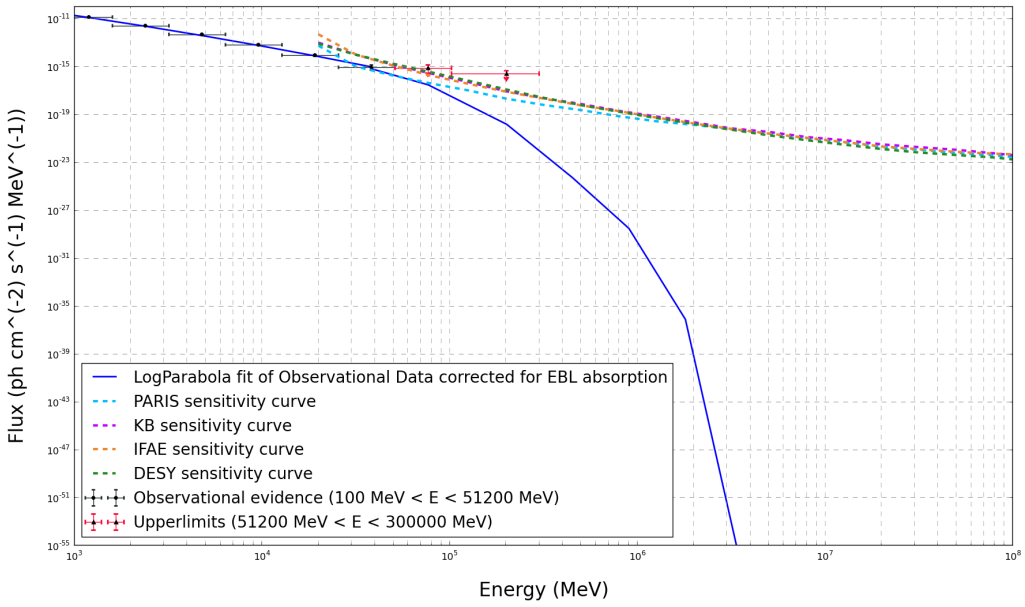

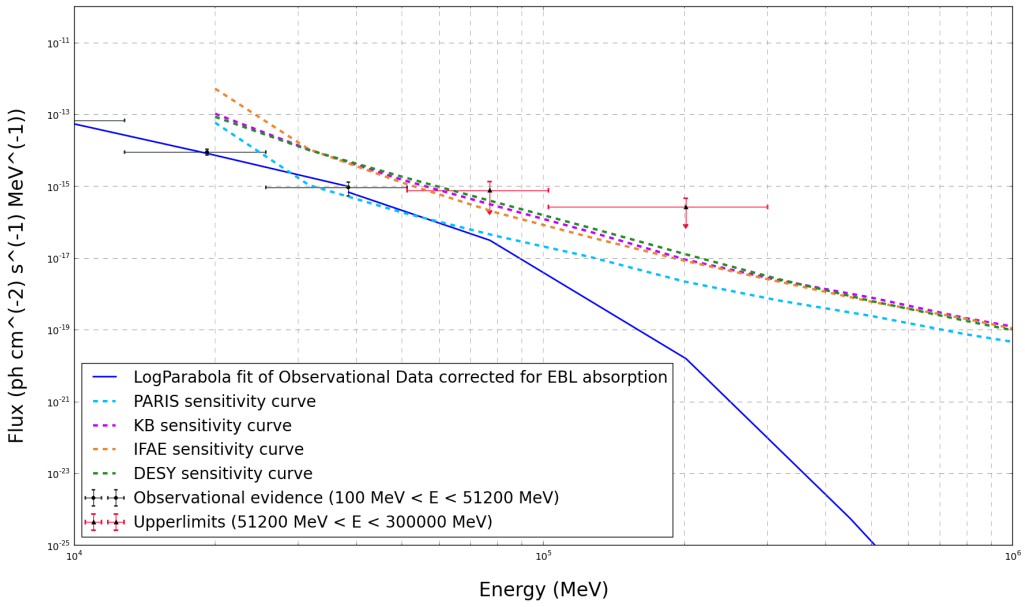

Figure 53: *Spectrum of PKS1502+106 for 5-year Fermi analysis together with 50-hour PROD1 sensitivity curves. PKS1502+106 is the third source in order of descending brightness. Contrary to PKS1510-089, our analysis suggests that CTA is unlikely to detect this source with any of the PROD1 analyses considered. Although the PARIS curve is slightly below the spectrum, is does not seem probable that PKS1502+106 will be detected given our criteria and analysis features.*

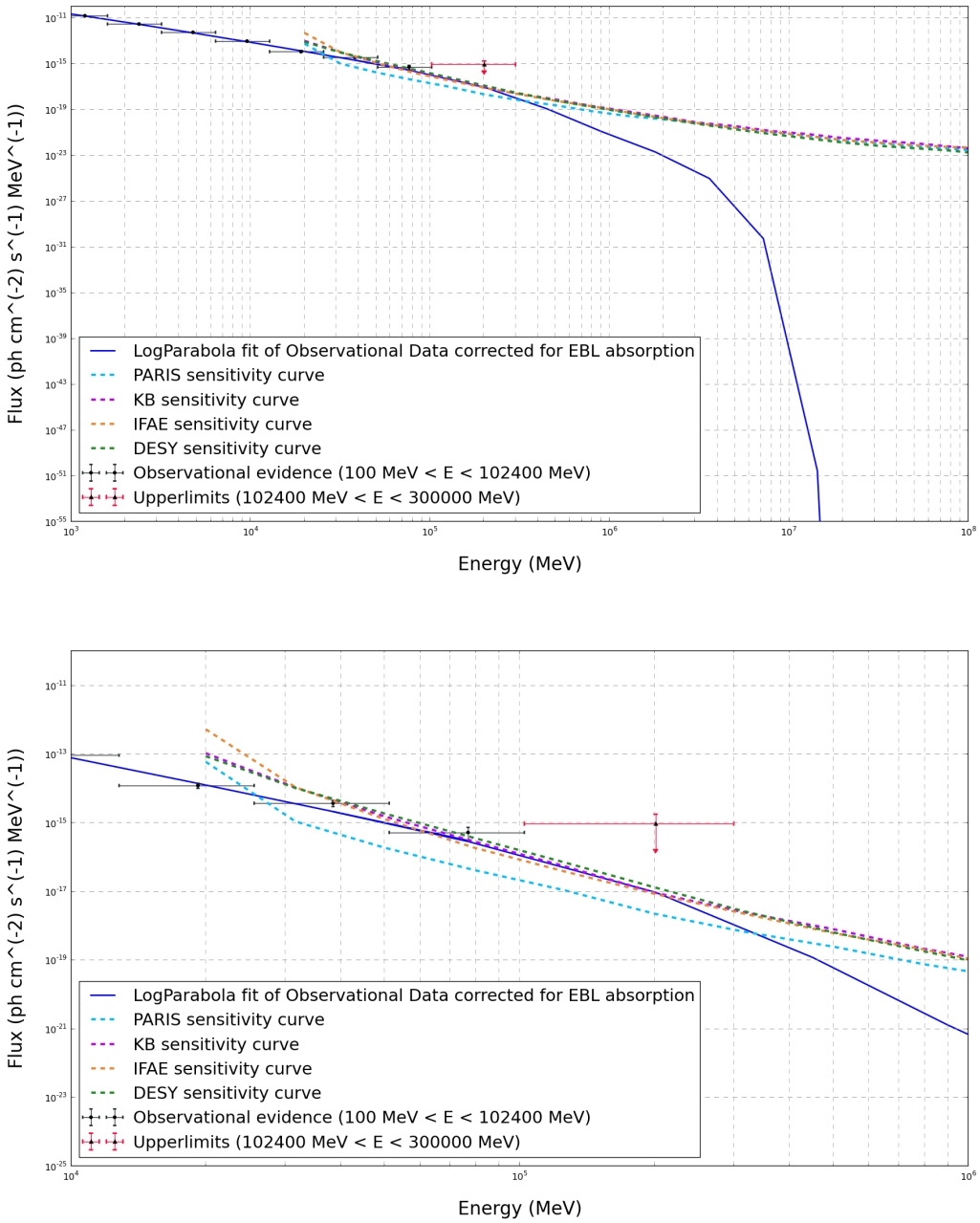

Figure 54: *Spectrum of 4C+21.35 for 5-year Fermi analysis together with 50-hour PROD1 sensitivity curves. For the 5-years' worth of data we have considered, the configuration of the PROD1 PARIS sensitivity curve would represent a positive detection of the FSRQ 4C+21.35. For the remaining 3 PROD1 analyses, it is unlikely that the object will be detected, although the sensitivity of the PROD1 IFAE curve is a bit below the spectrum.*

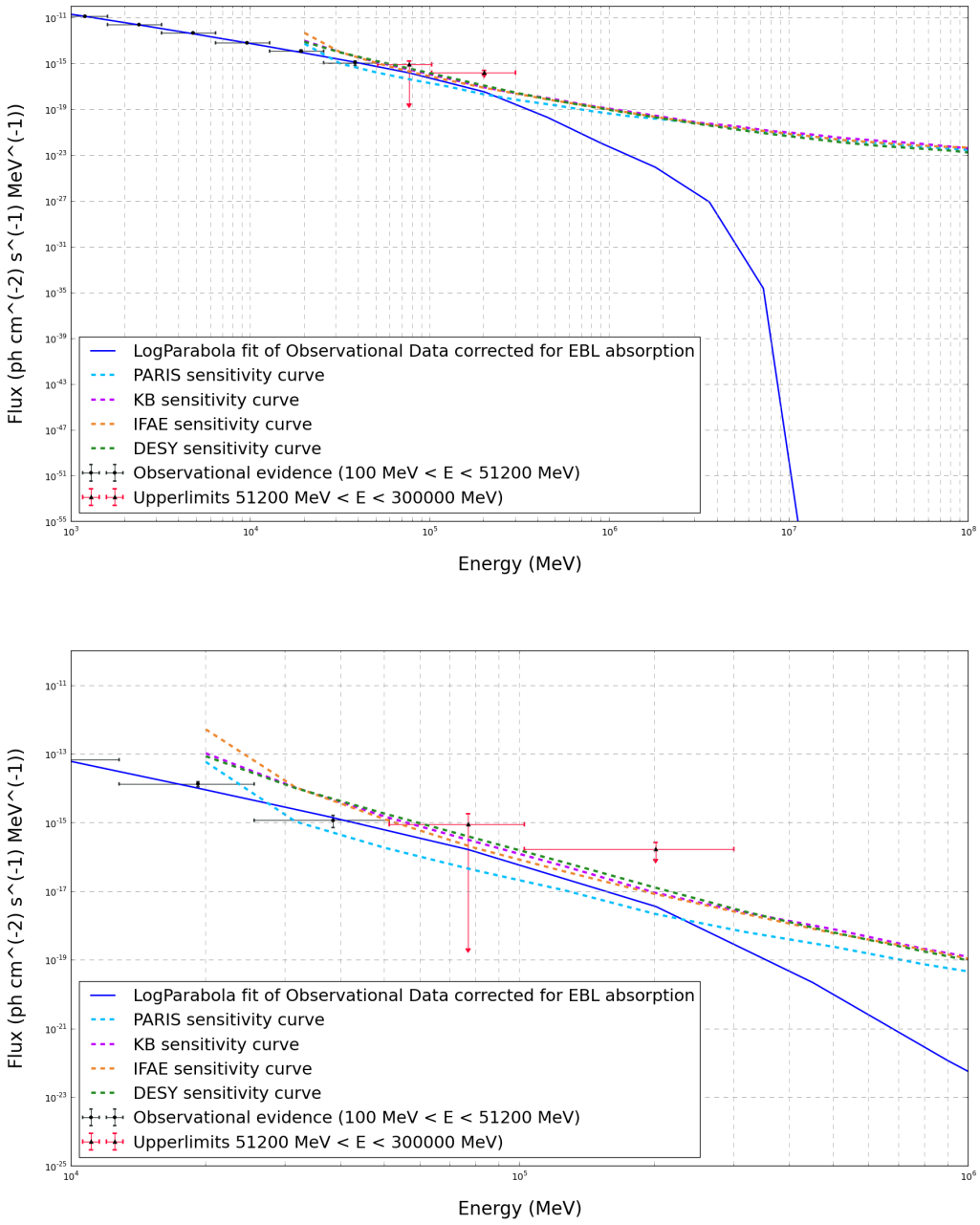

Figure 55: *Spectrum of 3C279 for 5-year Fermi analysis together with 50-hour PROD1 sensitivity curves. 3C279 is the fifth source in our list, and according to our analysis, only the PROD1 PARIS analysis would be able to detect it.*

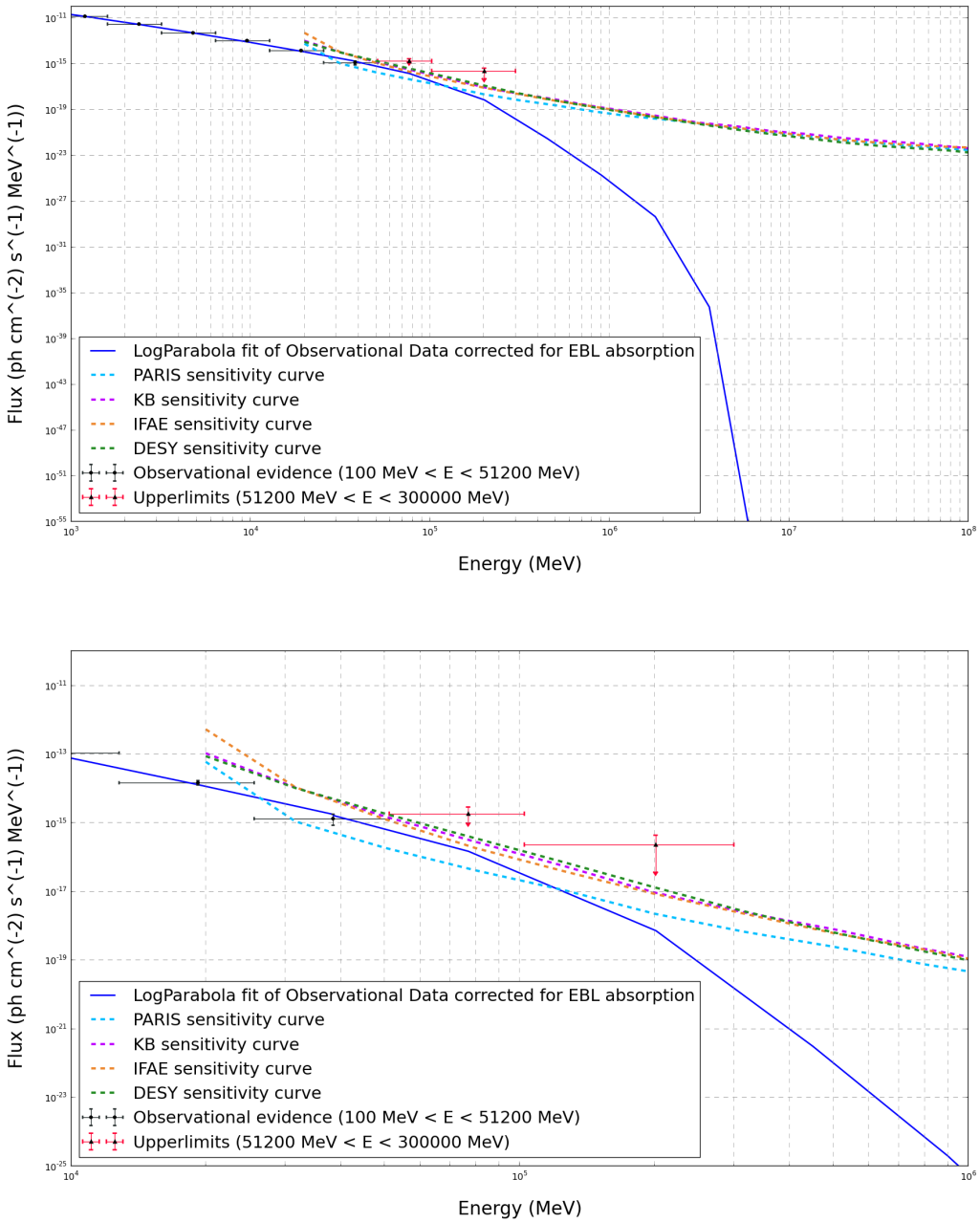

Figure 56: *Spectrum of PKS0454-234 for 5-year Fermi analysis together with 50-hour PROD1 sensitivity curves. The behaviour of this source resembles the behaviour of 3C279: only PROD1 PARIS would enable us to see the source. However, as this source is fainter than 3C279, when closely looking at the spectrum, it can be seen that PKS0454-234 is not as close to the PROD1 IFAE, DESY and KB curves. This shows that for weaker sources, it is increasingly hard to detect them by these last 3 analysis procedures.*

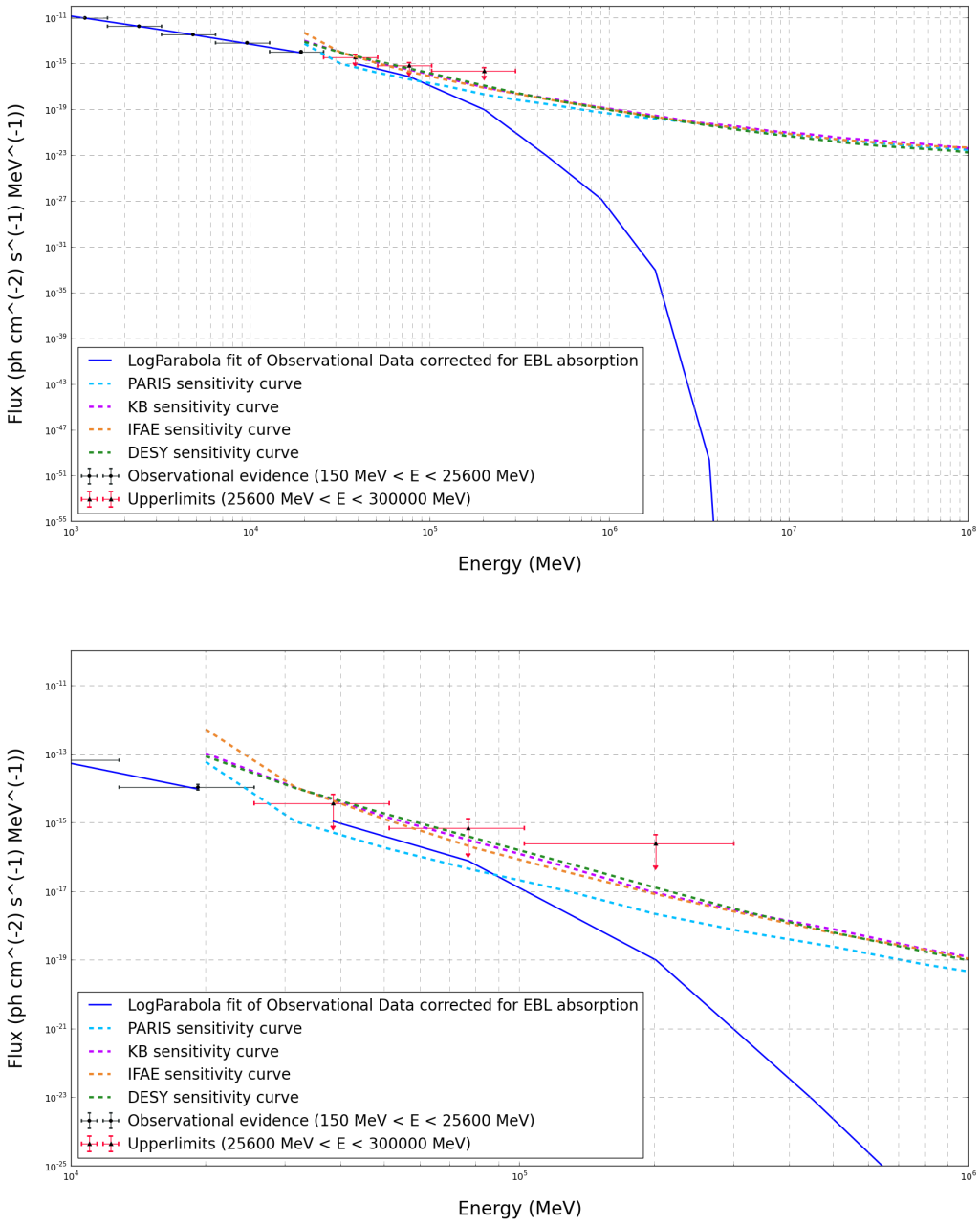

Figure 57: *Spectrum of PKS0727-11 for 5-year Fermi analysis together with 50-hour PROD1 sensitivity curves. The spectrum is getting closer to the PROD1 PARIS curve, and the remaining 3 analyses are not capable of detecting the source. In addition, the curvature of the spectrum is increasing, and hence the source is attenuated in a lower energy range compared to the brightest sources of our samples. Note that the blank space in the blue line corresponding to the spectrum is due to the fact that for this source, the last 3 energy bins of the analysis required upper limit calculation, and given the LE threshold for optical depths of the EBL model we have considered throughout this work is around 39 GeV, it was not possible to extrapolate the EBL-corrected flux to the 25.6 GeV-51.2 GeV energy bin.*

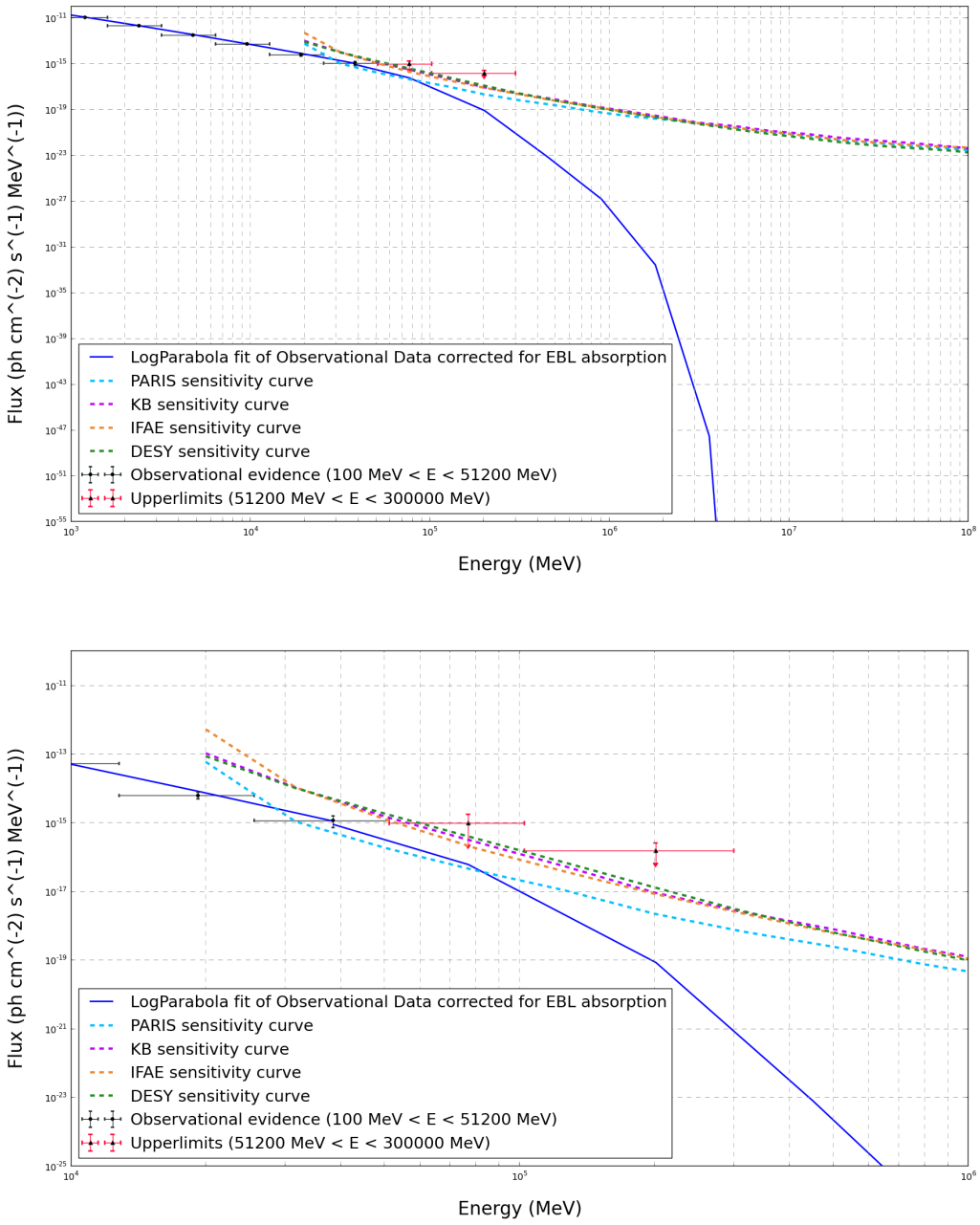

Figure 58: *Spectrum of B21520+31 for 5-year Fermi analysis together with 50-hour PROD1 sensitivity curves. As can be seen in the lower plot, the spectrum is even closer to the PROD1 PARIS curve. This relatively faint object is unlikely to be detected with CTA.*

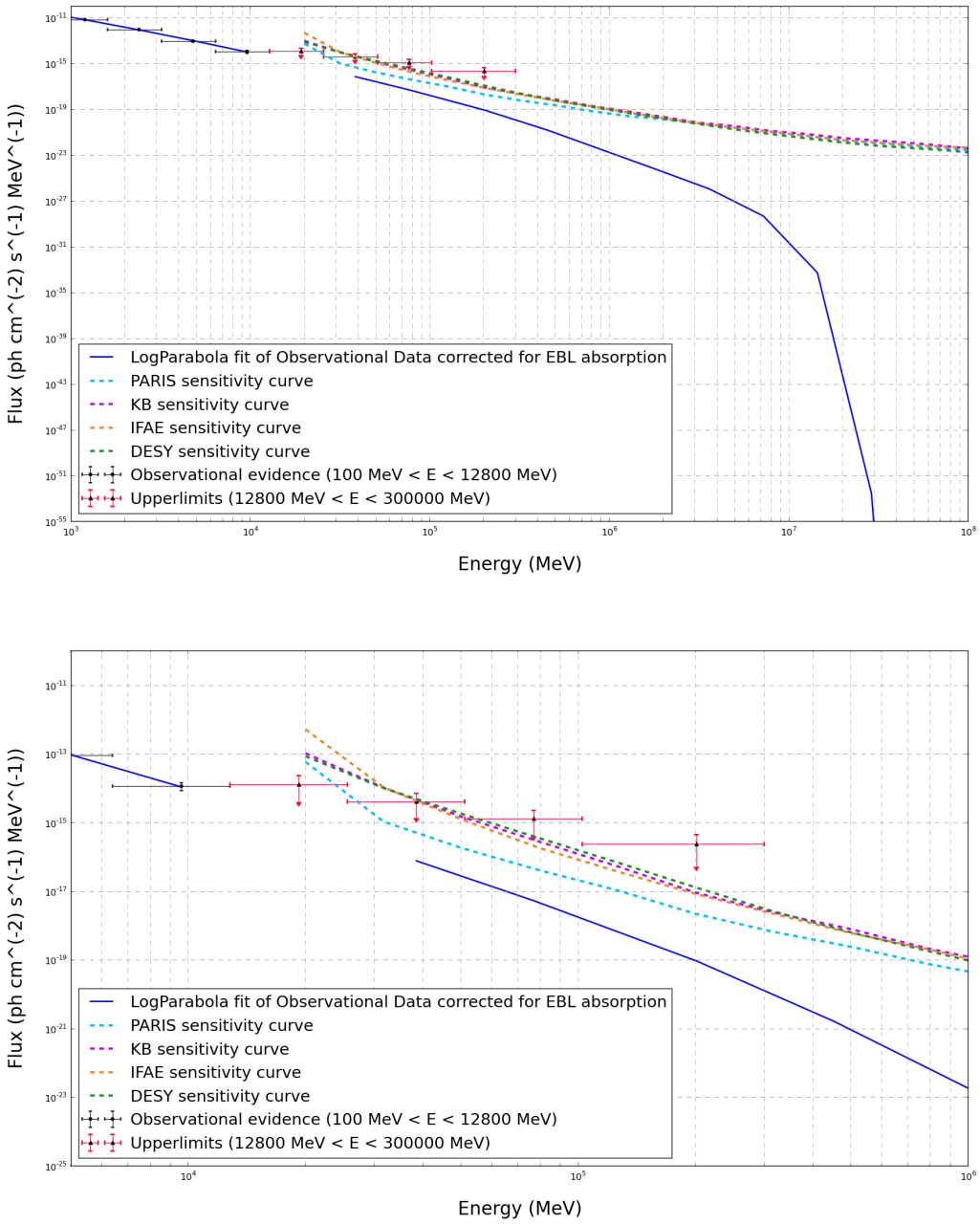

Figure 59: *Spectrum of 3C273 for 5-year Fermi analysis together with 50-hour PROD1 sensitivity curves. Unsurprisingly, for our last and faintest source, the object would not be detected by any of the PROD1 analyses considered. Fainter sources are less likely to emit photons in the VHE regime, meaning that we have fewer events for the analysis of the most energetic bins, precisely the bins that are meaningful for making comparisons with CTA, since they are in the range in which both Fermi-LAT and CTA overlap (Funk & Hinton 2013). In this case, the EBL absorption is not the tightest constraint for detection: it is obvious that the source is below the sensitivity of the CTA curves even in the lower energy range in which the EBL absorption is not an important feature.*

The results for the detection based on the spectra of the sources and the sensitivity curves are summarized in the following table:

Table 7: Qualitative detection for different configurations of CTA

Source	PARIS	KB	IFAE	DESY
3C454.3	✓	×	≈	×
PKS1510-089	✓	✓	✓	✓
PKS1502+106	≈	×	×	×
4C+21.35	✓	≈	×	×
3C279	✓	×	×	×
PKS0454-234	✓	×	×	×
PKS0727-11	✓	×	×	×
B21520+31	✓	×	×	×
3C273	×	×	×	×

Sample of 9 FSRQs analysed, and whether a source would be observed for a certain sensitivity curve. All the sensitivity curves correspond to an exposure time of 50h and array setup E. The ✓ symbol represents positive detection, × negative detection, and ≈ means that the spectrum of the source lies very close to the sensitivity curve, and given the uncertainties inherent in the extrapolation and EBL correction, it is not clear whether the object would be detected. Detection is at 5σ level.

As can be observed in the plots of the spectrum and CTA sensitivity curves, the sensitivity curve corresponding to the PARIS analysis lies below the rest of the PROD1 sensitivity curves. Hence, according to our analysis, 8 FSRQs out of nine would be detected by the PARIS analysis. Completely the opposite happens with the DESY sensitivity curve, which has the highest sensitivity threshold, with the consequent lack of detection even of the brightest FSRQs.

The same statement is applicable to IFAE and KB curves, which are in fact very similar to the DESY one, and are not likely to detect our FSRQs in long-term observation periods.

Interestingly, the only source whose best fit model is not a LogParabola, i.e. PKS1510-089, best modelled by a BrokenPowerLaw, is the single source that would be detected *all* the PROD1 sensitivity curves. When comparing the spectra of the brightest FSRQ 3C454.3 and PKS1510-089, it is noticeable that the decrease in flux due to EBL absorption is more *gradual* for PKS1510-089, due to the nature of the BrokenPowerLaw spectrum. While for the *Fermi* energy range there is not a great difference between the shape of both distributions, this changes for the CTA energy range, and the LogParabola function is attenuated more quickly and at lower energies than the BrokenPowerLaw. This tendency can be appreciated when comparing the distribution of PKS1510-089 with the rest of the sources, which are also best fitted by a LogParabola.

PKS1510-089 is also one of the three FSRQs in our sample that have been detected by ground-based gamma-ray observatories during flare states (Abramowski et al., 2014), as mentioned in Table 2. With the improved sensitivity of CTA, we would be able to observe this FSRQ even without a bright flare. Despite the improved sensitivity, though, CTA would not be able to observe the remaining two FSRQs detected at VHE range, that is, 4C+21.35 and 3C279, without a flare event.

Another interesting point is that as we move towards fainter sources in our sample, the attenuation moves steadily to lower energies for the majority of the sources modelled as LogParabolas. The spectrum of PKS1502+106, the 3rd brightest source of our FSRQs, is the one that becomes fainter most rapidly of all the FSRQs, followed by 4C+21.35, 3C279, PKS0454-234, PKS0727-11, and B21520+31, sources number 4, 5, 6, 7 and 8. Looking at Table 2, we directly see that this is most likely because PKS1502+106 is the one with largest redshift. Sources number 4, 5, 6, 7 and 8 present increasingly larger redshift values too. Therefore, a sensible reason for this larger curvature in the distributions could be the redshift of these sources (see Table 2). The absorption that the gamma-rays suffer from is redshift dependent (Eq. 9), hence, a larger redshift means the photons will suffer from larger EBL absorption because they are more exposed to EBL absorption since they have to travel longer distances until they reach the detector. However, the larger curvature of the spectrum could also point towards some mechanism of internal absorption within the inner region of the AGN (Poutanen & Stern, 2013: Brown, 2013).

Internal gamma-ray absorption is thought to be identified by the source presenting a LogParabola spectrum, which shows a spectral cut-off. This cut-off has been argued to be caused by internal absorption phenomena in FSRQs (Poutanen & Stern, 2010; Brown, 2013) that attenuate the emitted gamma-rays. From Eq. 13 can be inferred that β is the parameter which determines the curvature of the LogParabola: larger values of β result in larger curvature, and hence larger attenuation and lower fluxes. Nonetheless, this is not enough to state that sources presenting larger β values show larger curvature, and present lower fluxes due to a larger absorption. For example, the faintest FSRQ of our sample, 3C273, has the largest β value but it is not attenuated at the lowest energies. To the contrary, the spectrum of 3C73 goes up to much higher energies. As a matter of fact, 3C273 reaches the highest energies out of the 9 sources. On the other hand, PKS1502+106 has the second largest β value of the whole sample of FSRQs, and is the source that becomes fainter most rapidly of all the FSRQs in our sample.

To cast some light on this last point (whether larger β necessarily means fainter fluxes), the fluxes obtained from the binned likelihood analysis with the source modelled as the best fit model (Table 5) were plotted against the β spectral indexes from the same likelihood analysis (Figure 60). No apparent correlation is found for the two parameters. Larger β values apparently do not necessarily imply fainter fluxes.

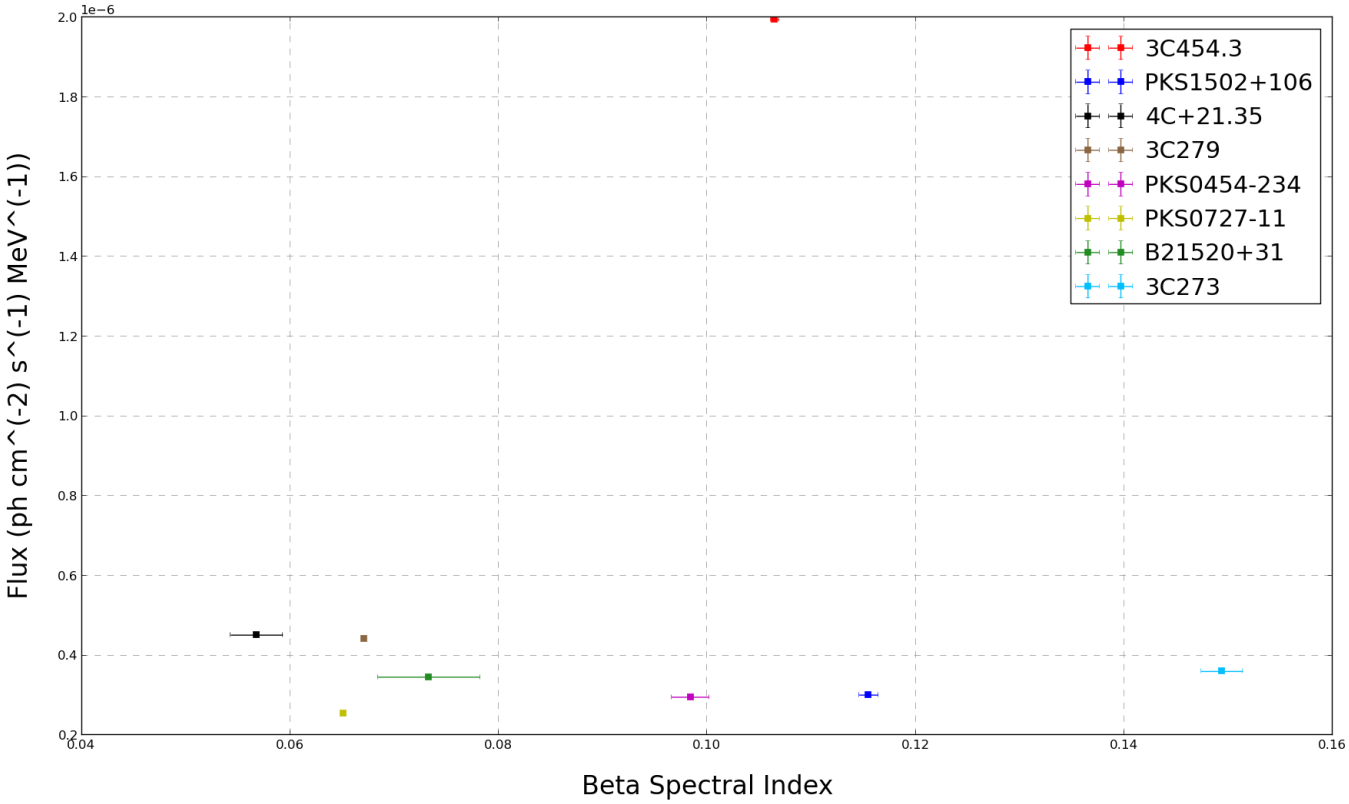

Figure 60: *Flux obtained from likelihood analysis plotted against β spectral index obtained from likelihood analysis. Only the sources best modelled with a LogParabola are plotted. No evident relation between the two factors is noticeable. Source 3C454.3 presents the highest flux of all sources, but not a remarably high or low β value.*

Moreover, trying to clarify whether the absorption is more likely to be caused by EBL or by internal absorption, we plotted the redshifts against the β spectral indexes of the 9 FSRQs (Figure 61) to discover whether a relationship between the redshift values and curvature (represented by β) exists. A correlation between redshift and β would mean that the attenuation is likely to be dominated by EBL absorption: photons from more distant sources are more attenuated since they have to travel longer distances through the EBL. Accordingly, a lack of correlation would point towards some other mechanism causing the attenuation, something intrinsic to the source rather than extrinsic. It could be due to, for instance, the afore mentioned internal absorption of gamma-rays, or due to the electrons from which the gamma-rays are created follow a spectral distribution that presents a cut-off feature. No correlation is found for all the 9 FSRQs. Anyhow, some of the sources (4C+21.35, 3C279, 3C454.3 and PKS1502+106) do present larger β values for increasing redshift values. This suggests that the EBL is not the only absorption mechanisms that attenuates the flux of these sources, and that internal absorption mechanisms are also significant.

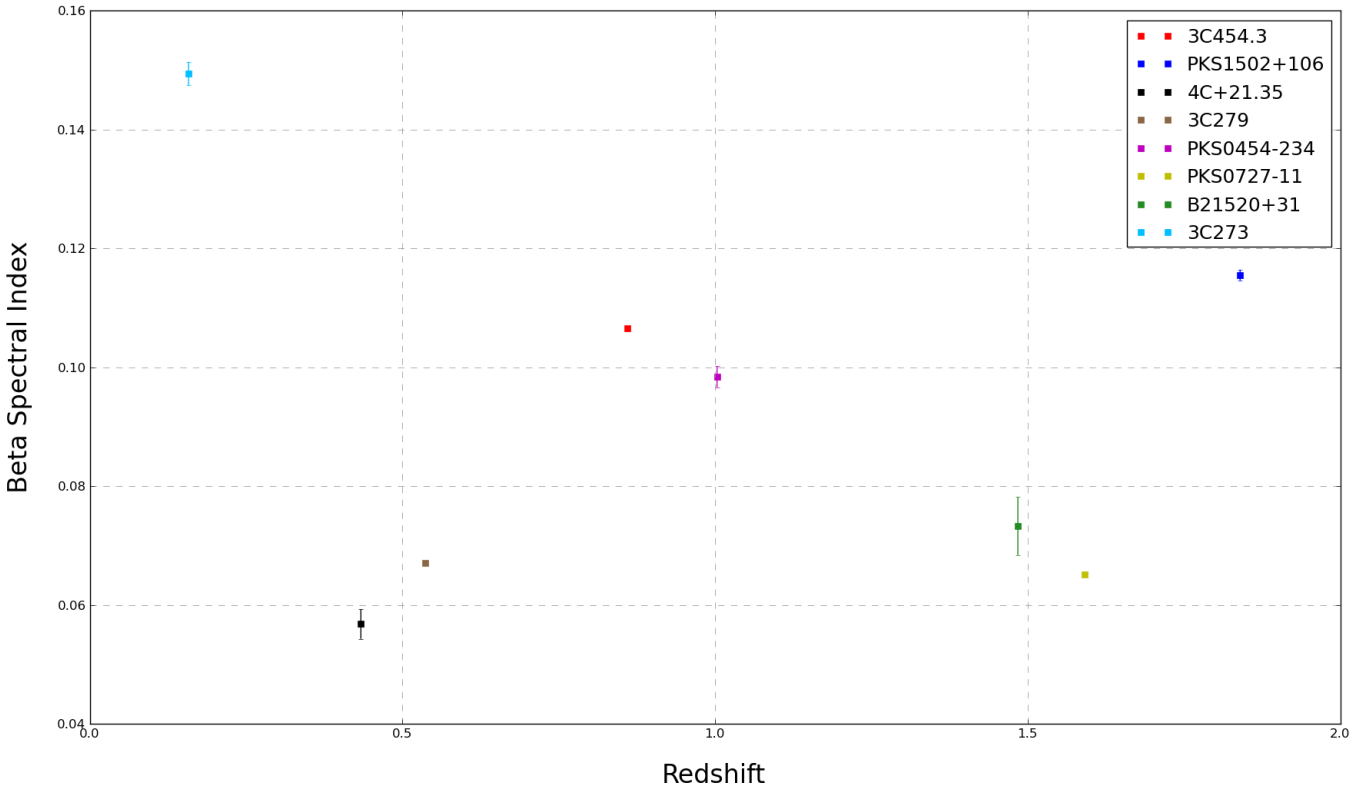

Figure 61: *Redshift of the sources from (Table 2) plotted against β spectral index obtained from likelihood analysis. Only the sources best modelled with a LogParabola are plotted. There is not a clear correlation applicable to the 9 FSRQs. However, there is a slight tendency for sources 4C+21.35, 3C279, 3C454.3 and PKS1502+106 to present larger β values for larger redshifts.*

After analysing the spectrum of the sources and qualitatively determining whether a source will be detected or not by looking at its relative position to CTA sensitivity curves, some quantitative way of identifying a positive detection seemed logical. Hence, we integrated the flux coming from the source across the *Fermi* energy range, the corrected flux across the CTA energy range and the sensitivity curves across their respective energy ranges. This way, we get a number that identifies the *average* integrated value in order to compare one to another.

To choose the most consistent integration procedure, a *manual integration* of the flux was performed to have an idea of the whereabouts of the integrated flux. Afterwards, the integrating procedure most consistent with the manual integration values was implemented . Values obtained from the integration procedure are presented in Table 7.

Table 8: Integrated flux values for sources and sensitivity curves

Source	INTEGRATED FLUX (ph/cm^2/s/MeV)
3C454.3	3.407×10^{-10}
PKS1510-089	4.716×10^{-10}
PKS1502+106	1.001×10^{-10}
4C+21.35	2.087×10^{-10}
3C279	1.618×10^{-10}
PKS0454-234	1.750×10^{-11}
PKS0727-11	1.275×10^{-11}
B21520+31	1.074×10^{-11}
3C273	1.157×10^{-12}
Sensitivity Curve	**INTEGRATED FLUX (ph/cm^2/s/MeV)**
PARIS	2.705×10^{-11}
IFAE	2.461×10^{-10}
DESY	2.481×10^{-10}
KB	2.492×10^{-10}

Table comprising the integrated values for the fluxes of the sources and the different PROD1 sensitivity curves. Fluxes have been integrated in the energy range of the CTA sensitivity curves, so that a meaningful comparison can be made between the sources and the sensitivity curves.

The minimum energy boundary for integrating the fluxes was the minimum energy value for which the CTA sensitivity curves could be calculated (i.e 19954 MeV), while the maximum boundary was set by the maximum energy for which the EBL corrected flux could be calculated (i.e. 72 TeV). These limits have been applied to both the CTA curves and the spectrum of the sources, enabling a sensible comparison between them to be made.

The results obtained from integration are consistent to the ones obtained from the more qualitative detection criteria. Again, the PARIS sensitivity curve is likely to detect all the FSRQs, whereas the remaining 3 sensitivity curves lie above the integrated fluxes of the sources for long-term analysis.

PKS1510-089 shows the highest integrated flux (4.716×10^{-10} ph/cm^2/s/MeV), even greater than the flux for the brightest FSRQ 3C454.3 (3.407×10^{-10} ph/cm^2/s/MeV). On the other hand, the lowest flux corresponds to PKS1502+106 (1.001×10^{-10} ph/cm^2/s/MeV), due to the large attenuation suffered by the flux of this source.

6. ANALYSIS OF THE SOURCES DURING FLARE EVENTS

After analysing the sources' behaviour for a 5-year period, the next step was to cast some light on the flaring state of the FSRQs, and whether CTA would be able to see the sources when they enter such an active state. The fact that a source is not detected in the 5-year analysis by a certain sensitivity curve does not necessarily mean that it will not be detected when it enters a flaring state: flares are very active periods of enhanced activity and brightness. Militating against this is the short duration of flare events, which makes long observations impossible. Therefore, it is interesting to try to predict whether this enhanced brightness will be 'bright' enough to be detected by CTA. For instance, PKS1510-089, the second FSRQ in our sample, has already been detected in the VHE during one of its flaring periods. This chapter explains the steps followed for the flare event analysis, which is mostly very similar to the analysis done for the long-term analysis of the sources. Only the first 5 sources, the brightest ones from our sample, were considered for flare event analysis.

1. Analysis of the sources during brightest flare events

The first thing to do in order to observe the sources during flaring periods is, logically, to identify these periods of enhanced activity. One of the simplest ways to detect a flare event is to look at the *Light Curves* (LCs) of the source. Hence, LCs of the whole 5 years of data were produced with the user contributed **like_lc.pl** tool available in the FSSC website. LCs are produced by binning the 5-year data in *time bins* of a certain duration. In the present work, all 5 years of data were split into 2 weekly bins, a time span large enough to appreciate a flare in the LC and small enough not to require a long computation period. In addition, a threshold TS value of 10 (only events with TS$>$ 10 were taken into account) was chosen. This results in the non-detection of the object in certain time bins.

The rest of the criteria were the same as for the long-term analysis. An unbinned likelihood analysis was performed for each of the time bins, obtaining not only the flux values for each of the bins, but also the spectral indexes and TS values of the sources

from the **gtlike** *Fermi* tool.

In this work, we only considered the **brightest** flare interval for each of the sources in the sub-sample of 5 FSRQs. The brightest flare is identified as the highest peak of the flux in the 5-year LC of each source. The following Figures show the 2-weekly LCs for the 5 FSRQs. The time in MJD is plotted in the abscissa, whereas the ordinate shows the flux values in units of photons per centimetre square per second (ph/cm^2/s). The statistical error bars from the likelihood analysis are also plotted in the LCs. The systematic errors concerning the telescope, which are mainly energy dependent, have not been explicitly considered for this work.

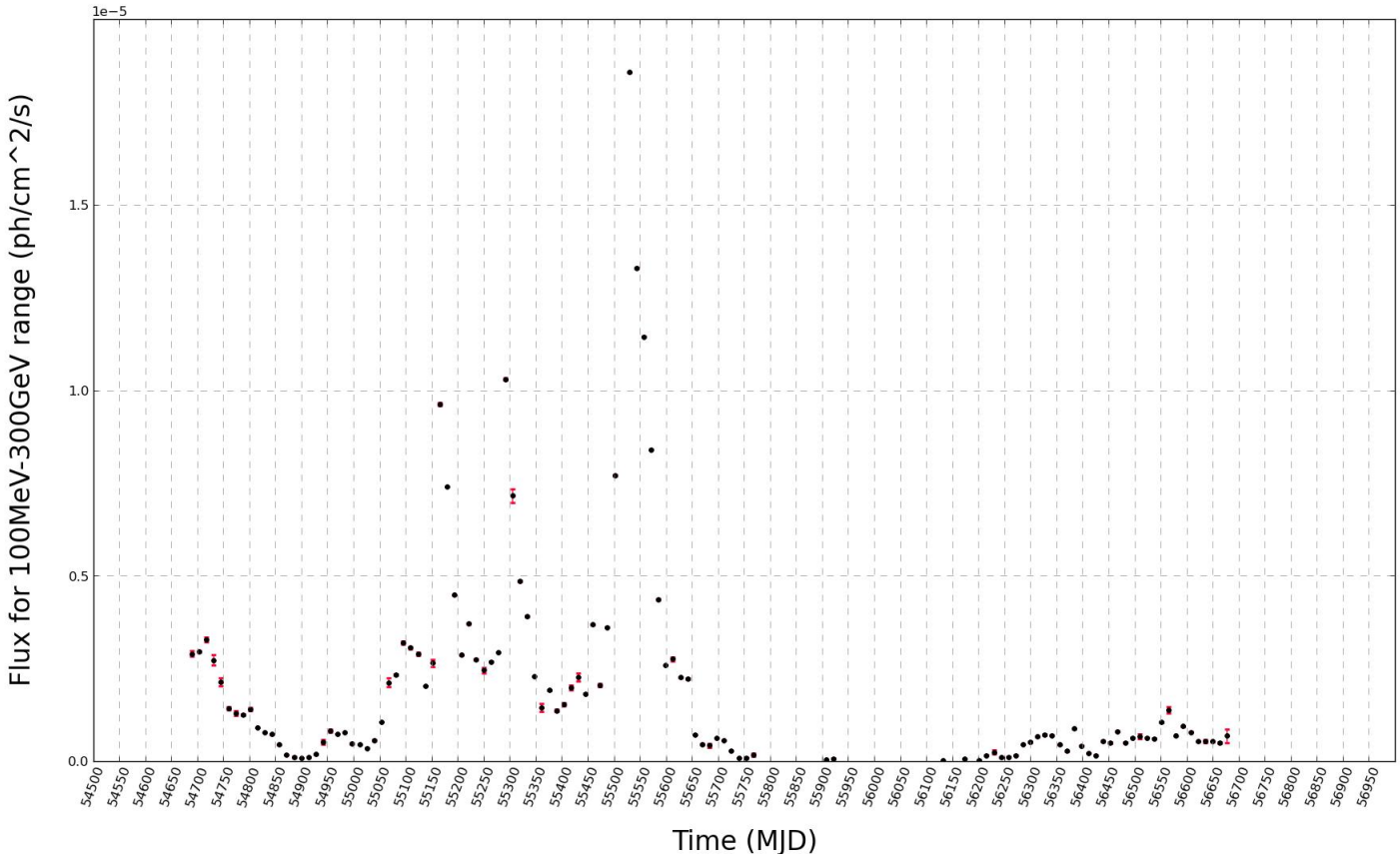

Figure 62: *2-weekly binned light curve for source 3C454.3. Several bright flares are obvious, followed by some periods of time for which the source is not even detected, or very low fluxes are detected.*

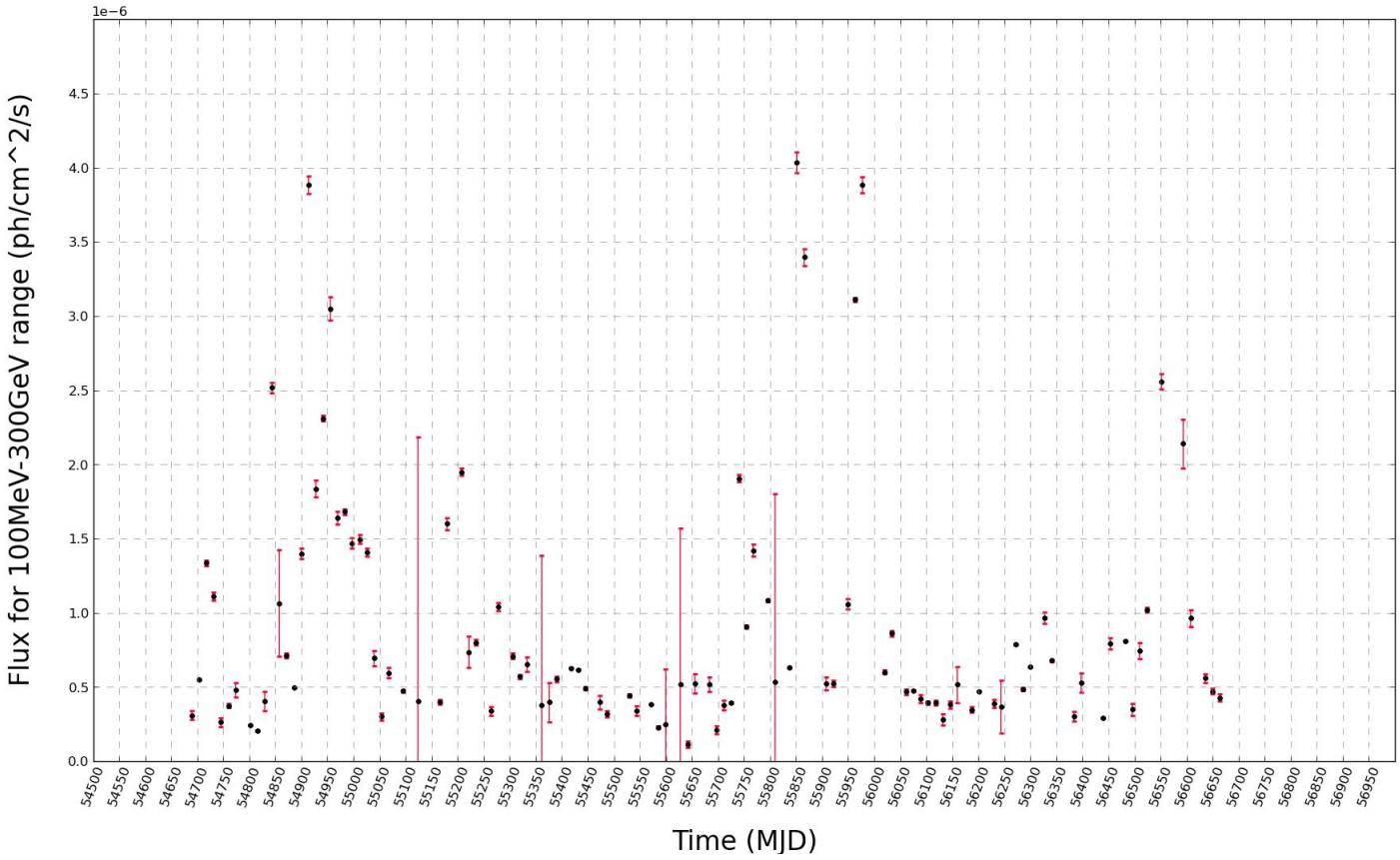

Figure 63: *2-weekly binned light curve for source PKS1510-089.*

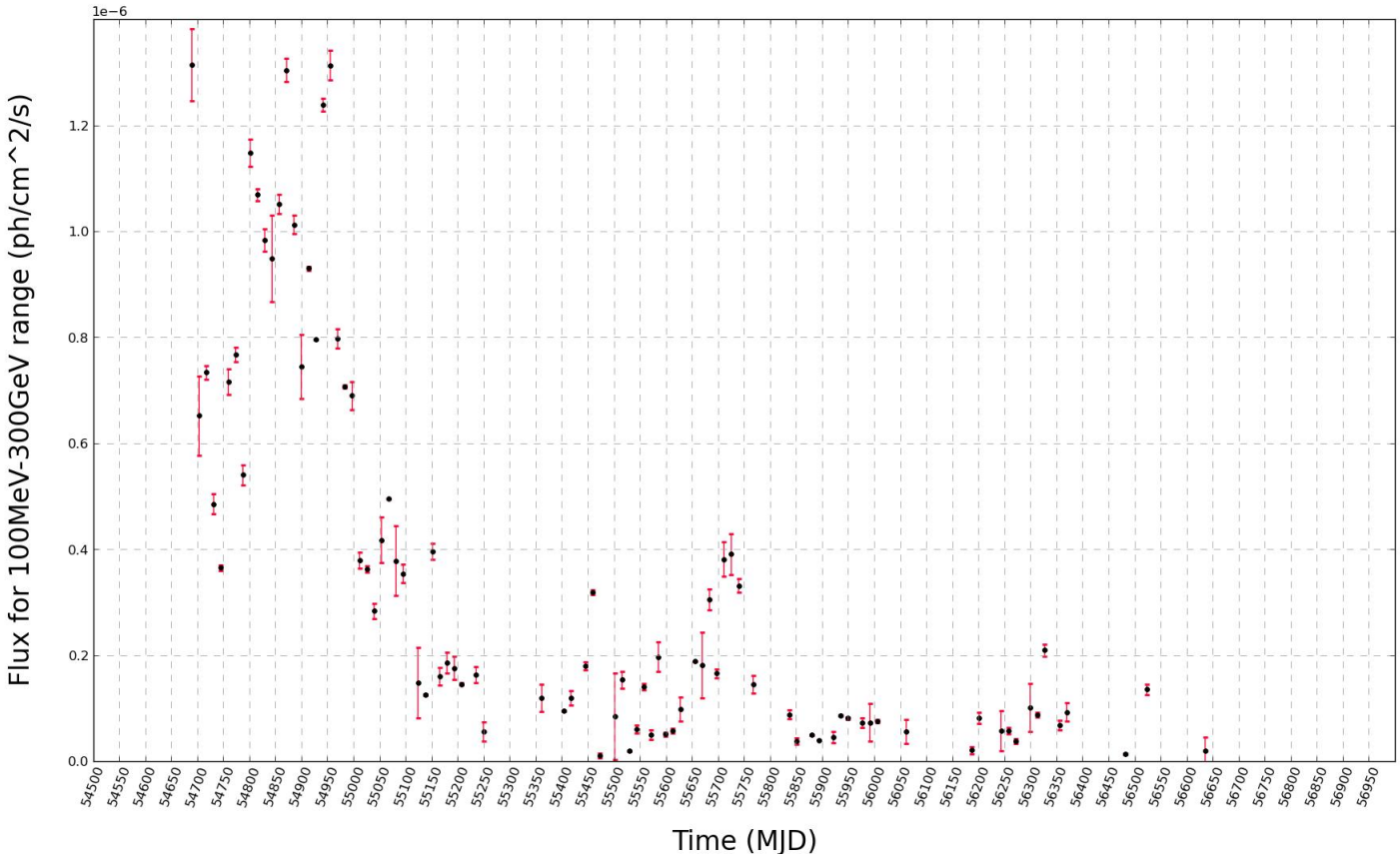

Figure 64: *2-weekly binned light curve for source PKS1502+106.*

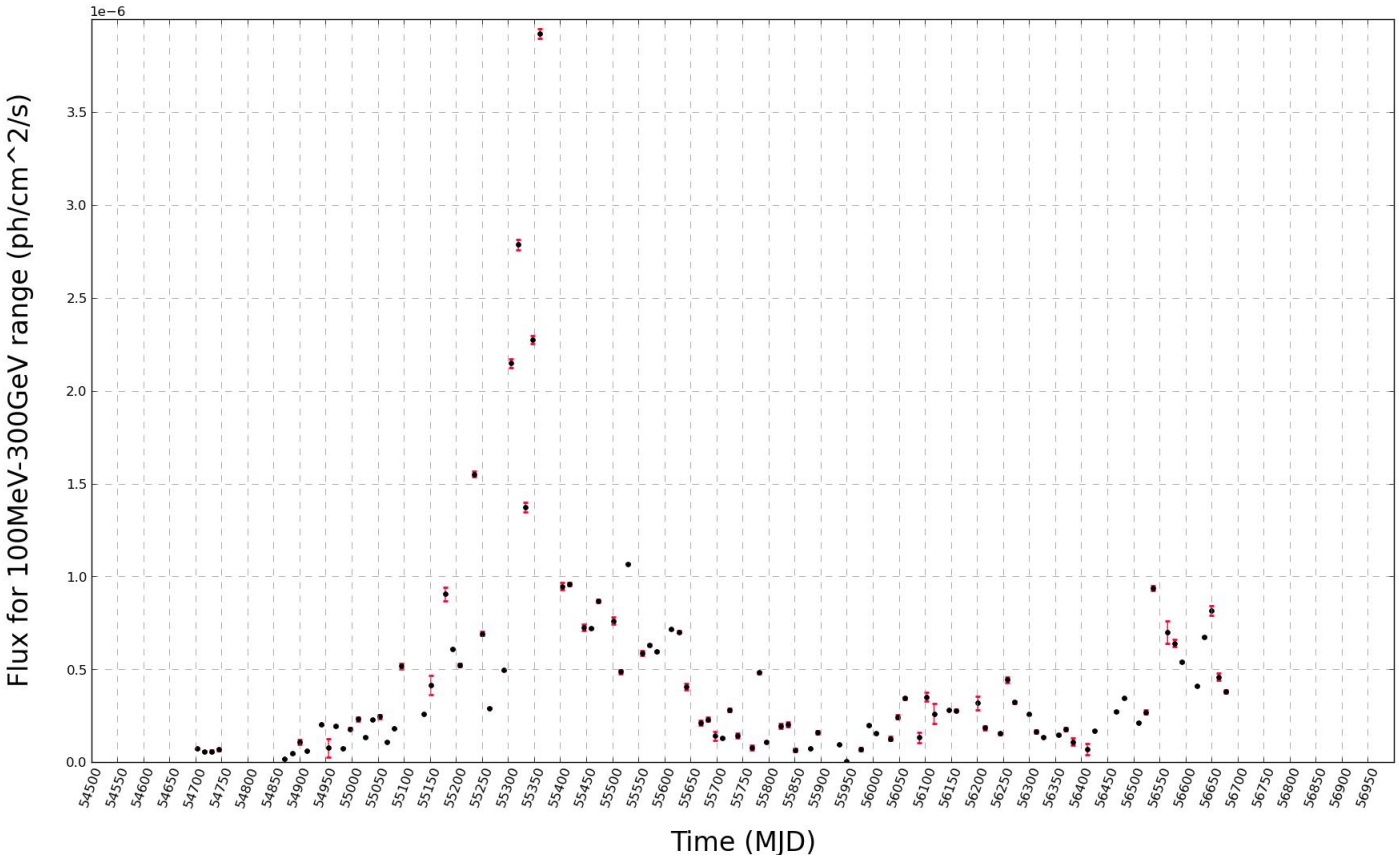

Figure 65: *2-weekly binned light curve for source 4C+21.35.*

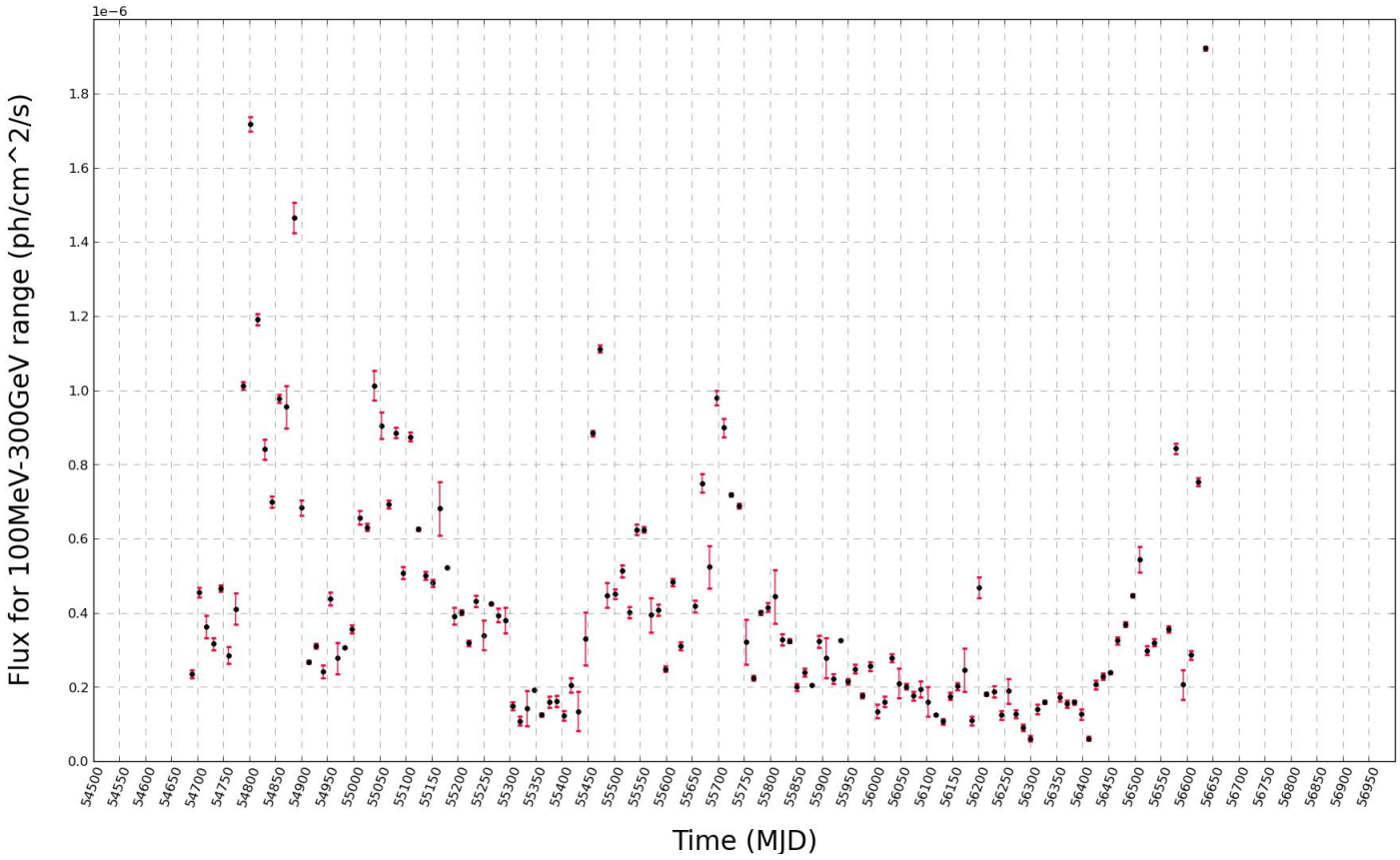

Figure 66: *2-weekly binned light curve for source 3C279.*

To identify the exact interval when the flare happened in the LCs, the flare events were approximately identified by eye in the 2-weekly LCs, and a daily binned LC was produced for those periods, in order to accurately determine the duration of the flare. The daily binned LCs are presented in the following plots.

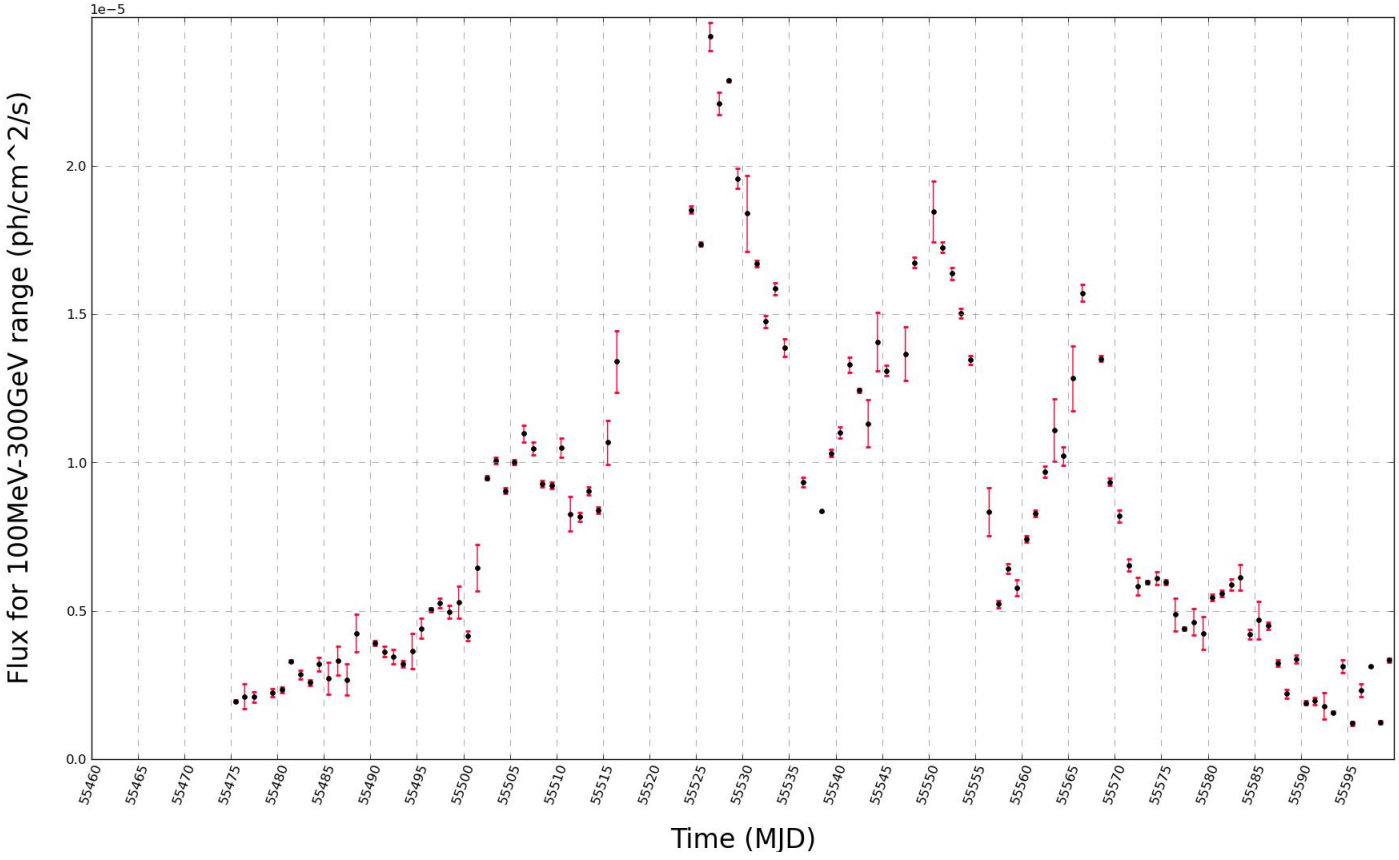

Figure 67: *Daily binned light curve for source 3C454.3.*

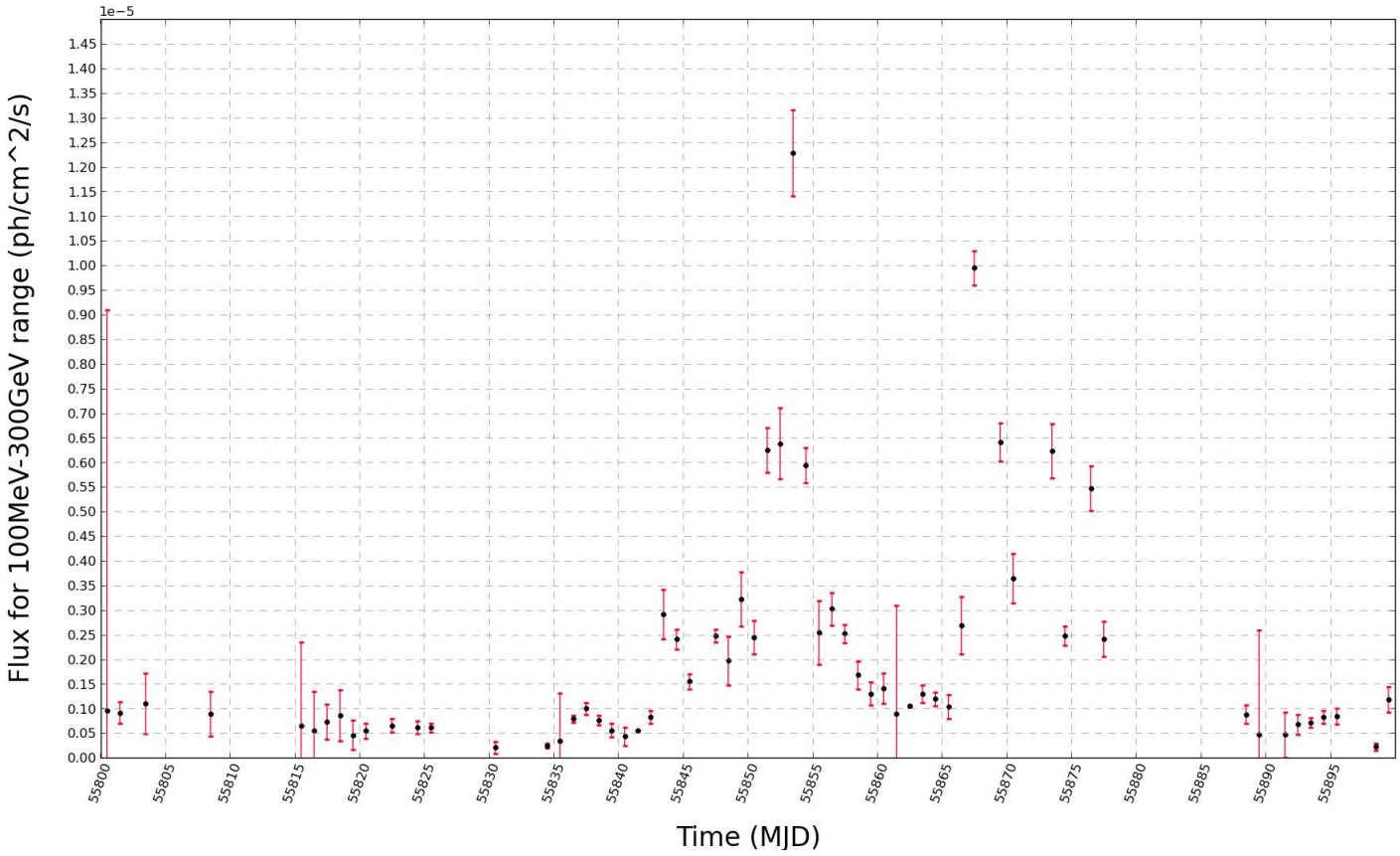

Figure 68: *Daily binned light curve for source PKS1510-089.*

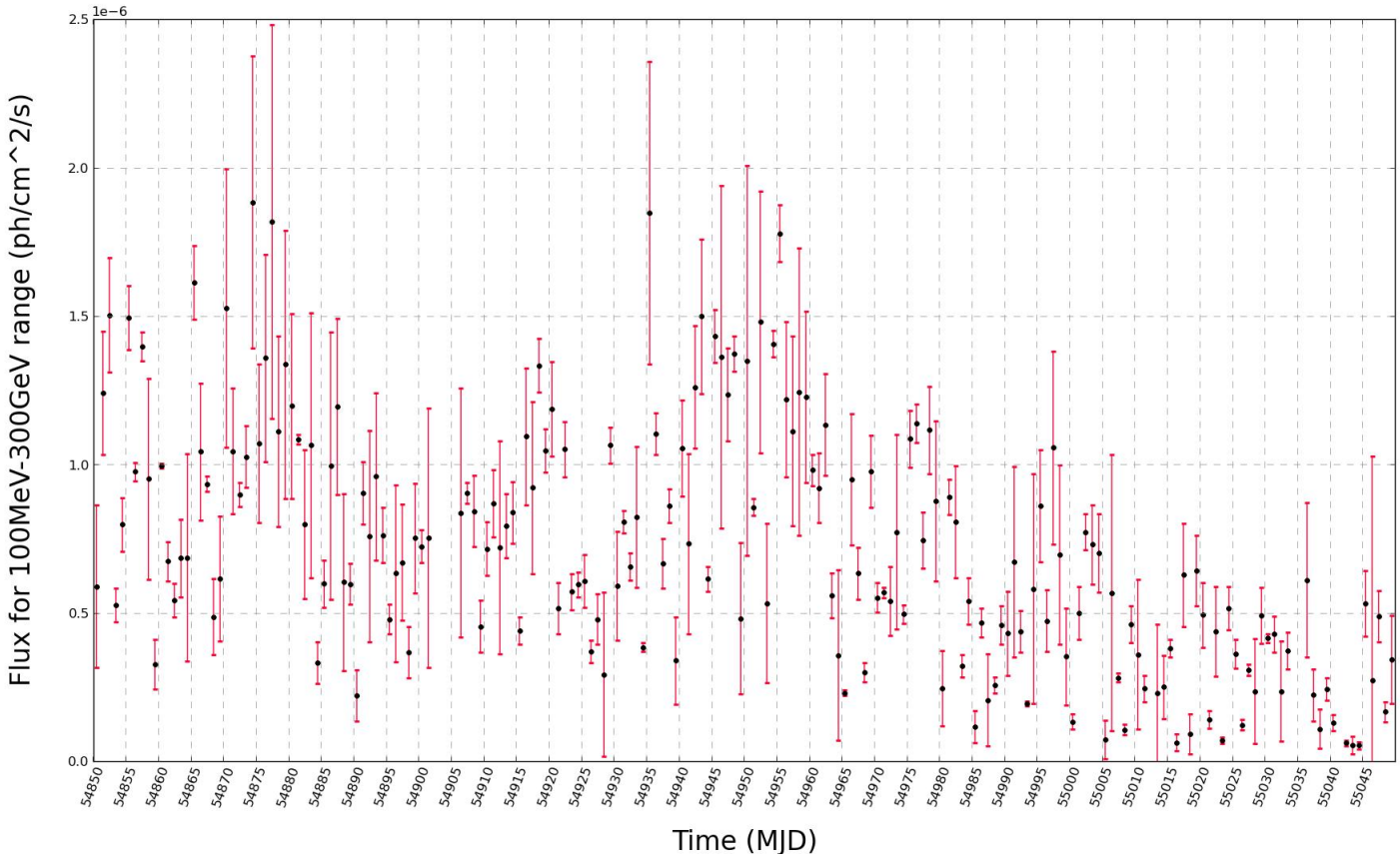

Figure 69: *Daily binned light curve for source PKS1502+106.*

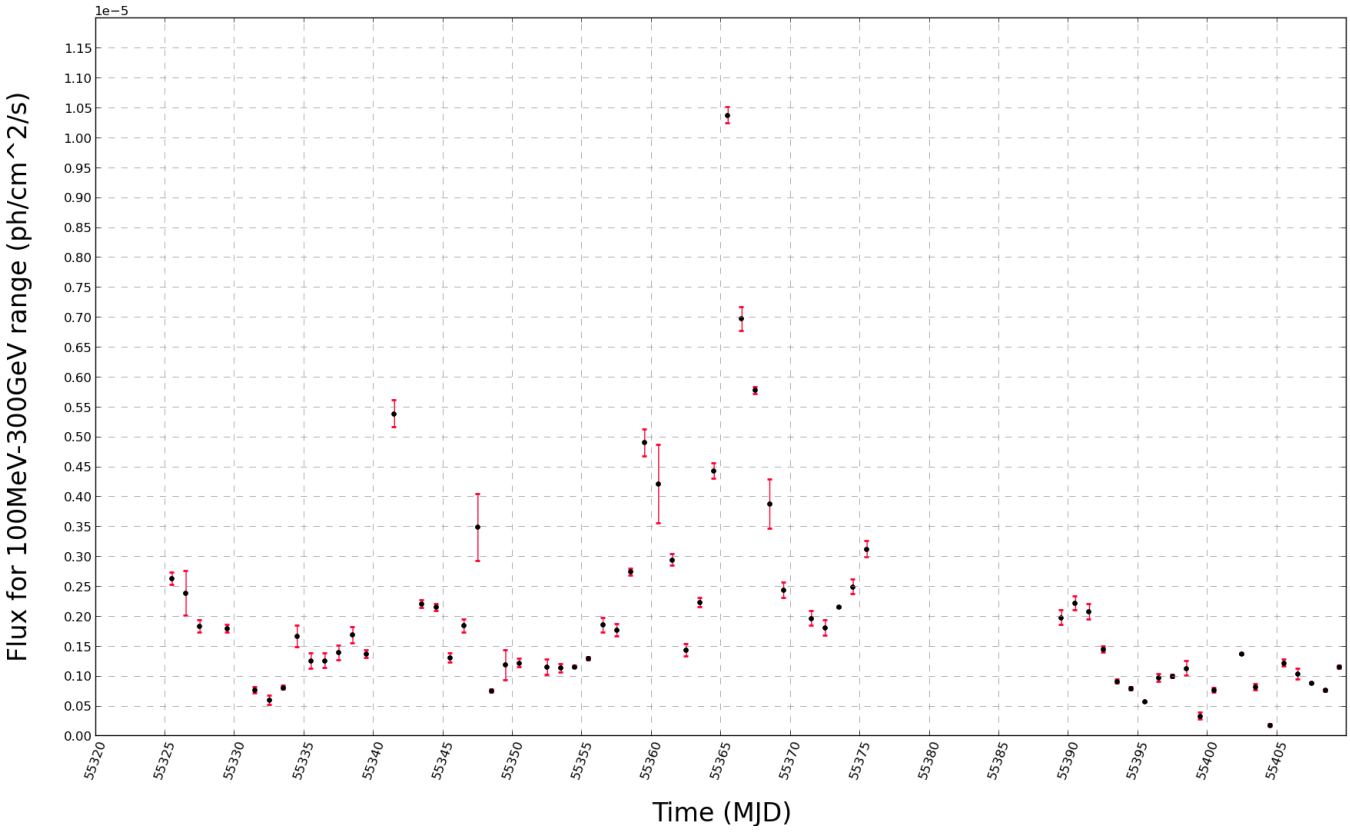

Figure 70: *Daily binned light curve for source 4C+21.35.*

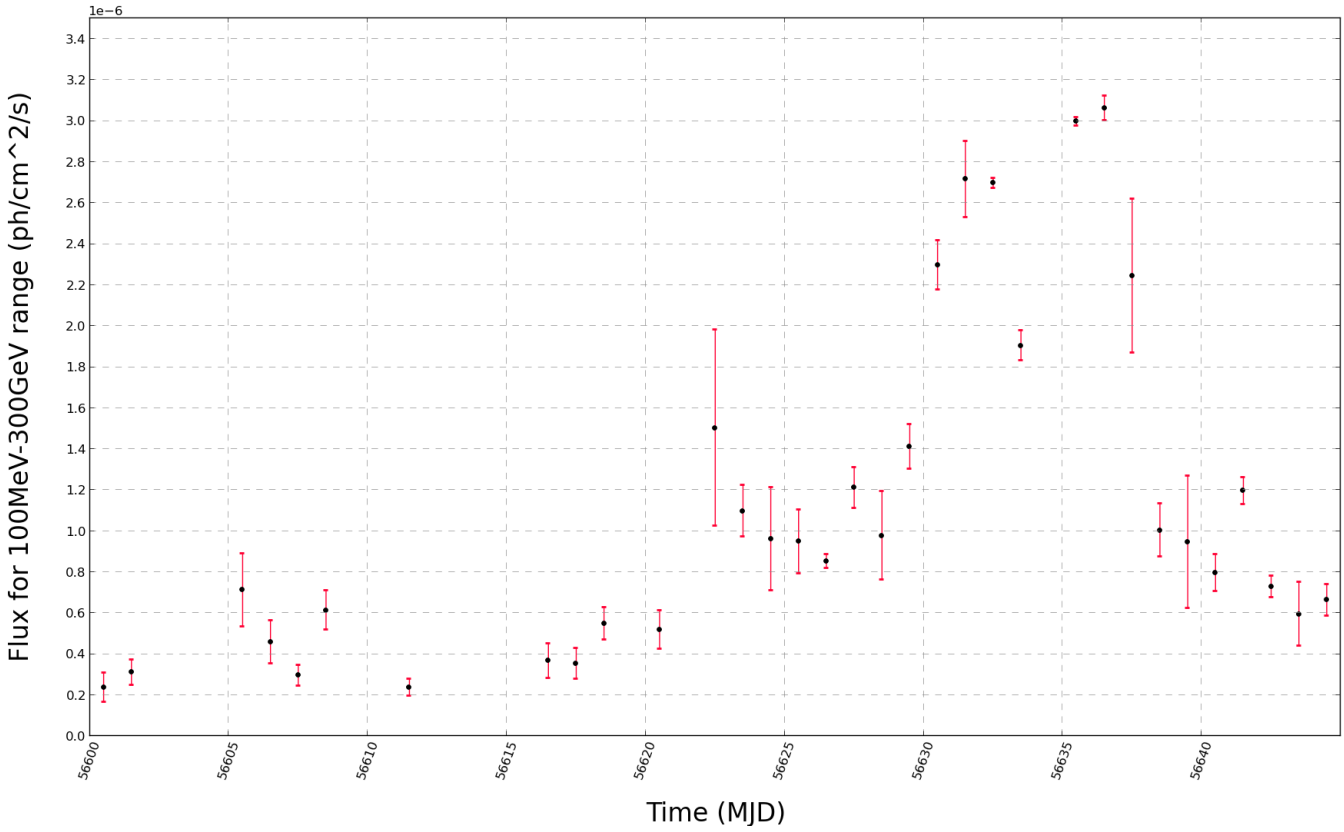

Figure 71: *Daily binned light curve for source 3C279.*

For flare event analysis, it is interesting to know whether the spectral shape of a source, varies much during the analysed period of time. This is related to the existence of a correlation between the spectral index of the source and the fluxes. The lack of a correlation means that one can integrate the flux in as long a period of time as the whole flare event. To discover a possible correlation, we plotted the observed fluxes against

- the spectral indexes α and β for sources whose best fit model is a LogParabola (Eq. 13)
- the spectral indexes γ_1 and γ_2 for the source best modelled as a BrokenPowerLaw (Eq. 11)

over the whole 5-year data set.

The plots of spectral indexes α and β versus detected *Fermi* fluxes are presented in Figures 68-72, first spectral index (α for LogParabola fits, Eq. 13, and γ_1 for BrokenPowerLaw fits, Eq. 11) vs flux on the left plot, and second spectral index (β for LogParabola, Eq. 13, and γ_2 for BrokenPowerLaw, Eq. 11) vs flux on the right. No apparent correlation between indexes and fluxes is found. The flaring periods are presented in Table 8.

Table 9: Flaring period for brightest sources

SOURCE	MET	MJD	DATE
3C454.3	308016002-318816002	55475-55600	2010/10/06 - 2011/02/08
PKS1510-089	336096002-344736002	55800-55900	2011/08/27 - 2011/12/05
PKS1502+106	254016002-271296002	54850-55050	2009/01/19 - 2009/08/07
4C+21.35	295056002-302400002	55325-55410	2010/05/09 - 2010/08/02
3C279	405216003-413856003	56600-56700	2013/11/04 - 2014/02/12

List of five brightest sources analysed during flare events. The period in which the brightest flare happened according to the 2-weekly binned LC is presented in the Mission Elapsed Time (MET) in column 1, in Modified Julian Date (MJD) in column 2 and in ISO 8601 date in column 3.

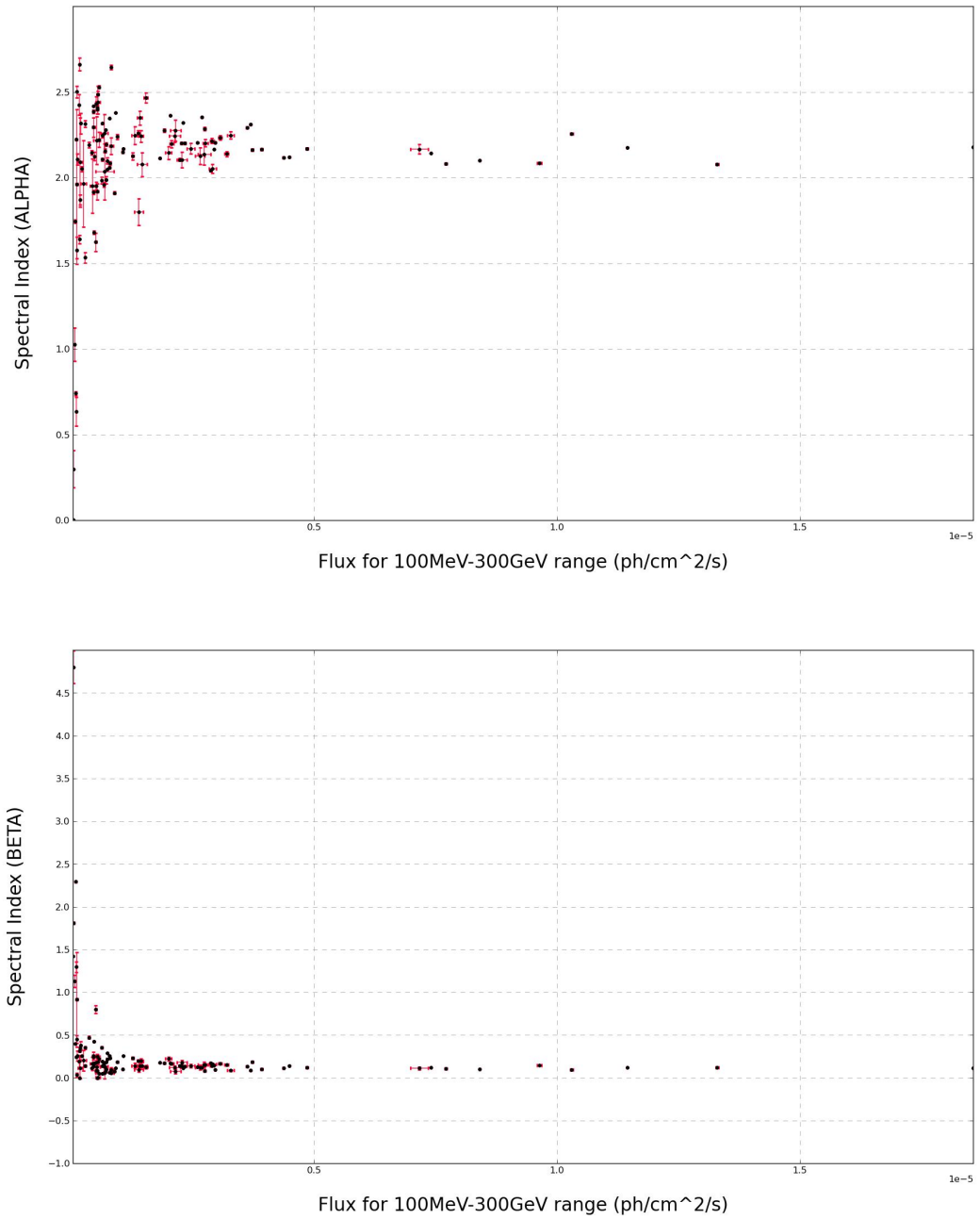

Figure 72: *Spectral indexes versus flux for source 3C454.3. ABOVE - α vs flux. BELOW - β vs flux. No correlation between flux and spectral index is found. Low flux values present larger error bars possibly due to low statistics in this range, resulting in low TS values (and hence significance) of these events.*

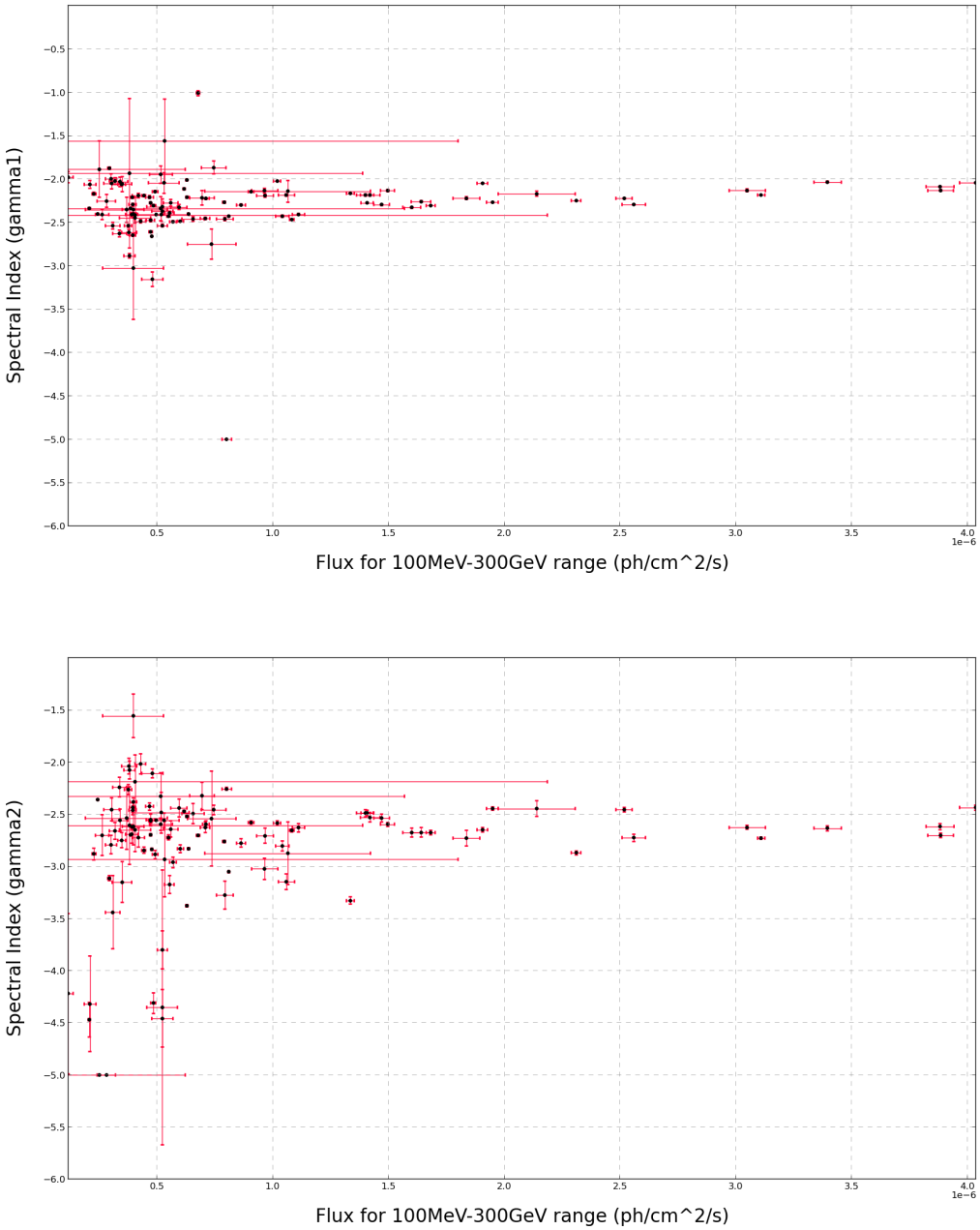

Figure 73: *Spectral indexes versus flux for source PKS1510-089. ABOVE - γ_1 vs flux. BELOW - γ_2 vs flux. No correlation between flux and spectral index is found. Low flux values present larger error bars possibly due to low statistics in this range, resulting in low TS values (and hence significance) of these events.*

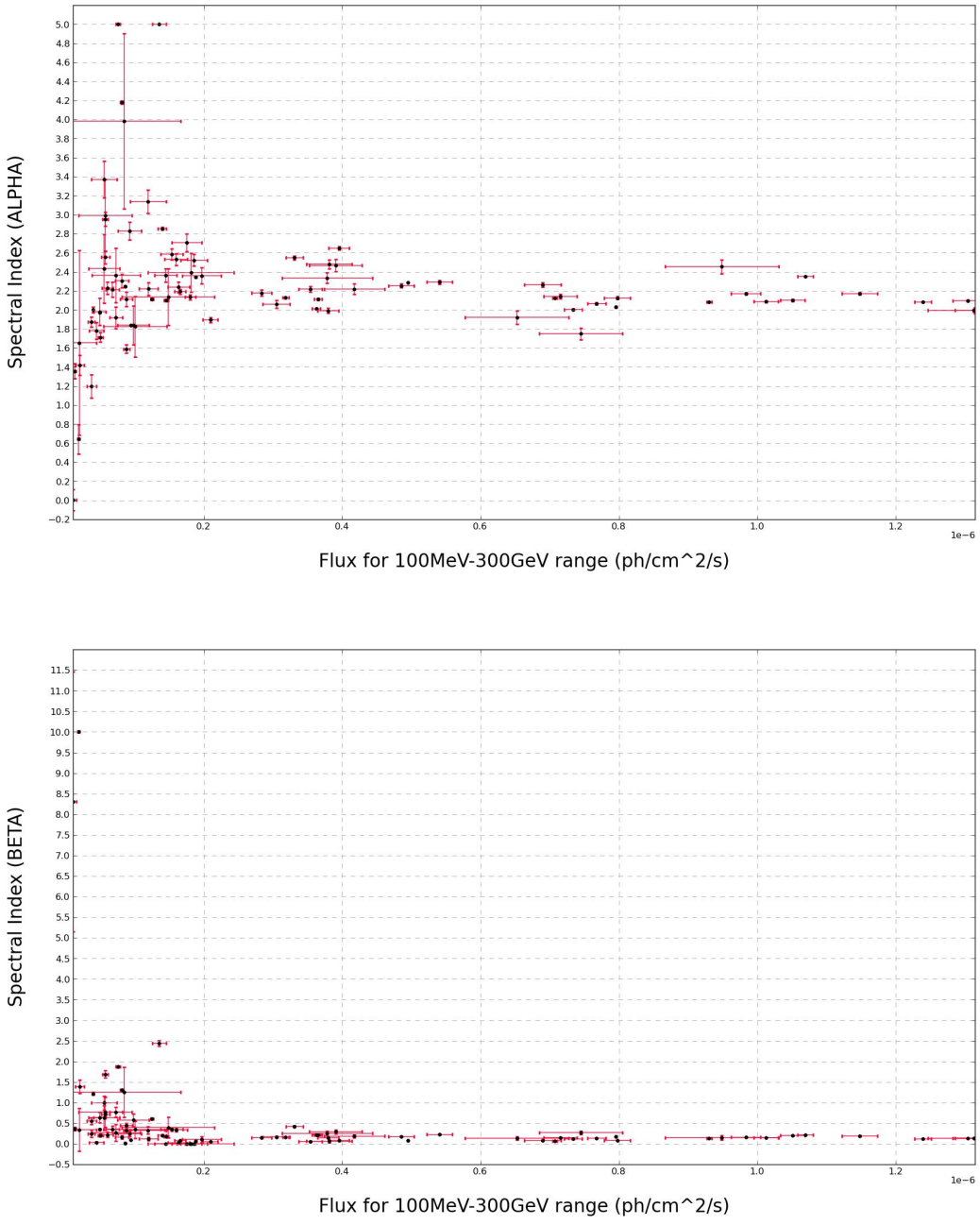

Figure 74: *Spectral indexes versus flux for source PKS1502+106. ABOVE - α vs flux. BELOW - β vs flux. No correlation between flux and spectral index is found. Low flux values present larger error bars possibly due to low statistics in this range, resulting in low TS values (and hence significance) of these events.*

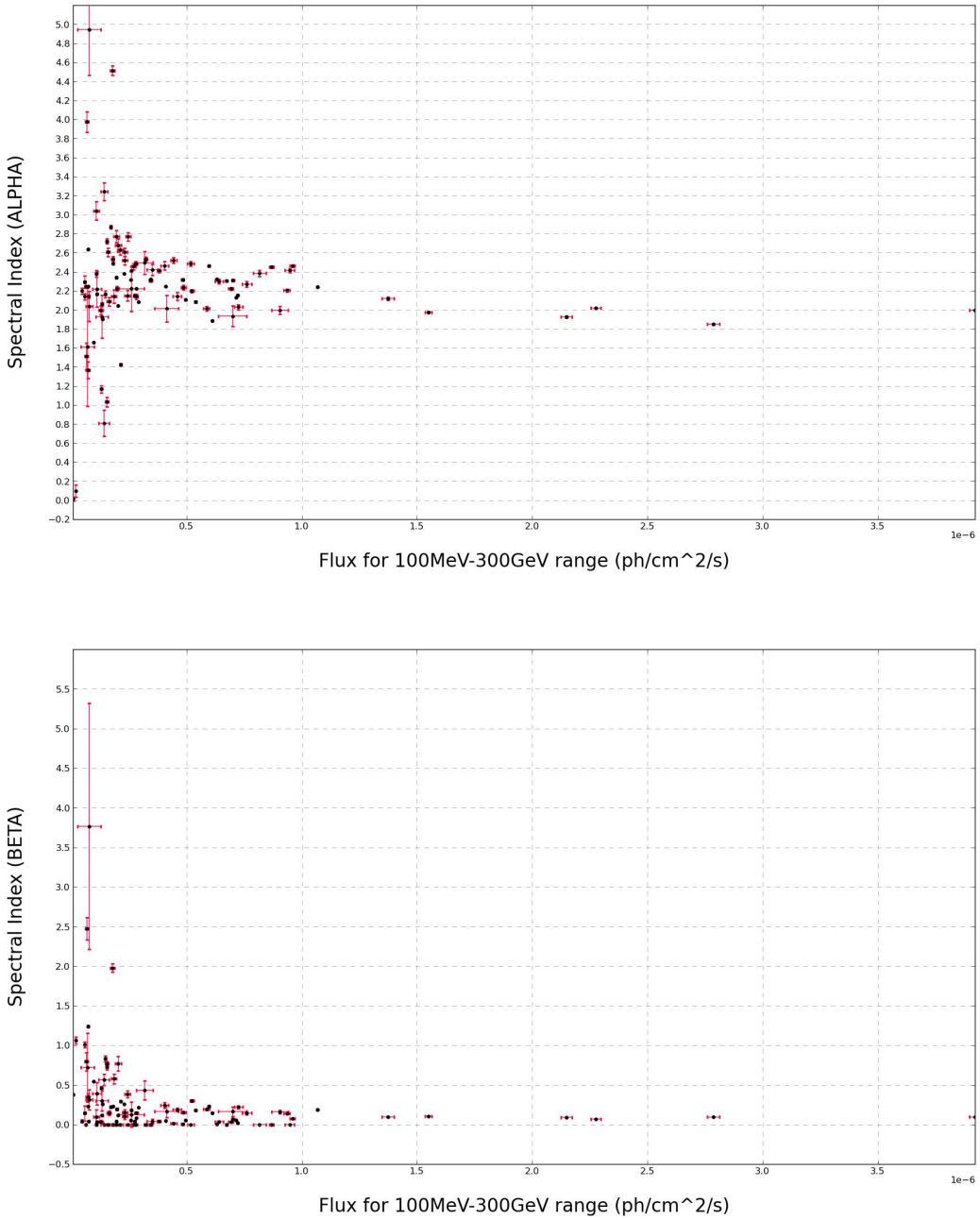

Figure 75: *Spectral indexes versus flux for source 4C+21.35. ABOVE - α vs flux. BELOW - β vs flux. No correlation between flux and spectral index is found. Low flux values present larger error bars possibly due to low statistics in this range, resulting in low TS values (and hence significance) of these events.*

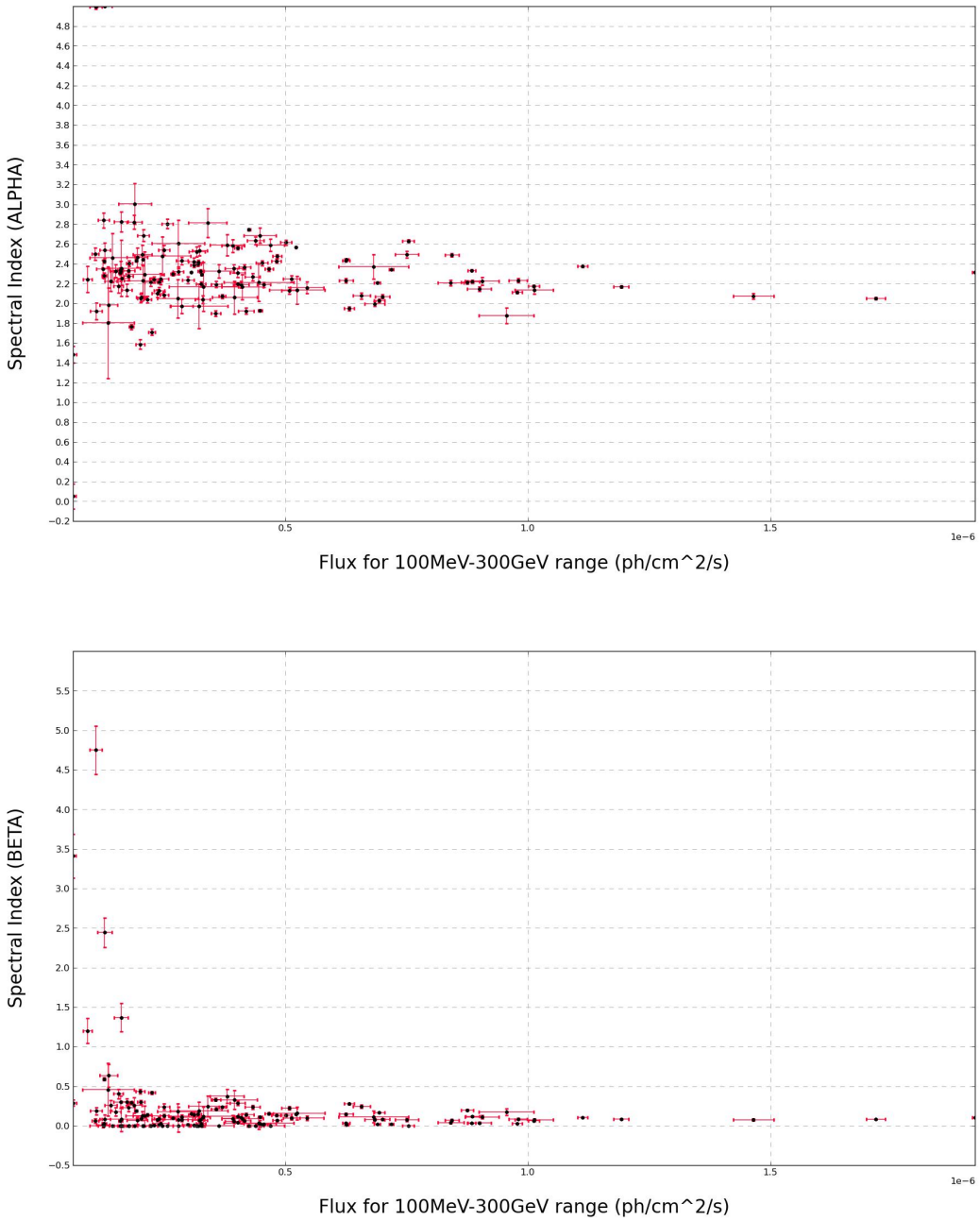

Figure 76: *Spectral indexes versus flux for source 3C279. ABOVE - α vs flux. BELOW - β vs flux. No correlation between flux and spectral index is found. Low flux values present larger error bars possibly due to low statistics in this range, resulting in TS values (and hence significance) of these events. There is a slight tendency of larger β values for lower fluxes, even if there is not an overall correlation.*

After determining the flare epochs for the five sources by identifying the highest peaks in the LCs, a similar analysis to the one in Chapter 5 was performed to end up with the spectrum of the source during its most active period. Data filtering and selection criteria were the same as for the 5-year analysis, and so it was the initial model file. The only difference was that, given the flares are short events when compared to 5 years of data, and that we split the *Fermi* energy range into smaller bins for obtaining the average flux for each of them, an *unbinned* likelihood analysis was more suitable to obtain the spectrum, because the number of events in such short periods of time is not very high.

Each source was modelled following the best fit model obtained for the long-term analysis. Model files were modified following the same steps as in Chapter 5, i.e. taking low TS values out, producing residuals maps to account for any extra source with high TS value (Figures 75-79). As in the long-term analysis, only the residuals map of PKS1510-089 show an extra gamma-ray source that has to be added to the model file. The new source is the same as for the long-term analysis, TXS1530-131.

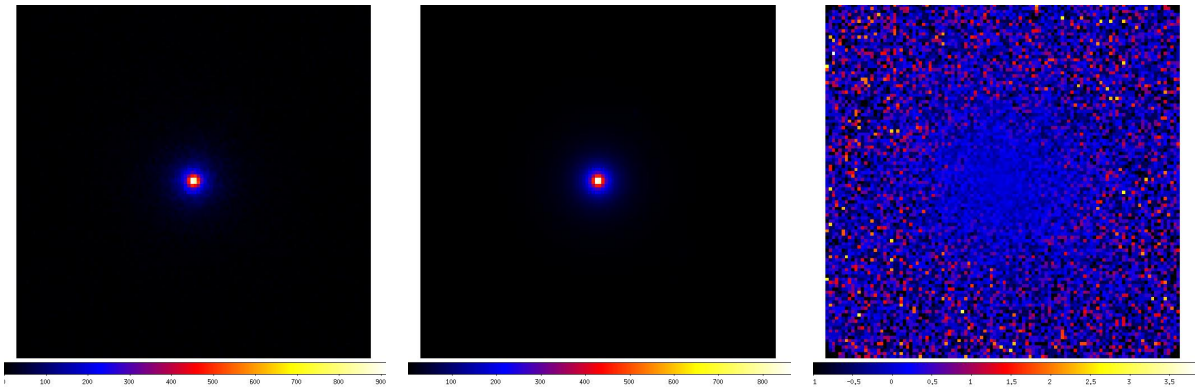

Figure 77: *Source 3C454.3. LEFT - 100 MeV-300 GeV map for the brightest flare. Counts per pixel are shown on the color bar. The image scale is 0.2° per pixel, and the image covers 22° ×22°. CENTER - Model map obtained with the* ***gtmodel*** *Fermi tool for the brightest flare, using the best fit model which for 3C454.3 is a LogParabola. Counts per pixel are shown on the color bar. The image scale is 0.2° per pixel, and the image covers 22° ×22°. RIGHT - Residuals map of the 100 MeV-300 GeV events in units of percentage. The residuals map is produced by (sky map - model map)/(model map). The colour scales for both the sky map and the model map are in units of gamma-ray counts, whereas the residuals maps are in units of percentage. No evidence is visible for new gamma-ray sources.*

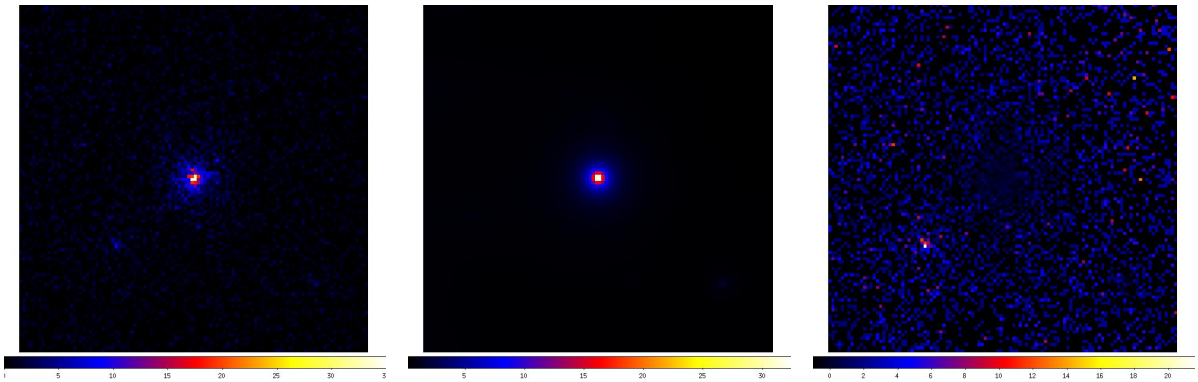

Figure 78: *Source PKS1510-089. LEFT - 100 MeV-300 GeV map for the brightest flare. Counts per pixel are shown on the color bar. The image scale is 0.2° per pixel, and the image covers 22° ×22°. CENTER - Model map obtained with the* ***gtmodel*** *Fermi tool for the brightest flare, using the best fit model which for PKS1510-089 is a BrokenPowerLaw. Counts per pixel are shown on the color bar. The image scale is 0.2° per pixel, and the image covers 22° ×22°. RIGHT - Residuals map of the 100 MeV-300 GeV events in units of percentage. The residuals map is produced by (sky map - model map)/(model map). The colour scales for both the sky map and the model map are in units of gamma-ray counts, whereas the residuals maps are in units of percentage. As for the 5-year long-term analysis, an apparent extra point source is present in the residuals, which corresponds to the same new source from the long-term analysis, TXS 1530-131. Accordingly, the new source is added in the model file.*

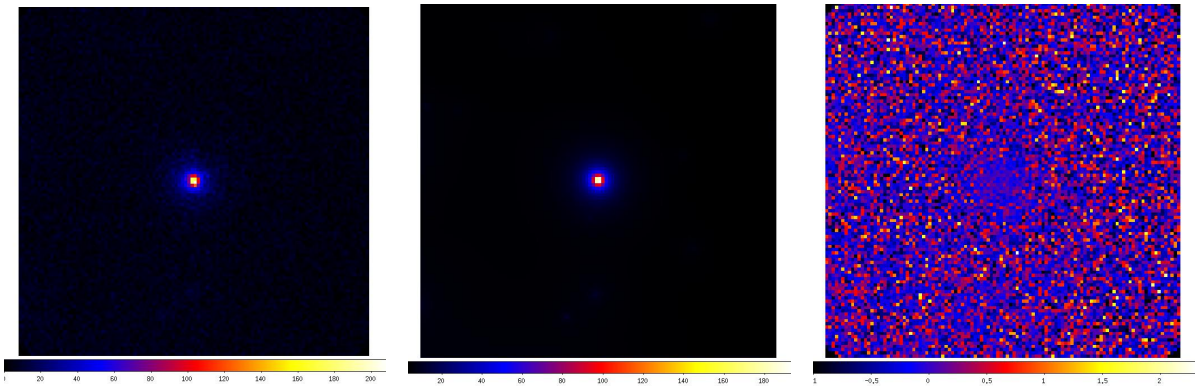

Figure 79: *Source PKS1502+106. LEFT - 100 MeV-300 GeV map for the brightest flare. Counts per pixel are shown on the color bar. The image scale is 0.2° per pixel, and the image covers 22° ×22°. CENTER - Model map obtained with the* ***gtmodel*** *Fermi tool for the brightest flare, using the best fit model which for PKS1502+106 is a LogParabola. Counts per pixel are shown on the color bar. The image scale is 0.2° per pixel, and the image covers 22° ×22°. RIGHT - Residuals map of the 100 MeV-300 GeV events in units of percentage. The residuals map is produced by (sky map - model map)/(model map). The colour scales for both the sky map and the model map are in units of gamma-ray counts, whereas the residuals maps are in units of percentage. No evidence is visible for new gamma-ray sources.*

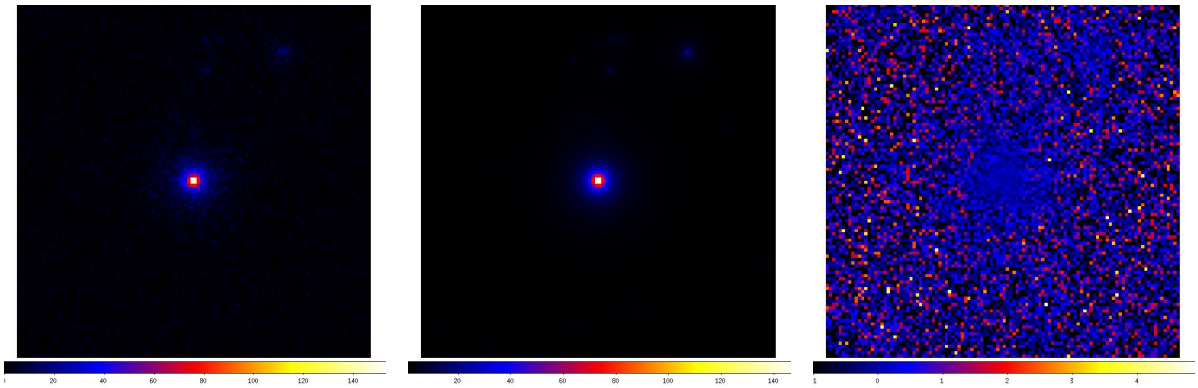

Figure 80: *Source 4C+21.35. LEFT - 100 MeV-300 GeV map for the brightest flare. Counts per pixel are shown on the color bar. The image scale is 0.2° per pixel, and the image covers 22° ×22°. CENTER - Model map obtained with the* ***gtmodel*** *Fermi tool for the brightest flare, using the best fit model which for 4C+21.35 is a LogParabola. Counts per pixel are shown on the color bar. The image scale is 0.2° per pixel, and the image covers 22° ×22°. RIGHT - Residuals map of the 100 MeV-300 GeV events in units of percentage. The residuals map is produced by (sky map - model map)/(model map). The colour scales for both the sky map and the model map are in units of gamma-ray counts, whereas the residuals maps are in units of percentage. No evidence is visible for new gamma-ray sources.*

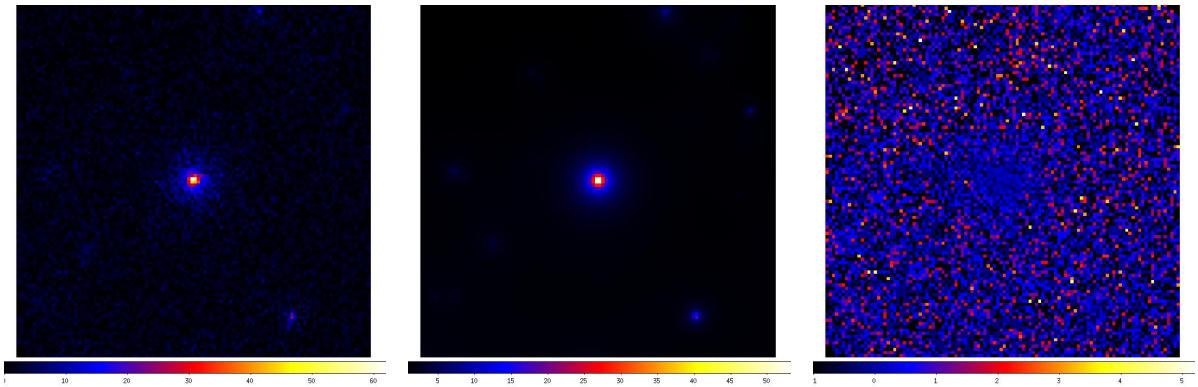

Figure 81: *Source 3C279. LEFT - 100 MeV-300 GeV map for the brightest flare. Counts per pixel are shown on the color bar. The image scale is 0.2° per pixel, and the image covers 22° ×22°. CENTER - Model map obtained with the* ***gtmodel*** *Fermi tool for the brightest flare, using the best fit model which for 3C279 is a LogParabola. Counts per pixel are shown on the color bar. The image scale is 0.2° per pixel, and the image covers 22° ×22°. RIGHT - Residuals map of the 100 MeV-300 GeV events in units of percentage. The residuals map is produced by (sky map - model map)/(model map). The colour scales for both the sky map and the model map are in units of gamma-ray counts, whereas the residuals maps are in units of percentage. No evidence is visible for new gamma-ray sources.*

Again, only the normalization parameters of the sources within 10° are left to be fitted in the likelihood analysis. To get the spectrum, the same 11 bins used for the whole 5-year analysis were applied, and an unbinned likelihood routine was performed for each bin. Fluxes were estimated with upper limits for energy bins with TS$<$ 25 values too.

Once the energy spectra during the flare events were obtained, extrapolated to the CTA energy range and corrected for the EBL absorption, they were contrasted with the PROD1 and PROD2 CTA sensitivity curves (as explained in Chapter 4 Section 5) for 5-hour exposures to determine whether the sources would be visible during bright flares. See the next Sections of this Chapter for the results obtained.

3. Results for flare events

In the following Section the spectra during flare events are presented. The fluxes corrected for EBL absorption are plotted along with the CTA sensitivity curves considered for flare event analysis, that is, the PROD2 DESY sensitivity curve for array layout A and PROD1 DESY sensitivity curve for array layout E, both for a 5-hour exposure (see Chapter 4 Section 5 for more information about PROD1 and PROD2 simulations). There are two main reasons to consider a PROD2 configuration for flare events. On the one hand, flare events are relatively short in time, so the enhanced sensitivity of PROD2 configuration is a key point for detecting the sources. On the other hand, PARIS, IFAE and KB analyses have not been so far implemented for PROD2 configurations of CTA, so there is no information available to consider these analyses.

The qualitative criteria followed for flare events is the same as for the long-term analysis of the sources in Chapter 5: if the spectrum is above the sensitivity curve, the source will be detected by CTA.

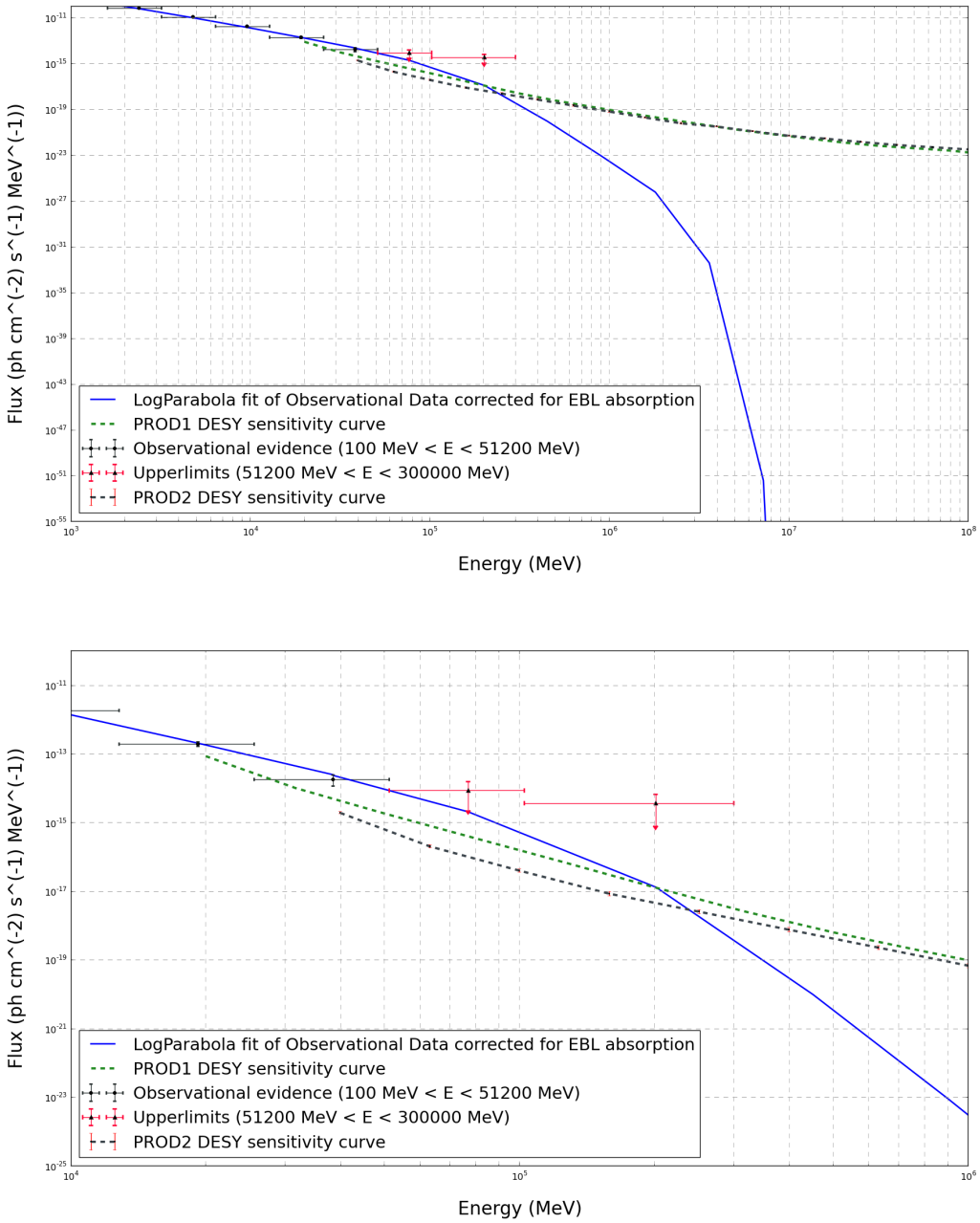

Figure 82: *Plot of the spectrum for the brightest flare of 3C454.3 together with 5-hour PROD1 and PROD2 DESY sensitivity curves. The shape of the spectra during the flare and for the 5-year analysis are quite similar: the EBL absorption reduces the observed flux drastically for energies above 10^5 MeV. The lower plot illustrates that the PROD2 DESY configuration is more sensitive than the PROD1 DESY configuration, even if the latter extends to lower energies. But it is more interesting to obtain a better sensitivity for higher energies, since this is where the difficulty for detecting FSRQs rises. Nonetheless, for the FSRQ 3C454.3, both configurations would enable the detection the source according to this analysis.*

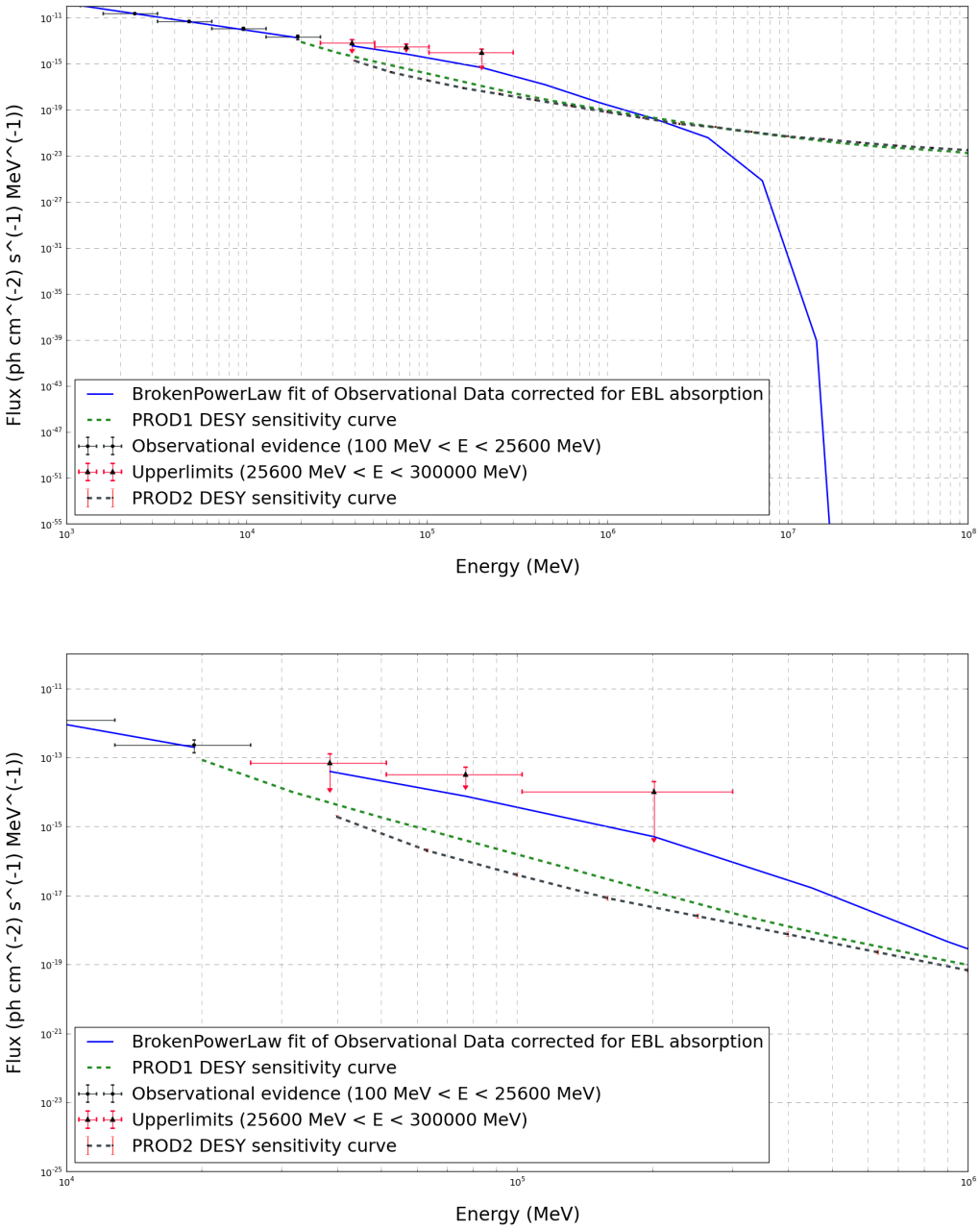

Figure 83: *Plot of the spectrum for the brightest flare of PKS1510-089 together with 5-hour PROD1 and PROD2 DESY sensitivity curves. PKS1510-089 would be detected using both PROD1 and PROD2 configurations and DESY analysis up to higher energies that the rest of the sources, due to a combination of the BrokenPowerLaw shape of the distribution and the brightness of the flare.*

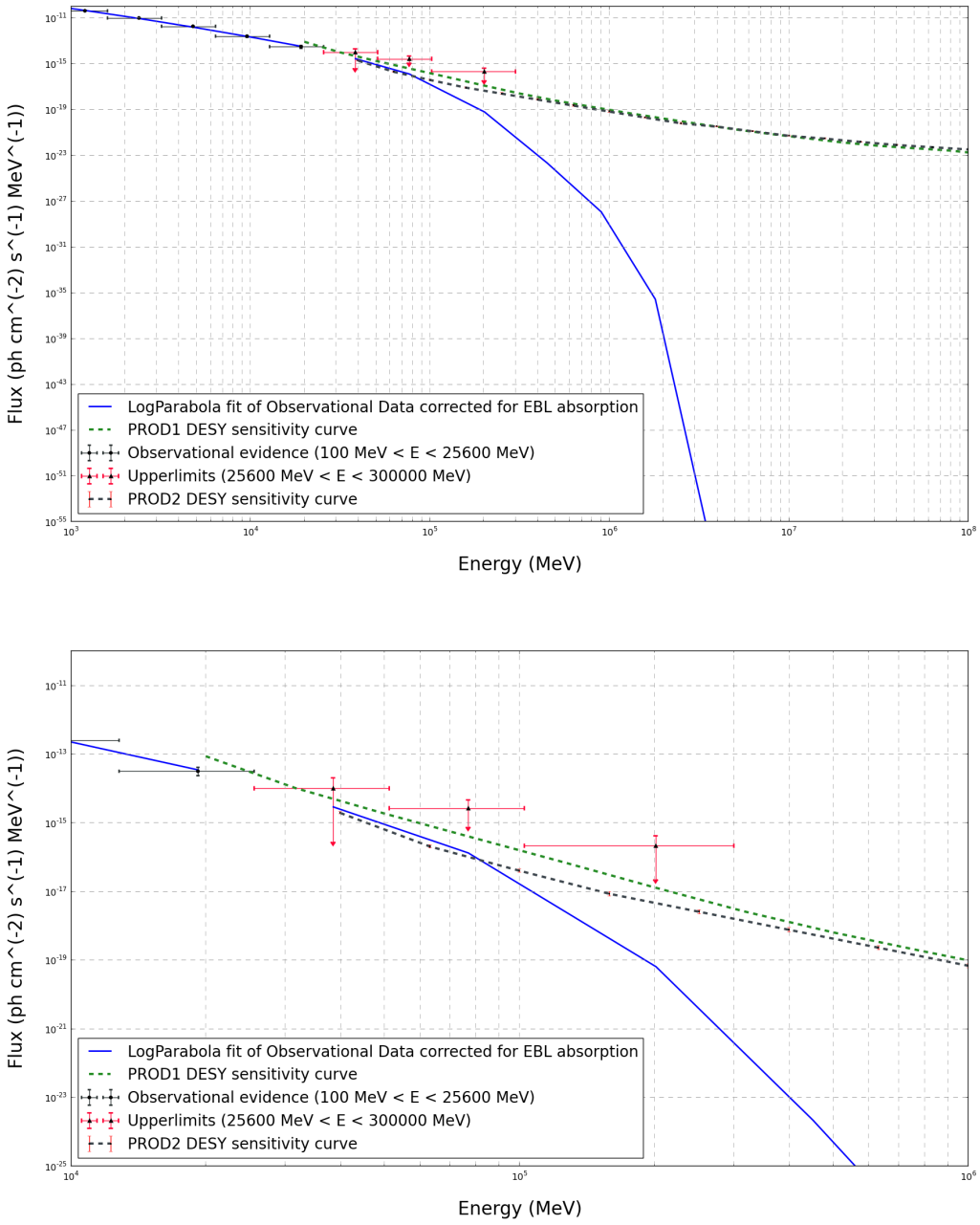

Figure 84: *Plot of the spectrum for the brightest flare of PKS02+106 together with 5-hour PROD1 and PROD2 DESY sensitivity curves. As happened for the long-term analysis, PKS1502+106 would not be detected by PROD1 DESY configuration, even during flaring state. On the other hand, since PROD2 DESY has greater sensitivity, this configuration might stand a chance of detecting it, but as can be seen in the lower plot, the spectrum is really close to the sensitivity curve.*

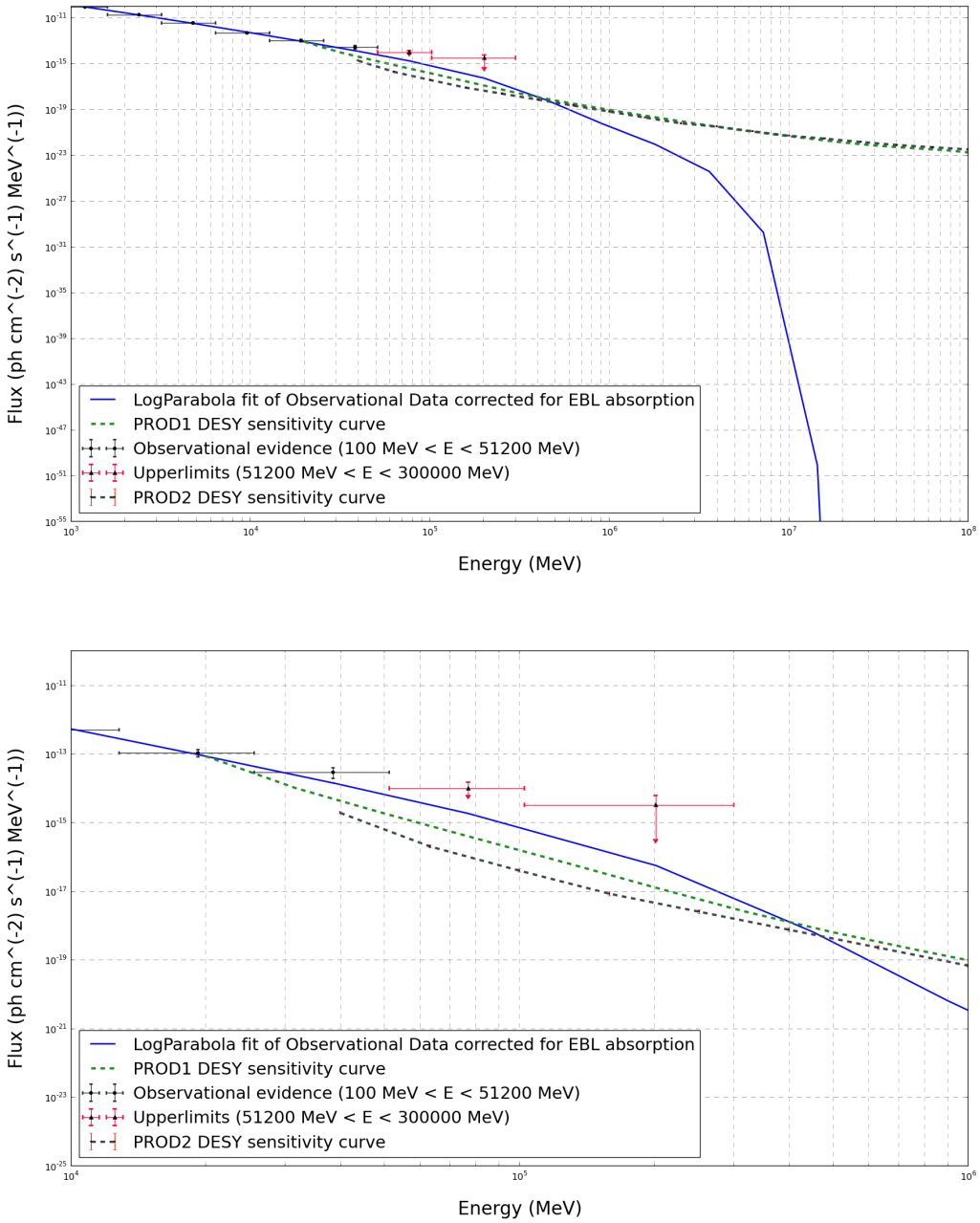

Figure 85: *Plot of the spectrum for the brightest flare of 4C+21.35 together with 5-hour PROD1 and PROD2 DESY sensitivity curves. For the 4th source considered for flare analysis, the two configurations considered would enable CTA to observe this FSRQ.*

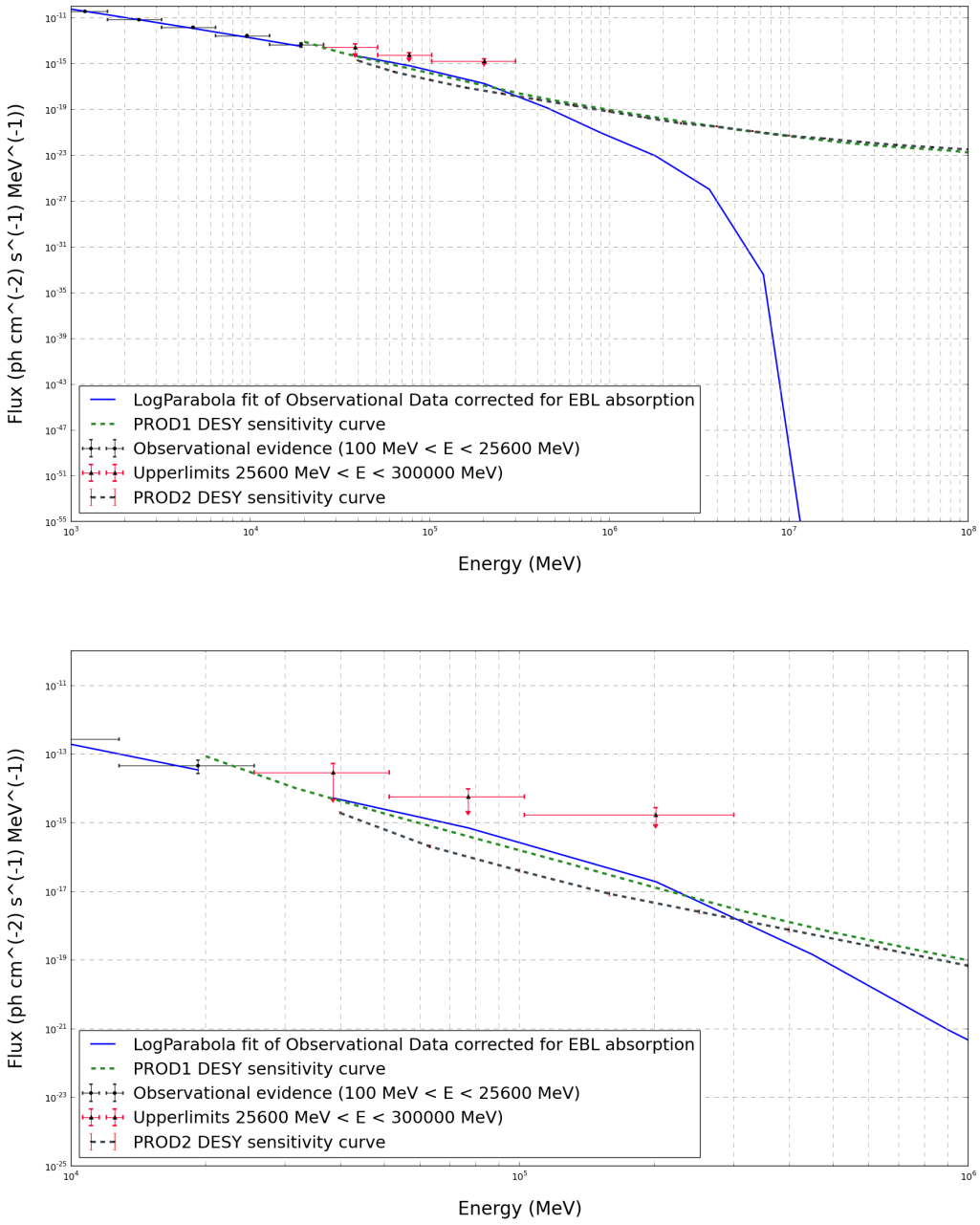

Figure 86: *Plot of the spectrum for the brightest flare of 3C279 together with 5-hour PROD1 and PROD2 DESY sensitivity curves. Likewise the rest of the sources analysed during flare intervals, 3C79 would be observed by both PROD1 and PROD2 DESY configurations.*

Although the flares are much shorter compared to the period of time for which the 5-year average flux analysis was performed, both sets of spectra resemble one another. A quick look to the spectra shows the flux attenuation is obvious for flare events too, as it was for the whole 5-year period analysis. Of course, the same arguments regarding extrinsic and intrinsic attenuation mechanisms apply to flare events and 5-year analysis.

Flare epochs are so active and bright that sources that were not detected by a certain CTA configuration for the 5-year average flux analysis might be detected when they enter a flaring state. In fact, only PKS1510-089 out of the 9 FSRQs was detected by the implementation of PROD1 DESY configuration for the 5-year analysis. For flaring intervals, though, all the FSRQs with the exception of PKS1502+106, the source with highest redshift, would be detected by the exactly the same PROD1 DESY configuration.

Of the sub-sample considered for flare epoch analysis, three FSRQs had already been detected during flare epochs by ground-based gamma-ray observatories: PKS1510-089, 4C+21.35 and 3C279 (Table 2). They would also be detected by both PROD1 and PROD2 DESY CTA configurations. A very promising result is that 3C454.3 would also be detected during flare state by both PROD1 and PROD2 CTA configurations, owing to the enhanced sensitivity of CTA. 3C454.3, unlike the former three, has not yet been detected in the VHE range. As mentioned in Chapter 2, FSRQs are hard to detect in the VHE regime not only due to the EBL absorption the photons suffer from in the intergalactic medium, but also due to internal absorption mechanisms that prevent the gamma-rays from going further than the AGN itself. To cast light on this issue, multi wavelength observations of the optical spectral lines from the inner region of the Lyman Alpha (Ly-α) forest could be useful (Poutanen and Stern, 2010; Poutanen and Stern, 2014).

What is more, the PROD2 DESY configuration, with its enhanced sensitivity, would be able to detect all of the sources in flare epochs. This is quite positive, since the most sensitive PARIS configuration - able to detect 8 out of 9 FSRQs - is not taken into account in the PROD2 simulations (at least so far).

Something that stands out when closely observing the spectra and comparing them to one another, is that the spectrum of PKS1510-089 is a bit of an outlier. Either due to this source being better fit with a BrokenPowerlaw, or because the flare analysed was quite bright, this source would be detected by both PROD1 and PROD2 DESY up to higher energies than the rest of the FSRQs. Again, this is quite reassuring for the CTA configurations being considered, since it means the designs are on the right path for a very useful implementation of the telescopes.

Table 10: Qualitative source detection during flare events

Source	DESY PROD1	DESY PROD2
3C454.3	✓	✓
PKS1510-089	✓	✓
PKS1502+106	×	✓
4C+21.35	✓	✓
3C279	✓	✓

FSRQs considered during flare events, and whether a source would be observed during flares considering the PROD1 DESY curve for 5h exposure and layout E and PROD2 DESY for 5h exposure and array layout A.

As in Chapter 5, apart from qualitative determination of CTA detection, a quantitative determination method is required for flare events. Likewise for the qualitative criteria, quantitative criteria followed for flare events is the same as for the 5-year average flux analysis of the sources: if the integrated value of the spectrum is greater than the integrated value of the sensitivity curve, the source will be detected by CTA.

Table 11: Integrated flux values for sources during flare events

Source	INTEGRATED FLUX (ph/cm^2/s/MeV)
3C454.3	0.634×10^{-09}
PKS1510-089	1.438×10^{-09}
PKS1502+106	0.697×10^{-10}
4C+21.35	4.303×10^{-10}
3C279	1.589×10^{-10}
Sensitivity Curve	INTEGRATED FLUX (ph/cm^2/s/MeV)
DESY PROD1	6.217×10^{-11}
DESY PROD2	4.501×10^{-11}

Table comprising the integrated values for the fluxes of the sources in flare events, along with PROD1 DESY and PROD2 DESY sensitivity curves.

In the case of flare events, the energy boundaries considered for integration are different from the 5-year analysis boundaries, since the minimum energy available for the DESY PROD2 sensitivity curve is higher than for the PROD1 DESY configuration (39810 MeV for PROD2 and 19952 MeV for PROD1). The maximum boundary was again set by the maximum energy for which the EBL corrected flux could be calculated (i.e. 72 TeV). These limits have been applied to the integration of both the CTA curves and the spectrum of the sources, enabling a sensible comparison between them to be made.

The results obtained from flux integration are consistent with the results from the qualitative analysis. As we have mentioned before, the only source that would not be detected in flare state using the PROD1 DESY configuration is PKS1502+106, and the results in Table 10 show that the integrated flux from this source is the only one that lies below the integrated fluxes for the sensitivity curves.

It can be also noticed how much brighter are the flares of 3C454.3 and PKS1510-089, whose flux is one order of magnitude larger than that of the rest of the sources. The LCs of both sources show that the flare of 3C454.3 reaches almost 1.7×10^{-5} ph/cm^2/s/MeV, while PKS1510-089 lies one order of magnitude below, around 4.1×10^{-6} ph/cm^2/s/MeV. Hence, one would expect the integrated flux of 3C454.3 to be larger than the integrated flux of PKS1510-089. Quite unexpectedly, though, the integrated flux of PKS1510-089 is larger than the integrated flux of 3C454.3, 1.438×10^{-09} ph/cm^2/s/MeV versus 0.634×10^{-09} ph/cm^2/s/MeV.

A possible reason for this is that the integrated fluxes have been calculated only for the energy range in which the spectra of the sources and the sensitivity curves of CTA overlap (39810 MeV- 7.2 TeV), in order to enable a sensible comparison between the fluxes. If we contrast the two spectra of these sources during the considered flare events in this integration energy range, we can see that due to the nature of the BrokenPowerLaw spectrum, PKS1510-089 is likely to be detected for a larger energy range than 3C54.3 with CTA (the spectrum of PKS1510-089 lies above the sensitivity curves for a larger energy), since the LogParabola spectrum of 3C454.3 is attenuated more rapidly. Hence, the integrated flux of PKS1510-089 over the energy range considered for integration could be larger than the flux of 3C454.3, even if the overall flare was brighter for the latter source.

7. OVERVIEW AND FINAL REMARKS

In this work, 9 of the brightest *Fermi* detected FSRQs have been analysed in order to cast light on whether the future ground-based gamma-ray observatory CTA would be able to detect these sources, based on the average flux from 5 years of existing *Fermi* data. Likewise, the brightest five sources from the chosen 9 FSRQs (i.e. the first five FSRQs) were analysed for epochs in which they entered their brightest flaring state. Flaring epochs were determined based on the light curves of the 5 year period, were the flare events appear as high peaks of enhanced flux levels.

Spectra were produced for both the long-term and the short-term analysis, via binned likelihood analysis of the whole 5 years of *Fermi* data for the former case, and via unbinned likelihood analysis of the same *Fermi* data narrowed to the flaring intervals for the latter. The fluxes obtained from the likelihood analysis of the *Fermi* data were then fitted with the best fit model according to the AIC, and these best fit functions were extrapolated to the CTA energy range, as well as corrected for EBL absorption according to the EBL model proposed by Franceschini et al. in 2008.

1. Long-term analysis

For the long-term analysis, the obtained spectra were compared with 4 different configurations corresponding to different analyses of PROD1 simulations of 50 hours of exposure of array layout E, namely PARIS, IFAE, KB and DESY.

The detection of a source in consonance with our analysis was determined in two ways, both for 5-year average flux analysis and flare state analysis. First, the relative positions of spectra and CTA sensitivity curves were compared, defining a positive detection for the cases when the sensitivity curve lies below the spectrum of the source. Secondly, both the fluxes obtained from the analysis and the CTA sensitivity curves were integrated over the energy range in which they overlap in order to enable us to make a meaningful quantitative comparison of the integrated fluxes. Again, if the integrated flux of the source is larger than the integrated flux of a certain sensitivity curve, the analysis approach concerned would detect the source according to the analysis I have performed.

From Figures 51-59, plots of the spectra and CTA sensitivity curves, it can be seen that the sensitivity curve corresponding to PROD1 PARIS configuration lies a bit below the rest of the PROD1 sensitivity curves for the lowest energies in the CTA range. This means that, according to our analysis, 8 out of the 9 FSRQs from our sample would be detected by the PROD1 PARIS configuration for our 5-year observation period. On the other hand, the PROD1 DESY configuration sensitivity curve, whose sensitivity threshold is the highest, results in a lack of detection even of the brightest FSRQs. The same statement is applicable to IFAE and KB curves, which are in fact very similar to the DESY one, and are not likely to detect our FSRQs in the 5-year average flux analysis.

Something to note is that the only source whose best fit spectral model is a BrokenPowerLaw instead of a LogParabola, PKS1510-089, is the only source that would be detected by *all* the PROD1 sensitivity curves for our 5-year analysis. The decrease in flux is more *gradual* for PKS1510-089 than for the rest of the sources, due to the nature of the BrokenPowerLaw spectrum. While for the *Fermi* energy range there is not a great difference between the shape of both distributions, this changes for the CTA energy range, and the LogParabola function becomes fainter more rapidly and at lower energies than the BrokenPowerLaw. This tendency can be appreciated when comparing the spectrum of PKS1510-089 with the spectra of the rest of the sources for 5-year average flux analysis, which are best fitted by a LogParabola.

The attenuation of the flux that is observed for all the FSRQs could be due to the EBL absorption we have taken into account in the spectra of the sources. Sources with larger redshifts are more likely to suffer from larger attenuation due to the EBL, since the gamma-ray photons have to travel larger distances until they reach the detector. This could explain the fact that PKS1502+106, the 3rd brightest of our sources, is attenuated more rapidly than the rest of the sources, since this source is the one with the largest redshift (Table 2). This trend could also be applied to sources 4C+21.35, 3C279, PKS0454-234, PKS0727-11 and B21520+31, which present increasingly larger redshift values, and hence, become fainter increasingly rapidly. Note that all these sources are modelled as LogParabolas, whose curvature is determined by the β spectral index in Eq. 13. Larger curvature results in more rapid attenuation of the flux, and therefore, fainter fluxes. To cast light on the existence of a relationship between the curvature and the flux, a plot of these two parameters was created (Figure 60), showing no clear correlation for both quantities. Interestingly, though, Figure 76 shows that for the source 3C279, there is a slight tendency of larger β values for lower fluxes, even if there is not an overall correlation.

However, the attenuation could be due to some intrinsic rather than extrinsic absorption mechanisms. The previous paragraph noted that the trend of greater attenuation is observed for sources modelled as LogParabolas. In fact, LogParabola spectra are thought to be a reflection of some internal absorption mechanism happening in the inner region of the FSRQ. Such a mechanism would mean that gamma-rays are absorbed before they can escape the clouds that surround the AGN, resulting in a cut-off in the gamma-ray spectrum that is observed in LogPararabola distributions. This points

towards gamma-rays being created close to the BLR of the AGN. Since the β factor controls the curvature in the LogParabola spectral function, and larger curvature means larger attenuation, one would expect large β values for sources with a brighter BLR that absorbs more gamma-ray photons. For the sources considered in this work, 4C+21.35 and 3C279 show lower β spectral indexes than the majority of the FSRQs in our sample. This could be the reason why these two sources have been detected in the VHE regime: fewer VHE gamma-ray photons are absorbed, and hence it is easier to detect them.

On the other hand, $\beta \approx 0$ would turn the LogParabola distribution into a PowerLaw spectrum, which does not have any cut-off feature. PowerLaw distributions would reflect gamma-ray emission mechanisms located further away from the SMBH, and hence not being absorbed in the BLR, which results in an absence of spectral cut-offs.

In addition, large curvature could also mean that the electrons from which the gamma-rays were created are described by a distribution with large curvature. Large curvatures can also be caused by poor statistics in the VHE regime, which might be a caveat in our analysis since we have extrapolated *Fermi*-LAT data to higher energies. With its improved sensitivity, CTA will be able to detect more gamma-ray events in the VHE range, enabling the production of much more accurate spectra that will cast light on the features behind the behaviour of the sources.

To try to discriminate between an EBL origin and an intrinsic absorption origin of the attenuation observed for all the FSRQs in our sample, the redshifts of the sources were plotted against the β spectral indexes (Figure 61). If a correlation between the redshift and β exists, this would point towards an EBL origin, since larger redshifts would be related to larger β values, as a the photons have to travel longer distances through the EBL, and hence, suffer from more absorption. No clear correlation is found for all the FSRQs. However, some sources (4C+21.35, 3C279, 3C454.3 and PKS1502+106) actually follow a slight tendency of larger β values for larger redshifts. This suggests that the EBL is not the only absorption mechanism for these objects, and that internal absorption is also significant.

After qualitatively determining whether a source would be detected, we integrated the flux coming from the source across the *Fermi* energy range, the corrected flux across the CTA energy range and the sensitivity curves across their respective energy ranges. This way, we get a number that identifies the *average* integrated value in order to compare one to another. The minimum energy boundary for integrating the fluxes was the minimum energy value for which the CTA sensitivity curves could be calculated (i.e 19954 MeV), while the maximum boundary was set by the maximum energy for which the EBL corrected flux could be calculated (i.e. 7.2 TeV). These limits have been applied to both the CTA curves and the spectra of the sources, enabling a sensible comparison between them to be made.

The results obtained from integration were consistent to the results obtained from the more qualitative detection criteria. Again, the PROD1 PARIS configuration is likely to detect all the FSRQs, whereas the remaining 3 sensitivity curves lie above the inte-

grated fluxes of the sources for the 5-year analysis.

Moreover, PKS1510-089 shows the highest integrated flux, even greater than the flux for the brightest FSRQ 3C454.3 (4.716×10^{-10} ph/cm^2/s/MeV for PKS1510-089, 3.407×10^{-10} ph/cm^2/s/MeV for 3C454.3). On the other hand, the lowest flux corresponds to PKS1502+106 (1.001×10^{-10} ph/cm^2/s/MeV), due to the large attenuation that this source presents.

After performing the 5-year analysis and considering the results obtained, one thing is clear: the analysis that is implemented for the PROD1 configuration of CTA is the key point for a positive or negative detection of a certain source. From the point of view of the present work, the PARIS analysis is outstandingly better for detecting as many FSRQs as possible, whereas the DESY analysis would not enable us to see them in the 5-year average flux analysis. It is paramount that the different analysis techniques are closely examined in order to determine which is the most sensible one, since it is such a critical aspect.

2. Flaring state analysis

For flare event analysis, 5 hour exposure sensitivity curves from both PROD1 and PROD2 simulations were considered: PROD1 DESY for array layout E (same as for long-term analysis) and PROD2 DESY for array layout A, the only analysis available for PROD2 at the time of writing.

So far as the spectra are concerned, both 5-year and flaring state spectra show similar shape and features, even though the flares are much shorter compared to the period of time for which the long-term analysis was performed. The flux attenuation is also remarkable for flare events, as it was for the whole 5-year period analysis, hampering the detection of the sources in the VHE range. The same arguments regarding extrinsic and intrinsic origin of attenuation mechanisms apply to flare events and long-term analysis.

The analysis of the sources during flare events proves that the source not being bright enough to be detected on the basis of its 5-year average flux does not necessarily mean it would not be detected when the FSRQ enters a flaring epoch. From the 5 FSRQs analysed during flares, only PKS1510-089 was detected by the implementation of PROD1 DESY configuration for the 5-year analysis. For flaring intervals, though, all FSRQs except PKS1502+106, the source with highest redshift and second highest β spectral index, would be detected by the exactly the same PROD1 DESY configuration. This again is a reflection of the enhanced sensitivity that will be reached with the implementation of CTA.

On the other hand, the PROD2 DESY configuration, with its enhanced sensitivity,

would be able to detect all of the sources in flare epochs. This is quite positive, since the most sensitive PARIS configuration - able to detect 8 out of 9 FSRQs, is not taken into account in the PROD2 simulations (at least so far).

Of the sub-sample considered for flare epoch analysis, three FSRQs had already been detected during flare epochs: PKS1510-089, 4C+21.35 and 3C279 (Table 2) by ground-based gamma-ray observatories. They would also be detected by both PROD1 and PROD2 DESY CTA configurations. A very promising result is that 3C454.3 would also be detected during flare state by both PROD1 and PROD2 CTA configurations, owing to the enhanced sensitivity of CTA. 3C454.3, unlike the former three, has not yet been detected in the VHE range.

Something that stands out when closely observing the spectra for flares and comparing them to one another, is that the spectrum of PKS1510-089 is a bit of an outlier. Either due to this source being better fit with a BrokenPowerlaw (and hence not displaying a curvature as large as a LogParabola) or either because the flare analysed was quite bright, this source would be detected using both the PROD1 and PROD2 DESY analyses up to higher energies than the rest of the FSRQs. Again, this is reassuring, since it means the CTA designs simulations being considered are on the right path for a productive implementation of the telescopes.

The flares of 3C454.3 and PKS1510-089 are the brightest of the sample, their integrated flux being one order of magnitude larger than that of the rest of the sources. Quite unexpectedly, the integrated flux of PKS1510-089 is larger than the integrated flux of 3C454.3 (1.438×10^{-09} ph/cm^2/s/MeV versus 0.634×10^{-09} ph/cm^2/s/MeV.) although the LC of 3C454.3 shows a flare that reaches almost 1.7×10^{-5} ph/cm^2/s/MeV, while the flare of PKS1510-089 lies one order of magnitude below according to its LC, around 4.1×10^{-6} ph/cm^2/s/MeV. Hence, one would expect the integrated flux of 3C454.3 to be larger than the integrated flux of PKS1510-089.

The reason for this is that the integrated fluxes have been calculated only for the energy range in which the spectra of the sources and the sensitivity curves of CTA overlap ($\approx$ 40 GeV- 7.2 TeV), in order to enable a sensible comparison between the fluxes. If we contrast the two spectra of these sources during the considered flare events in this integration energy range, we can see that due to the nature of the BrokenPowerLaw spectrum, PKS1510-089 is likely to be detected for a larger energy range than 3C54.3 with CTA (the spectrum of PKS1510-089 lies above the sensitivity curves for a larger energy span), since the LogParabola spectrum of 3C454.3 is attenuated more rapidly. Hence, the integrated flux of PKS1510-089 over the energy range considered for integration could be larger than the flux of 3C454.3, even if the overall flare was brighter in the case of the latter source.

As for the whole 5-year analysis, the results obtained from flux integration for flare events are consistent with the results from the qualitative analysis. As mentioned before, the only source that would not be detected in flare state by PROD1 DESY configuration is PKS1502+106, and the results in Table 10 show that the integrated flux from this

source is the only one that lies below the integrated fluxes for the sensitivity curves. The fluxes from the rest of the sources are one order or two orders of magnitude larger than the sensitivity curves. The lower flux for the flare epoch of PKS1502+106 does not necessarily mean that it was fainter. As we have mentioned before, this could be owing to how distant this source is, and also due to a large internal absorption of the gamma-rays originated in the inner region of the FSRQ, both resulting in fewer photons reaching the detector. Anyhow, there are really good chances of detecting all the sources considered in this work during flare epochs.

3. General comments

An issue that can be inferred from our analysis, and is observed in both long-term analysis and flare analysis, is that the detection of the source mainly depends on *the implemented CTA configuration*. Since CTA is still in its preparatory phase, our results are by no means absolute, and the final detection of the sources considered throughout this work will depend in what CTA layout is finally built. However, it is important that we understand which is the best analysis to be implemented, since results and detection change dramatically with the choice of a certain CTA analysis for the same production configuration of CTA.

It is also necessary to take into account the possible caveats in our analysis. For instance, we have extrapolated flux values obtained from likelihood analysis of *Fermi* data to CTA energies. Given that the sample of data that was extrapolated - the flux values from the likelihood analysis - was a rather small sample (11 energy bins), this might become a limitation for obtaining accurate extrapolated values.

Another caveat could be the best fit model of the spectrum of each source. For this work we have been consistent with the AIC, but as can be seen in Table 4, there is not much difference between the best fit model and the model with the next minimum AIC value. It could be worth it, then, to redo the analysis and see how things change for the model with the second minimum AIC value, specially having a look to the residuals maps obtained to see which model best fits the *Fermi* data of the corresponding source.

Likewise, the choice of a certain EBL model restrains the results to the features considered by the model. The model proposed by Franceschini et al. in 2008 was chosen due to the simplicity with which the optical depth value could be obtained for our energy range of interest. Nonetheless, it would be very interesting to compare the results from this work with those obtained with the implementation of a different EBL model.

Repeating the analysis with data from other gamma-ray telescope, such as HESS, would be really helpful to see whether the data from a space-based telescope and a ground-based telescope drive us to divergent conclusions. Predictions made with HESS

data, being a ground-based observatory, might be very clarifying for the future implementations of CTA.

CTA will also enable us to produce much more accurate spectra, which will be decisive if we are to better understand both the emission and absorption mechanisms of gamma-rays. The cause of the absorption of gamma-rays has been one of the key points of this work: initially we only considered the possible absorption of the EBL, but when analysing the results obtained, it was evident that other absorption mechanisms, such as the internal gamma absorption within the inner region of the AGN, have great impact in the spectra of the sources. The next generation ground-based observatory will help us to cast light on such features, and hopefully we will be able to detect more FSRQs that will help us to better constrain the behaviour and characteristics of these interesting type of AGN.

APPENDICES

A. Very Long Baseline Interferometry

When two waves with the same frequency are combined, the resulting wave is determined by the phase difference in the initial waves. In an interferometer, the waves are superimposed in order to get information about them.

The Very Long Baseline Interferometry (VLBI) is a type of interferometry used in radio astronomy. A signal from an astronomical source is collected by multiple telescopes on Earth. After the collection, the distance between the radio telescopes is calculated using the time differences in the arrival of the signal to different telescopes.

Each antenna of the array stores information about the arrival time of the signal. Later, data from all telescopes is correlated and contrasted to produce the final image of the triggering event.

VLBI allows the distance between telescopes to be much greater than with conventional interferometers, which have to be physically linked to each other.

The result of using many telescopes to gather information about the signal is that the angular resolution of a telescope of equal size to the maximum separation between the telescopes is achieved. Nonetheless, an array of some telescopes will not receive as many photon events as a telescope of that diameter would. Hence, astronomical interferometers are most useful to get information about the brightest astronomical objects.

An example of VLBI is the *Very Large Baseline Array*, (VLBA). The VLBA consists of 10 different 25 meter telescopes working together in the longest VLBI system in the world. From Hawaii to New Hampshire and the Virgin Islands, the VLBA spands for about 8000 km, and is used for radio observations at wavelengths from 3 mm to 28 cm ($\nu \approx 0.3$ GHz to 100 GHz.)

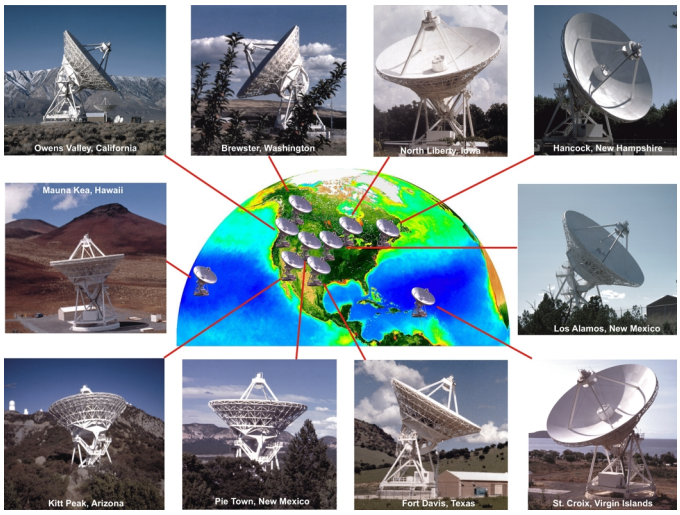

Figure 87: *Location of the different telescopes composing the VLBA.*

B. The Instrument Response Function (IRF)

The IRF is one of the most important *Fermi tools*: it gives the parametrized representation of instrument performance. For data analysis purposes, the LAT assumes the IRFs can be factorized into three parts:

- *Effective Area*, $A_{\rm eff}(E, \hat{v}, s)$, the product of the cross-sectional geometrical collection area, gamma-ray conversion probability, and the efficiency of a given event section (denoted by s) for a gamma-ray with energy E and direction $\hat{v}$ in the LAT frame.

- *Point-spread Function* (PSF), $P(\hat{v}'; E, \hat{v}, s)$, the probability density to reconstruct an incident direction $\hat{v}'$ for a gamma-ray with $(E, \hat{v})$ in the event selection s.

- *Energy Dispersion*, $D(E'; E, \hat{v}, s)$, the probability density to measure an event energy E' for a gamma-ray with $(E, \hat{v})$ in the event selection s.

Given a distribution of gamma-rays $S(E, \hat{p})$, with $\hat{p}$ referring to the celestial directions of the gamma-rays, the predicted distribution of observed gamma-rays $M(E', \hat{p}', s)$ can be predicted by using the IRFs:

$$M(E', \hat{p}', s) = \int\int\int S(E, \hat{p}) A_{\rm eff}(E, \hat{v}(t; \hat{p}), s) \times P(\hat{v}'(t; \hat{p}'); E, \hat{v}(t; \hat{p}'), s)\, D(E'; E, \hat{v}(t; \hat{p}), s)\, {\rm d}E\, {\rm d}\omega\, {\rm d}t \tag{27}$$

References

[1] Abdo et al., 2010a, *'Fermi Large Area Telescope View of the Core of the Radio Galaxy Centaurus A'*, ApJ, **719**, 1433

[2] Abdo et al., 2010b, *'Suzaku Observations of Luminous Quasars: Revealing the Nature of High-energy Blazar Emission in Low-level Activity States'*, ApJ, **716**, 835

[3] Abramowski et al., 2014, *'Flux upper limits for 47 AGN observed with HESS in 2004-2011'*, A&A, **564**, A9

[4] Acciari et al., 2008, *'VERITAS Discovery of >200 GeV Gamma-Ray Emission from the Intermediate-Frequency-Peaked BL Lacertae Object W Comae'*, ApJL, **684**, L73

[5] Aharonian et al. 2006, *'A low level of extragalactic background light as revealed by gamma-rays from blazars'*, Nature, **440**, 1018

[6] Akaike, 1974, *'A new look at the statistical model identification'*, IEEE, Transactions on Automatic Control, **19**

[7] Atwood et al., 2009, *'The Large Area Telescope on the Fermi Gamma-Ray Space Telescope Mission'*, ApJ, **697**, 1071

[8] Baade, 1956, *'Polarization in the jet of Messier 87'*, ApJ, **123**, 550

[9] Baade and Minkowski, 1954, *'Identification of the Radio Sources in Cassiopeia, Cygnus A, and Puppis A'*, ApJL, **119**, 206

[10] Barnacka et al. 2013, *'PKS 1510-089 - a rare example of a flat spectrum radio quasar with very high energy emission'*, A&A, **567**

[11] Barnacka et al., 2014, *'Strong gravitational lensing as a tool to investigate the structure of jets at high energies'*, ApJ, **788**, 139

[12] Bell, 1978, *'The acceleration of cosmic rays at shock fronts'*, MNRAS, **182**, 147

[12] Bernlöhr et al., 2012, *'Monte Carlo design studies for the Cherenkov Telescope Array'*, Astroparticle Physics, **43**, 171

[13] Bernlöhr et al., 2013, *'Progress in Monte Carlo design and optimization of the Cherenkov Telescope Array'*, Proceedings of the 33rd International Cosmic Ray Conference (ICRC2013), Rio de Janeiro (Brazil)

[14] Blumenthal & Gould, 1970, *'Bremsstrahlung, Synchrotron Radiation, and Compton Scattering of High-Energy Electrons Traversing Dilute Gases'*, RevModPhys., **42**, 237

[15] Borriello et al. 2009, *'Radio constraints on dark matter annihilation in the galactic halo and its substructures'*, PhysRev. D, **79**, 023518

[16] Brown 2013, *'Locating the gamma-ray emission region of the flat spectrum radio quasar PKS 1510-089'*, MNRAS, **431**, 824

[17] Burbidge, 1956, *'On Synchrotron Radiation from Messier 87'*, ApJ, **124**, 416

[18] Dermer & Schlickeiser 1993, *'Model for the High-Energy Emission from Blazars'*, ApJ, **416**, 458

[19] Dole et al., 2006, *'The Cosmic Infrared Background Resolved by Spitzer'*, A&A, **451**, 417

[20] Dominguez et al. 2011, *'Axion-like particle imprint in cosmological very-high-energy sources'*, JCAP, **1111**, 020

[21] Fazio et al. 2004, *'Number Counts at 3 $\mu m < \lambda < 10$ μm from the Spitzer Space Telescope'*, ApJS, **154**, 39

[22] Franceschini et al. 2008, *'Extragalactic optical-infrared background radiation, its time evolution and the cosmic photon-photon opacity'*, A&A, **487**, 837

[23] Francis et al. 1991, *'A High Signal-to-Noise Ratio Composite Quasar Spectrum'*, ApJ, **373**, 465

[24] Funk & Hinton, 2013, *'Comparison of Fermi-LAT and CTA in the region between 10-100 GeV'*, Astroparticle Physics, **43**, 348

[25] Gasparrini & Cutini, 2011, *'Fermi-LAT detection of a possible new extragalactic gamma-ray source in the vicinity of TXS 1530-131 (PMN J1532-1319)'*, ATel, **3579**, 1

[26] Ghisellini et al. 2010, *'General physical properties of bright Fermi blazars'*, MNRAS, **402**, 497

[27] Gould & Schreder 1967, *'Pair Production in Photon-Photon Collisions'*, Phys. Rev., **155**, 1404

[28] Hauser et al. 1998, *'The COBE Diffuse Infrared Background Experiment Search for the Cosmic Infrared Background. I - Limits and Detections'*, ApJ, **508**, 25

[29] Hauser & Dwek 2001, *'The Cosmic Infrared Background: Measurements and Implications'*, ARA&A, **39**, 249

[30] Holder, 2012, *'TeV gamma-ray astronomy: A summary'*, Astroparticle Physics, **39**, 61

[31] Jansky, 1933, *'Radio Waves from Outside the Solar System'*, Nature, **132**, 66.

[32] Jelley 1966, *'High-Energy Gamma-Ray Absorption in Space by a 3.5°K Microwave Field'*, Phys. Rev. Lett., **16**, 479

[33] Jennison and Das Gupta, 1953, *'Fine Structure of the Extra-terrestrial Radio Source Cygnus I'*, Nature, **172**, 996

[34] Keel, 1996, *'Seyfert Galaxies With Companions: Orbital and Kinematic Clues to AGN Triggering'*, AJ, **111**, 696

[] Laporte et al., 2012, *'SST-GATE: an innovative telescope for very high energy astronomy'*, Proc. SPIE 8444, Ground-based and Airborne Telescopes IV, 84443A

[35] Lawrence et al., 1996, *'Optical Spectra of a Complete Sample of Radio Sources. I. The Spectra'*, ApJS, **107**, 541

[36] G. Maier, 2011, `http://www.cta-observatory.org/ctawpcwiki/images/1/13/GMaier_DESYAnalysisDescription.pdf`

[37] Maraschi et al., 1992, *'A Jet Model for the Gamma-Ray Emitting Blazar 3C279'*, ApJ, **397**, L5-L9

[38] Marscher et al., 2010, *'Probing the Inner Jet of the Quasar PKS1510-089 with Multi-Waveband Monitoring during Strong Gamma-Ray Activity'*, ApJL, **710**, L126

[39] Mazin & Raue, 2008, *'Optical depth for VHE gamma-rays from distant sources from a generic EBL density'*, IJMP, **17**, 1515

[40] Mortlock et al., 2011, *'A luminous quasar at a redshift of $z = 7.085$'*, Nature, **474**, 616

[41] Nikishov 1962, *'Absorption of High-Energy Photons in the Universe'*, JETP, **14**, 39

[42] Nolan et al., 2012, *'Fermi Large Area Telescope Second Source Catalogue'*, ApJS, **199**, 31

[43] Oort and Walraven, 1956, *'Polarization and composition of the Crab nebula'*, BAN, **12**, 285

[44] Padovani, 1992, *'Is There a Relationship between BL Lacertae Objects and Flat-spectrum Radio Quasars?'*, MNRAS, **257**, 404

[45] Poutanen & Stern, 2010, *'GeV Breaks in Blazars as a Result of Gamma-Ray Absorption within the Broad-Line Region'*, ApJ, **717**, L118

[46] Poutanen & Stern, 2014, *'The Mistery of Spectral Breaks: Lyman Continuum absorption by photon-photon pair production in the Fermi GeV spectra of Bright Blazars*, arXiv:1408.0793

[47] Puget et al. 1996, *'Tentative detection of a cosmic far-infrared background with COBE'*, A&A, **308**, L5

[48] Reimer & Bötcher, 2013, *'Studies of active galactic nuclei with CTA'*, Astroparticle Physics, **43**, 103

[49] Ritz, 2007, *'Overview of the GLAST Mission and Opportunities'*, AIP, **921**, 3

[50] Schmitt, 1968, *'BL Lac identified as a Radio Source'*, Nature, **218**, 663

[51] Schönfelder & Gottfried, 2010, ISSI Scientific Reports Series, ESA/ISSI. ISBN 978-92-9221-938-8, 207

[52] Seyfert, 1943, *'Nuclear Emission in Spiral Nebulae'*, ApJ, **97**, 28

[53] Shklovsky, 1953, *'On the Nature of the Crab Nebula's Optical Emission [in Russian]'*, Doklady Akad. Nauk SSSR, **90**, 983

[54] Sikora et al., 2009, *'Constraining Emission Models of Luminous Blazar Sources'*, ApJ, **704**, 38

[55] Stecker et al. 1992, *'TeV gamma rays from 3C 279 - A possible probe of origin and intergalactic infrared radiation fields'*, ApJ, **390**, L49

[56] Stickel et al., 1991, *'The complete sample of 1 Jansky BL Lacertae objects. I - Summary properties'*, ApJ, **374**, 431

[57] Shaw et al., 2009, *'Optical Spectroscopy of Fermi Bright Blazars'*, ApJ, **704**, 477

[58] Urry & Padovani, 1995, *'Unified Schemes for Radio-Loud Active Galactic Nuclei'*, ASP, **107**, 803

[59] Vashakidze, 1954, *'On the degree of polarization of the light near extragalactic nebulae and the Crab Nebula [in Russian]'*, Astr. Tsirk., **147**, 11

[60] Vermeulen & Cohen, 1994, *'Superluminal motion statistics and cosmology'*, ApJ, **430**, 467

[61] `http://astrophysics.pro/experiments/photoelectric-effect/`. Accessed 04/08/2014.

[62] `http://pondscienceinstitute.on-rev.com/svpwiki/tiki-index.php?page=Compton+Scattering`. Accessed 04/08/2014.

[63] `http://electrons.wikidot.com/pair-production-and-annihilation`. Accessed 04/08/2014.

[64] `http://tevcat.uchicago.edu/about.html`. Accessed 04/08/2014.

[65] http://www.daviddarling.info/encyclopedia/B/blazar.html. Accessed 04/08/2014.

[66] http://en.wikipedia.org/wiki/Image:Photomultipliertube.svg. Accessed 04/08/2014.

[67] http://nsspi.tamu.edu/media/155130/image26.jpg. Accessed 04/08/2014.

[68] http://integral.esac.esa.int. Accessed 04/08/2014.

[69] http://spie.org/x19645.xml. Accessed 04/08/2014.

[70] http://inspirehep.net/record/810115/plots. Accessed 04/08/2014.

[71] http://fermi.gsfc.nasa.gov/ssc/. Accessed 04/08/2014.

[72] http://petrowiki.org/Gamma_ray_logs. Accessed 04/08/2014.